UNIVERSITY OF CALIFORNIA

Los Angeles

Structural Stability and Phase Transformation Behavior In Nanostructured Energy Storage Materials

A dissertation submitted in partial satisfaction of the requirements for the degree Doctor of Philosophy in Chemistry

by

Yiyi Yao

2022

ABSTRACT OF THE DISSERTATION

Structural Stability and Phase Transformation Behavior

In Nanostructured Energy Storage Materials

by

Yiyi Yao

Doctor of Philosophy in Chemistry

University of California, Los Angeles, 2022

Professor Sarah H. Tolbert, Chair

Novel battery technology must be capable of providing both increased energy density and power density to keep up with global energy demand. This dissertation addresses a variety of structural challenges present in energy storage materials for both positive and negative electrode applications. Several materials ($LiMn_2O_4$, MoS_2, and SbSn) have been synthesized as nanoporous architectures to reduce ion diffusion length, mitigate volume changes, and enhance structural stability. The first part of this work describes a facile synthesis for nanoporous $LiMn_2O_4$ and how the self-discharge problem is mitigated by doping with Al^{3+}. Through x-ray photoelectron spectroscopy (XPS), x-ray diffraction (XRD), and electrochemical rate cycling, we show that the Al^{3+} dopant preferentially substitutes Mn^{3+} at the surface, stabilizes the spinel structure at lower temperature (200˚C), mitigates manganese dissolution, while still maintaining good rate cycling

up to current densities of 20C. The second and third chapters of this dissertation focus on de-convoluting the effects of reducing crystal size and lattice disorder in mesoporous MoS_2 pseudocapacitors. A series of mesoporous MoS_2 powders with different sizes and degrees of crystallinity are synthesized through a sulfurization reaction. Crystal size is controlled by the size of mesoporous MoO_2 precursor used, and disorder is controlled by higher annealing temperatures. Ambient synchrotron x-ray total scattering / pair distribution function (PDF) analysis techniques enable us to quantify the extent of layer shifting compared to layer expansion disorder in the matrix of samples. *Operando* x-ray diffraction (XRD) demonstrates that both size and disorder effects cause the suppression Li-intercalation induced phase transitions in MoS_2. The reduced size and increased disorder are correlated to enhanced fast-charging performance up to rates of 100C. Kinetic analyses show size and disorder effects increase the fraction of capacitive current in mesoporous MoS_2, demonstrating that reducing crystal size and increasing lattice disorder are both effective methods for introducing pseudocapacitive charge storage. Using *operando* PDF to study our matrix of size and disordered MoS_2, further understanding into the dynamic evolution of disorder and local structure is achieved. The final chapter elucidates the formation of both crystalline and amorphous phases evolved during the cycling of nanoporous SbSn alloying anode through both *operando* XRD and PDF. The nanoporous architecture of SbSn, intermetallic phase, and ductile amorphous intermediates all provide means of buffering the volume expansion during cycling, resulting in improved long-term cycling stability.

The dissertation of Yiyi Yao is approved.

Justin Ryan Caram

William M. Gelbart

Bruce S. Dunn

Sarah H. Tolbert, Committee Chair

University of California, Los Angeles

2022

Table of Contents

LIST OF FIGURES

Chapter 2: Aluminum Doping Nanoporous $LiMn_2O_4$ Pseudocapacitors Lowers Spinel Crystallization Temperature and Mitigates Self Discharge Through Surface Stabilization.

Chapter 3: Crystal Size and Lattice Disorder as Design Principles for the Suppression of Intercalation-Induced Phase Transitions in Pseudocapacitive Mesoporous MoS_2.

Figure 4.1. SEM images of (a) small disordered (sd), (b) Large Disordered (LD), (c) small crystalline (sc), (d) and bulk MoS_2. (e) HR-TEM image of LD MoS_2 showing disordered lattice planes. (f) XRD patterns of bulk (forest green), sc (pink), LD (blue), sd (red) MoS_2 samples. Reference pattern of 2H-MoS_2 from JCPDS 2-0132 is shown in black sticks.

Figure 4.2. Simulated PDF patterns of 2H-MoS_2, 1T-MoS_2, and triclinic Li_xMoS_2. (a) Nearest neighbor Mo-S bonds that contribute to the correlation at 2.36 Å in 2H-MoS_2. (b) Nearest neighbor Mo-S bonds that contribute to the correlation at 2.36 Å in 1T-MoS_2. (c) Nearest neighbor Mo-S bonds in triclinic Li_xMoS_2. that contribute to the correlation at 2.47 Å. Not all Mo-S bonds in the triclinic phase are symmetric, leading to a broadening of the distribution. (d) Perfect Mo-S octahedron with all Mo-S bonds at same length will give rise to one Mo-S PDF peak. (e) Distorted Mo-S octahedron with longer axial Mo-S bonds will give rise to two Mo-S PDF peaks observed in experimental data, with axial bonds at a higher r-position and a lower intensity because there are half as many axial Mo-S bonds as equatorial Mo-S bonds. (f) Nearest Mo-Mo distance contributing to correlation at 2.94 Å in triclinic Li_xMoS_2. (g) One of multiple sulfur-sulfur correlations across the vdW gap in 1T-MoS_2. (h) Nearest Mo-Mo distance between neighboring trigonal prisms within one layer contribute to correlate at 3.16 Å in 2H-MoS_2.

Figure 4.3. (a) Galvanostatic charge and discharge at C/2 and (b) *operando* XRD of bulk MoS_2. New peak appearing at Q = 1.07$Å^{-1}$ corresponds to the triclinic Li_xMoS_2 phase. (c) Galvanostatic charge and discharge at 1C and (d) *operando* XRD of LD-MoS_2.

Figure 4.4. *Operando* total scattering and pair distribution function for bulk MoS_2. (a) Galvanostatic charge and discharge curve cycled at C/5. Square markers indicate voltages where total scattering patterns were taken. (b) Normalized total scattering. First delithiation scan is

plotted with a yellow line. (c) Normalized corresponding PDF patterns. Reference XRD and PDF patterns for 2H MoS_2 (purple), 1T MoS_2 (green), and triclinic $LiMoS_2$ (gold) are shown.

Figure 4.5. *Operando* total scattering and pair distribution function for small crystalline MoS_2. (a) Galvanostatic charge and discharge curve cycled at C/5. Pink circle markers indicate voltages where total scattering patterns were taken. (b) Normalized total scattering. First delithiation scan is plotted with a pink line. (c) Normalized corresponding PDF patterns. Simulated PDF patterns for 2H MoS_2 (purple), 1T MoS_2 (green), and triclinic $LiMoS_2$ (gold) are plotted for reference.

Figure 4.6. *Operando* total scattering and pair distribution function for large disordered MoS_2. (a) Galvanostatic charge and discharge curve cycled at C/5. Blue circle markers indicate voltages where total scattering patterns were taken. (b) Normalized total scattering. First delithiation scan is plotted with a blue line. (c) Normalized corresponding PDF patterns. Simulated PDF patterns for 2H MoS_2 (purple), 1T MoS_2 (green), and triclinic $LiMoS_2$ (gold) are plotted for reference.

Figure 4.7. *Operando* total scattering and pair distribution function for small disordered MoS_2. (a) Galvanostatic charge and discharge curve cycled at C/5. Blue circle markers indicate voltages where total scattering patterns were taken. (b) Normalized total scattering. First delithiation scan is plotted with a blue line. (c) Normalized corresponding PDF patterns. Simulated PDF patterns for 2H MoS_2 (purple), 1T MoS_2 (green), and triclinic $LiMoS_2$ (gold) are plotted for reference.

Figure 4.8. Multi-phase refinement in the 0 – 10 Å range of PDF pattern for (a) small disordered, (b) Large Disordered, (c) small crystalline, and (d) bulk MoS_2, showing the percentage of 2H-MoS_2, 1T-MoS_2, and triclinic Li_xMoS_2 present during each PDF pattern throughout the *operando* experiment. Black dotted line indicates the end of lithiation. Percentage is calculated from the fraction of each phase of total refined scale factors.

LIST OF TABLES

ACKNOWLEDGEMENTS

There are so many people that have supported me, without whom I could not be standing here today. Thank you to my mom and dad who worked hard and sacrificed a lot so that we could have a new life in America. Thank you to my little brother, William, who has been one of my best friends since childhood and has borne my whims and abuses. Thank you to my aunt and uncle (gugu and gufu), and my cousin Qiqi.

Thank you to my advisor, Sarah Tolbert, for challenging me to think and question, and not to take the fundamental general chemistry questions for granted. Thank you to my committee members (Prof. Justin Caram, Prof. Bruce Dunn, Prof. Bill Gelbart) for their advice and help. Thank you to many older students and post-docs were who were teachers and mentors to me: Terri Lin, Yan, Yan, Stephen Sasaki, Sabrina Fischer. Thanks especially to Matt Lai who bought me an awesome mortar and pestle. Thank you to my labmates for being ridiculous nerdy people who make me simultaneously laugh and weep on a regular basis. Thanks especially to collaborators and mentees: Joe Mazzetti, Danny Robertson, Helen Cumberbatch, David Pe, Kodi Thurber. Thank you to awesome collaborators/friends from other research groups: Danielle Butts, Grace Whang, Tian Deng, Erin Avery, Naihao Chang, Omar Leon. Thank you to Dr. Hung Pham, who made every quarter teaching ochem fun, even though organic chemistry is not my forte. Thank you to all the staff of the chemistry department and graduate office advisors. Thank you to the guys in Shipping and Receiving.

Thank you to the beamline scientists at SSRL who helped us during our operando diffraction experiments: JR Troxel, Chris Tassone, David Agyeman-Budu, Johanna Nelson Weker. Thank you to the beamline scientists at APS for advice for submitting proposals and during

operando studies, especially during limited COVID-19 operations: Andrey Yakovenko, Kamila Wiaderek, Olaf Borkiewicz, Leighanne Gallington.

Thank you to my friends from Berkeley (Yinyin, Samantha, Amanda, Wanjiku, Kimberley, Charlene) who came and visited me, gave me money, and listened to my endless complaints. Thanks especially to Samantha, who designed the painting (at my request) to brighten my office, and Kim, who helped paint it! I'm thankful I have a daily visual reminder of how loved I am. Thank you to Lauren Kim, who always praises and encourages me. Thank you to many friends in Los Angeles (Sarah Low, Annie Wang, Jen and Caleb Price, Devin and Kate Deuell, Sean and Melissa Lyons, Marissa Han, Christian Ubillus, Joey and Bryan Elliff) for their love and kindness that encourages and inspires me. Thank you to my friends and church community from The Commons LA and Salt and Light for their prayers and support. Most of all, every breath is possible thanks to Jesus Christ, my Creator, Lord, Savior, and the God of second chances.

PREVIOUS PUBLICATIONS AND CONTRIBUTIONS OF CO-AUTHORS

Chapter 2 is a version of Yiyi Yao, Danielle Butts, Yan Yan, Chenlu Yang, Bruce Dunn, and Sarah H. Tolbert, "Aluminum Doping Nanoporous $LiMn_2O_4$ Pseudocapacitors Lowers Spinel Crystallization Temperature and Mitigates Self Discharge Through Surface Stabilization." I synthesized and characterized the raw material, performed electrochemical testing, and wrote manuscript. Danielle fabricated electrodes and performed electrochemical testing. Yan performed XPS on nanoporous LAMO. Chenlu helped in some synthesis and characterization of nanoporous LAMO. Prof Dunn and Prof Tolbert oversaw the research and edited the manuscript. This manuscript will be submitted for publication shortly after this dissertation is filed.

Chapter 3 is a version of Yiyi Yao, Daniel Robertson, Matthew A Chin, Ryan Lamkin, and Sarah H. Tolbert, "Crystal Size and Lattice Disorder as Design Principles for the Suppression of Intercalation-Induced Phase Transitions in Pseudocapacitive Mesoporous MoS_2." I synthesized and characterized the raw material, fabricated electrodes, performed electrochemical testing, performed *operando* XRD, analyzed and simulated PDF data, and wrote manuscript. Daniel synthesized the mesoporous MoO_2 precursor, took TEM images, performed *operando* XRD, and edited the manuscript. Matthew contributed to synthesis and characterization of material. Ryan helped process 2D synchrotron data from *operando* XRD experiment. Prof Tolbert oversaw the research and edited the manuscript. This manuscript will be submitted for publication shortly after this dissertation is filed.

Chapter 4 is a version of Yiyi Yao, Daniel Robertson, Kamila Wiaderek, Olaf Borkiewicz, Andrey Yakovenko, and Sarah H. Tolbert, "Studying Dynamic Disorder Evolution with *Operando* Pair Distribution Function Analysis in Mesoporous MoS_2." I synthesized and characterized the

raw material, fabricated electrodes, performed electrochemical testing, performed *operando* XRD and PDF, analyzed and simulated PDF data, and wrote manuscript. Daniel synthesized the mesoporous MoO_2 precursor, took TEM images, performed *operando* XRD, and edited the manuscript. Kamila, Olaf, and Andrey set up alignment, calibration, and scan parameters at APS BL 11-ID-C. Kamila processed the Fourier transformed PDF data. Prof Tolbert oversaw the research and edited the manuscript. This manuscript will be submitted for publication shortly after this dissertation is filed.

Chapter 5 is a version of Yiyi Yao, Joseph Mazzetti, Kodi Thurber, David Agyeman-Budu, Johanna Nelson Weker, and Sarah H. Tolbert, "Improving Structural and Long-Term Stability in SbSn Alloy Anodes via Control of Nanoarchitectures and Intermediates." Joe and Kodi synthesized and characterized the raw material, fabricated electrodes, and performed electrochemical testing. I performed the *operando* XRD and *operando* PDF measurements, processed and analyzed the data. Joe and I wrote the manuscript. David and Johanna helped with some *operando* XRD experiments at SSRL. Prof Tolbert oversaw the research and edited the manuscript. This manuscript will be submitted for publication shortly after this dissertation is filed.

VITA

2011	College of Chemistry Undergraduate Summer Research Fellowship, UC Berkeley
2012	B.S. in Chemistry from University of California, Berkeley
2014	M.S. in Chemistry from University of Minnesota, Twin Cities
2016 - present	Electrochemical Society (ECS) Student Chapter member, UCLA
2018	California NanoSystems Institute (CNSI) Nanoscience Outreach, Nanovation mentor
2019	Mad Scientist Escape Room creator at Explore Your Universe, UCLA
2020	UCLA Chemistry and Biochemistry Excellence in Research Fellowship

LIST OF PUBLICATIONS AND PRESENTATIONS

1. Kim, S.S., Agyeman-Budu, D.N., Zak, J.J., Dawson, A., Yang, Q., Caban-Acevedo, M., Wiaderek, K.M., Yakovenko, A.A., **Yao, Y.**, Irshad, A., Narayan, S.R., Luo, J., Nelson-Weker, J., Tolbert, S.H., See, K.A. "Promoting Reversibility of Multielectron Redox in Alkali-Rich Sulfide Cathodes through Cryomilling", *Chemistry of Materials*, **2022**, 34, 7, 3236 – 3245.
2. Anderson, N.H., Odoh, S.O., **Yao, Y.**, Williams, U.J., Schaefer, B.A., Kiernicki, J.J., Lewis, A.J., et al. "Harnessing redox activity for the formation of uranium tris(imido) compounds", *Nature Chemistry*, **2014**, 6, 919-926.
3. **Yao, Y.**, Jariwala, K., Martin, R., Haranczyk, M. "Computational Design of Materials for Gas Storage". Cal Energy Corps Research Symposium. Poster presentation. 2012.

CHAPTER 1: Introduction

As our society's energy demands grow larger and more diverse, much effort has been put into transitioning from fossil fuel resources to renewable energy sources such as solar, wind, hydrogen, and geothermal. Prof. Richard Smalley, who was awarded the Nobel Prize in Chemistry in 1996 for the discovery of buckminsterfullerene, once presented the energy problem as the foremost of "Humanity's Top Ten Problems for the next 50 years".[1] At the time of his lecture "Our Energy Challenge" in 2004, he sagely asserted, "the biggest single problem of electricity is storing it." Not only is it imperative to store energy, but our energy storage technology must be able to discharge power efficiently at peak usage hours to provide a robust energy management system.[2-3] Therefore, there is an urgent need for energy storage materials that can provide both higher power density and energy density than the currently dominant lithium-ion technology.

Since its commercialization by Sony Corporation in 1991, the lithium-ion battery (LIB) has transformed the way we live and work, making portable electronics widely available.[4] As we look towards utilizing battery technology for future applications such as electric vehicles and smart electrical grid storage, it is evident that dramatic improvements in both energy density and power density are needed. Energy density is the total amount of charge the material can store, reported gravimetrically or volumetrically. The energy density of the material has direct implications on the weight, size, and therefore energy efficiency of an electric vehicle. For example, the battery pack of a Tesla Model S constitutes 26% of the total car weight.[5] Power density is the rate at which energy can be charged or discharged from a material. Typical LIBs reach full charge within hours but re-fueling a gasoline-powered vehicle takes only minutes; therefore, the power density limitations of the LIB present significant barriers to widespread adoption of electric vehicles.

The canonical LIB is composed of an anode, cathode, and separator with electrolyte. The electrolyte is ionically conducting, while being electronically insulating. The potential difference between anode and cathode drives a spontaneous redox reaction, where the anode transfers electrons to the cathode through an external circuit, generating electricity. For charge balance, the electron transfer is accompanied by the movement of Li^+ from anode, through the electrolyte, to the cathode (during discharge). The anode is typically made of graphite, while the cathode is often a transition metal oxide such as $LiCoO_2$.[6] Because solid state diffusion of Li^+ is slow, this process often limits the current and power density of batteries.

Pseudocapacitors are a class of materials that have the unique opportunity to bridge the gap between high energy density and high power density.[7-10] Pseudocapacitors store charge through redox reactions like traditional battery materials, but show an electrochemical signature similar to electric double layer capacitors (EDLC), which store charge through surface ion adsorption.[11-12] This phenomenon is observed because redox in a pseudocapacitor occurs at the surface or near surface regime, and therefore Li^+ ion transport is no longer limited by solid state diffusion.[13-19]

There has been significant discussion around the precise definition of a pseudocapacitor, with some taking a narrower view that a 'pseudocapacitor' is not phenomenologically different from a true capacitor, while others claim that a range of physical mechanisms can give rise to the same electrochemical features typically characterized as "pseudocapacitive."[12,20] The fundamental question lies in whether the physical mechanism of charge storage or the observed electrochemical behavior ought to be the characteristic feature of a pseudocapacitor. Without taking a strong stance on this question, we clarify that our research aims to shed greater light onto the physical mechanisms that give rise to "pseudocapacitive" electrochemical behavior.

Initial work in the 1960s by Conway and others used the term "pseudocapacitance" to refer to surface Faradaic processes such as underpotential deposition and hydrogen adsorption.[21] Electron transfer occurs across an interface (making it Faradaic) but the kinetic behavior is not governed by solid-state diffusion. Over time, our notion of pseudocapacitance has expanded beyond surface reactions to intercalation pseudocapacitance, where ions intercalate into the entire material reversibly but still demonstrate electrochemical features like an EDLC and support fast rate capability (or fast charging times). A recent review on pseudocapacitance from the Augustyn group broadly defines pseudocapacitance as electrochemical behavior that "is not limited by solid-state diffusion at time scales of minutes and whose electrochemical response is highly reversible, leading to high efficiency at high current densities."

Therefore, we aim to elucidate structural features that give rise to pseudocapacitive electrochemical behavior. Previous work from our research group has shown that nanostructuring a bulk battery material can shorten the Li^+ ion diffusion length. At some critical nano-size, there is suppression of first-order phase transition upon lithium intercalation, resulting in superior rate capability.[22] Therefore, one of our key criteria for introducing pseudocapacitive properties into a battery material has been the suppression of intercalation-induced phase transitions and minimizing structural change between lithiated and de-lithiated phases. Reducing the particle size has proven to be an effective strategy for accomplishing this; however, in highly disordered systems, it is unclear to what extent the suppression of phase transition is influenced by size effects compared to increased lattice disorder. A significant portion of this dissertation will discuss how we de-convolute the two effects in nanostructured MoS_2.

Another important class of LIB materials are alloying anodes, which are typically metalloid or metallic elements such as Si, Ge, Sn, and Sb that store charge by forming an alloy with Li^+,

allowing for much larger energy densities than intercalation materials.[23-25] These materials can provide much higher energy density (994 $mAh \cdot g^{-1}$ for Sn, 660 $mAh \cdot g^{-1}$ for Sb) compared to graphite (372 $mAh \cdot g^{-1}$) and their metallic character affords good conductivity. However, the higher energy density comes with a cost of significant volume expansion and contraction during cycling. For example, graphite undergoes just a 10% volume expansion upon Li^+ intercalation, while the volume of a $Si_{66}Sn_{34}$ alloy increases by 264% during Li^+ alloying. Repeated cycling with such large volume expansion eventually leads to long-term cracking and capacity fade. Strategies for alleviating this issue include synthesizing the material as a nanoporous network to allow expansion into the pores while maintaining a connected, conductive network. Previous work in our group has demonstrated the synthesis of a nanoporous SbSn intermetallic that buffers volume expansion through the porous architecture, as well as by utilizing two metals that alloy with Li^+ at different potentials (Sb at 0.8 V, Sn at 0.7, 0.6, and 0.5 V).[26] This multi-stage lithiation process allows one component to act as an inert, flexible matrix during the lithiation of the other. The volume expansion problem is significantly mitigated, as demonstrated by retention of 595 mAh/g after 100 cycles at C/5 rate. However, the complexities of intermediate phases formed during (de)-lithiation of the intermetallic are poorly characterized. Therefore, in the last chapter of this dissertation, we elucidate the nature of both the crystalline and amorphous intermediates formed during cycling of nanoporous SbSn and correlate their structure with improved long-term cycling performance.

1.1 References.

[1] Richard E. Smalley. "Our Energy Challenge." Lecture. https://scholarship.rice.edu/bitstream/handle/1911/91314/NANO_Smalleylecture.pdf

[2] https://energystorageforum.com/energy-storage-technologies/smart-grid-energy-storage-systems

[3] Dedes, I.-C.; Tsampasis, E.; Elias, C.; Gkonis, P. "Energy Storage in Smart Electrical Grids." 10th Mediterranean Conference on Embedded Computing (MECO), 2021, p. 1 – 4. doi: 10.1109/MECO52532.2021.9460169.

[4] Blomgren, G. E. The Development and Future of Lithium Ion Batteries. *Journal of The Electrochemical Society*. **2017**, 164, A5019.

[5] https://www.tesla.com/models.

[6] Mizushima, K., et al. Li_xCoO_2 ($0 < x \leq 1$): A new cathode material for batteries of high energy density. *Solid State Ionics*, **1981**, 3 / 4, 171 – 174.

[7] Fleischmann, S., et al. Pseudocapacitance: From Fundamental Understanding to High Power Energy Storage Materials. *Chem. Rev*. **2020**, 120, 6738 - 6782.

[8] Conway, B.E., et al. Double-layer and pseudocapacitance types of electrochemical capacitors and their applications to the development of hybrid devices. *J. Solid State Electrochem*. **2003**, 7, 637 – 644.

[9] Augustyn, V., et al. Pseudocapacitive oxide material for high-rate electrochemical energy storage. *Energy & Environmental Science.* **2014**, 7, 1597 – 1614.

[10] Zhang, X.-L.; Zhang, W.-B.; Han, X.-W.; Zhang, L.; Bao, X.; Guo, Y.-W.; Chai, S.-S.; Guo, S.-B.; Zhou, X.; Ma, X.-J. "Review – Pseudocapacitive Energy Storage Materials from Hägg-Phase Compounds to High-Entropy Ceramics." *Journal of The Electrochemical Society*, **2021**, 168, 120521.

[11] Simon, P., et al. Where Do Batteries End and Supercapacitors Begin? *Science.* **2014**, 343, 1210 – 1211.

[12] Brousse, T., et al. To Be or Not To Be Pseudocapacitive? *Journal of The Electrochemical Society.* **2015**, 162 (5), 5185 – 5189.

[13] Kim, H.-S., et al. The Development of Pseudocapacitive Properties in Nanosized-MoO_2. *Journal of The Electrochemical Society.* **2015**, 162 (5), 5083 – 5090.

[14] Cook, J.B., et al. Mesoporous MoS_2 as a Transition Metal Dichalcogenide Exhibiting Pseudocapacitive Li and Na-Ion Charge Storage. *Advanced Energy Materials.* **2016**, 6, 1 – 12.

[15] Cook, J.B., et al. Pseudocapacitive Charge Storage in Thick Composite MoS_2 Nanocrystal-Based Electrodes. *Advanced Energy Materials.* **2017**, 7, 1 – 12.

[16] Lesel, B.J., et al. Using Nanoscale Domain Size to Control Charge Storage Kinetics in Pseudocapacitive Nanoporous $LiMn_2O_4$ Powders. *ACS Energy Letters.* **2017**, 2, 2293 – 2298.

[17] Lesel, B.J., et al. Mesoporous $Li_xMn_2O_4$ Thin Film Cathodes for Lithium-Ion Pseudocapacitors. *ACS Nano.* **2016**, 8, 7572 – 7581.

[18] Muller, G. A., et al. High Performance Pseudocapacitor Based on 2D Layered Metal Chalcogenide Nanocrystals. *Nano Letters.* **2015**, 15, 1911 – 1917.

[19] Augustyn, V., et al. High-rate electrochemical energy storage through Li^+ intercalation pseudocapacitance. *Nature Materials.* **2013**, 12, 518 – 522.

[20] Costentin, C., et al. Energy storage: pseudocapacitance in prospect. *Chem. Sci.* **2019**, 10, 5656 – 5666.

[21] Conway. B.E., et al. Kinetic Theory of Pseudo-Capacitance and Electrode Reactions at Appreciable Surface Coverage. *Trans. Faraday Soc.* **1962**, 28, 2493 – 2509.

[22] Cook, J.B., et al. Suppression of Electrochemically Driven Phase Transitions in Nanostructure MoS_2 Pseudocapacitors Probed Using Operando X-ray Diffraction. *ACS Nano.* **2019**, 13, 1223 – 1231.

[23] Obrovac, M.N., et al. Alloy Negative Electrodes for Li-Ion Batteries. *Chem. Rev.* **2014**, 114, 11444 – 11502.

[24] Park, C.-M., et al. Li-alloy based anode materials for Li secondary batteries. *Chem. Soc. Rev.* **2010**, 39, 3115 – 3141.

[25] Moyassari, E., et al. The Role of Silicon in Silicon-Graphite Composite Electrodes Regarding Specific Capacity, Cycle Stability, and Expansion. *Journal of The Electrochemical Society*. **2022**, 169, 010504.

[26] Lin, T.C., et al. Understanding Stabilization in Nanoporous Intermetallic Alloy Anodes for Li-Ion Batteries Using *Operando* Transmission X-ray Microscopy. *ACS Nano*. **2020**, 14, 14820 – 14830.

CHAPTER 2: Aluminum Doping Nanoporous $LiMn_2O_4$ Pseudocapacitors Lowers Spinel Crystallization Temperature and Mitigates Self Discharge Through Surface Stabilization

2.1 Introduction.

Increasing consumer demand, coupled with numerous government initiatives for cheaper and more scalable energy storage to utilize renewable resources, highlight the need for continued advancements in Li-ion battery (LIB) technology.[1-3] Constraints on the cell voltage, energy density, and long-term cycling often originate from limitations in the cathode chemistry.[4,5] Therefore, significant efforts have been focused on developing cathode materials with improved structural stability.

Lithium manganese oxide (LMO), $LiMn_2O_4$, is an extensively studied cathode material that represents a more cost-effective, environmentally friendly, and thermally stable alternative to the commonly used $LiCoO_2$ (LCO).[6-20] LMO adopts a spinel crystal structure with tetrahedral sites housing Li^+ that can travel through three-dimensional diffusion pathways.[21,22] While it provides lower energy density, with a theoretical capacity of 148 $mAh \cdot g^{-1}$, LMO has been utilized for high power density applications such as power tools, which require a large burst of energy in a short amount of time.[11] Currently, bulk LMO is sold commercially as a high-rate battery material for (dis)charging up to 2C, full charge within 30 minutes, while still retaining 50% of theoretical capacity.[23-24]

To encourage widespread adoption of electric vehicles, significant improvements in the battery charging time are needed. Therefore, we aim to push the practical application of LMO to even higher power densities of 20C, which corresponds to full charge within 3 minutes, by

introducing a scalable method for synthesizing nanocrystalline LMO. Nanostructuring of materials is an effective way to shorten the Li^+ ion diffusion length, increase surface area, and introduce aspects of pseudocapacitive behavior.[25,26] Pseudocapacitors are materials that store charge through surface or near surface redox reactions, so that the current is not limited by solid-state ion diffusion; this allows them to exhibit a capacitor-like electrochemical response, despite the fact that they are fundamentally faradaic systems.[27-32] Several studies have shown that first-order Li^+ intercalation-induced phase transitions in bulk battery materials can be suppressed the nanostructured form, and this suppression is a key feature for pseudocapacitive charge storage.[33-35] Among potential pseudocapacitive cathode materials, LMO has another advantage in its relatively lower crystallization temperature of 400 – 500˚C, which enables LMO to be easily synthesized in a nanoscale architecture without the grain growth that generally occurs upon crystallization of more conventional cathode materials.[36-38]

However, a known challenge with LMO is the surface disproportionation reaction, which occurs when two Mn^{3+} ions react to form Mn^{4+} and Mn^{2+}.[39-41] Unfortunately, the Mn^{2+} is highly soluble in Li-ion electrolytes.[40] This leads to degradation of the active material and self-discharge, where the voltage decays spontaneously in the charged state without any connection to an external circuit.[11,42] Self-discharge also reduces the long-term stability and cycle life of the battery.[43] The dissolved Mn^{2+} can likewise migrate to and deposit on the anode, causing an increase in cell resistance.[44,45] The surface disproportionation problem is exacerbated in a nanostructure due to increased surface area.

Many researchers have endeavored to solve the surface issue through methods such as protective layer coatings by ALD or CVD, synthesizing structures with preferential (111) stable faceting, and cation doping through melt impregnation.[21,46-52] Several of these approaches rely on

expensive instrumentation and precursors, or a lengthy fabrication process. Here we present a simple solution phase sol-gel method to substitute a small fraction of Mn^{3+} in nanoporous LMO with Al^{3+} dopant while creating an optimized nanoscale architecture using a colloidal polymer template. Al^{3+} is chosen because its incorporation into the spinel structure is facile and increases the average Mn oxidation state, making unfavorable the formation and dissolution of Mn^{2+}.[49,53] We have synthesized a highly nanoporous $LiAl_{0.1}Mn_{1.9}O_4$ (LAMO) network that shows significantly reduced self-discharge, while maintaining good conductivity and rate capability. The Al^{3+} dopant is also shown to stabilize the formation of the spinel structure at lower temperatures.

2.2 Experimental

2.2.1. Synthesis of colloidal polymethyl(methacrylate) (PMMA) template. The method is adapted from Wang et al.[54] A three-neck flask fitted with a condenser and septa was loaded with 165 mL of milliQ water, 0.3 mL of ammonium lauryl sulfate (ALS) solution, and 12.55 mL of methyl methacrylate (MMA). The solution was bubbled under N_2 for 20 – 30 mins while stirring to remove O_2 and prevent premature polymerization. A separate solution of 0.075 g of ammonium persulfate (APS) dissolved in 10 mL of H_2O was prepared. The MMA solution was ramped up to 73˚C in ~ 3 minutes. During the ramp, when the temperature reached 65˚C, the APS solution was injected into the three-neck flask. The reaction was stirred and heated at 73˚C for 3 hours. The product was purified by liquid-liquid extraction in a separatory funnel with hexanes to remove any remaining precursors. The colloid size was confirmed by dynamic light scattering (DLS) and scanning electron microscopy (SEM) to be 40 – 80 nm in diameter. The mass fraction of the colloid solution was measured using thermogravimetric analysis (TGA).

2.2.2. Synthesis of sol-gel templated nanoporous LMO and LAMO**.** In the synthesis of nanoporous LMO, 0.1517 g of $LiNO_3$ (2.2 mmol) and 1.004 g of $Mn(NO_3)_2{\cdot}4H_2O$ were added to 6.78 mL of aqueous solution of colloidal PMMA (solution density 55.3 mg/mL). For the LAMO precursor solution, 0.9 g of $Mn(NO_3)_2{\cdot}4H_2O$ and 0.15 g of $Al(NO_3)_3{\cdot}9H_2O$ were used to achieve a 5% substitution of Mn^{3+} with Al^{3+}. Other Mn:Al ratios were explored, but this ratio was determined to produce the best battery performance, so it was used for all studies presented here. Once the precursors were dissolved, the solution was heated at 60˚C for 40 mins to drive sol-gel reactions and to remove part of the water. The resulting viscous liquid was poured into a petri dish and dried overnight at room temperature in a chamber with flowing air at a controlled humidity between 20-28%. After 11 hours of drying, a translucent gel formed in the petri dish. The gel was scraped out and placed in a quartz boat for calcination. Dried gel was heated in a muffle furnace under ambient air up to 500˚C over 4 hours at a rate of 2˚/min and soaked at 500˚C for 2 hours before being allowed to freely cool to room temperature (**Figure 2.1**).

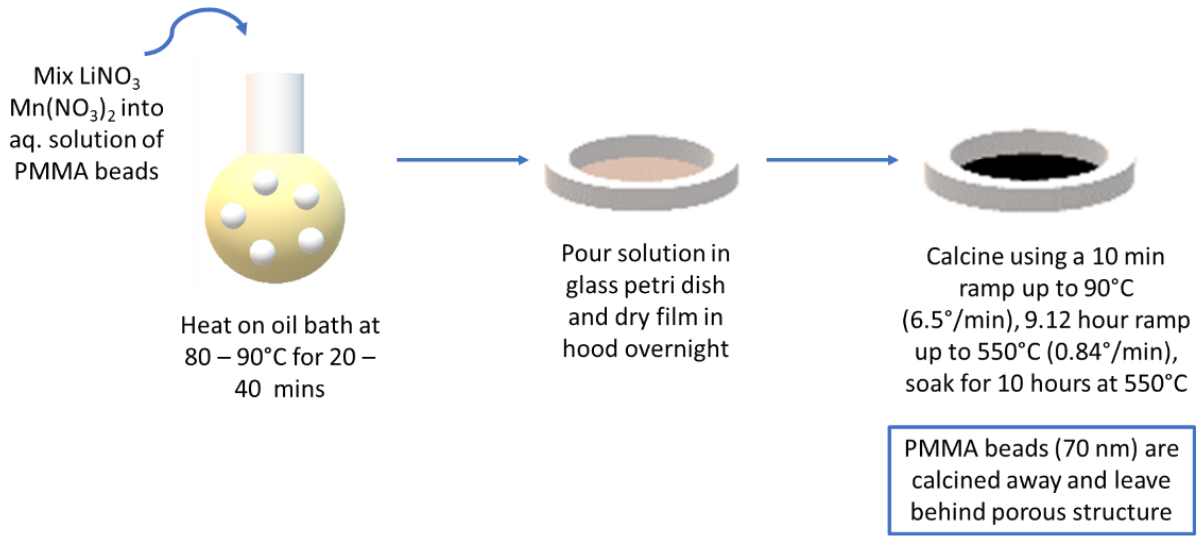

Figure 2.1. Schematic of $LiMn_2O_4$ (LMO) sol-gel reaction and subsequent calcination.

2.2.3. Material characterization**.** Scanning electron microscopy (SEM) images were obtained using a JEOL model 6700F electron microscope. X-ray diffraction (XRD) patterns were collected with a PANalytical X'Pert Pro diffractometer operating with Cu Kα (λ = 1.5418 Å) using a 0.05° step size, an accelerating voltage of 45 kV, and a current of 40 mA. Variable temperature XRD experiments were conducted using an HTK-1200N-2 Anton Paar heating stage on the PANalytical X'Pert Pro diffractometer described above. All heating was done in air, and once the sample reached target temperature, it was held there for 30 mins to equilibrate before taking diffraction patterns. XRD patterns were collected from 15 – 80˚ 2θ. JCPDS pattern 35-0782 was used as reference for $LiMn_2O_4$, pattern 1-1127 for Mn_3O_4, and pattern 1-1206 for MnO as possible impurity phases.

Surface area was measured by nitrogen adsorption porosimetry and calculated from the adsorption branch of the isotherm at low relative pressures using the Brunauer-Emmett-Teller (BET) model. Nitrogen porosimetry was carried out using a Micromeritics TriStar II 3020 porosimeter. Thermal gravimetric analysis (TGA) was performed on a Perkin Elmer Diamond TGA/DTA. TGA on dried pre-calcination gels was performed by holding the sample at room temperature for 1 min, ramping up to 400˚C at 2.0˚C/min, and holding at 400˚C for 30 mins - 1 hour. XPS was performed using a Kratos Axis Ultra DLD with a monochromatic Al Kα radiation source. The charge neutralizer filament was used to control charging of the sample, a 20 eV pass energy was used with a 0.05 eV step size, and scans were calibrated using the C 1s peak shifted to 284.8 eV. The samples were etched with an Ar beam (raster size 5 mm x 5 mm) for 1 min. The integrated area of the peaks was found using the CasaXPS software, and atomic ratios were also

found using this software. The atomic sensitivity factors used were from the Kratos library within the Casa software.

2.2.4. Electrochemical characterization. For electrochemical cycling, LMO was fabricated into slurry electrodes with composition of 80% active material, 5% carbon nanofibers, 5% carbon nanotubes, and 10% poly(3-hexylthiophene-2,5-diyl) (P3HT). P3HT has shown excellent behavior as a protective coating and conductive binder for high-rate cathode materials.[55] To make the slurries, the powders were first ground together with xylenes in a mortar and pestle to form a wet slurry without binder. The binder-less slurry was dried directly in the pestle to obtain a film of homogeneously dispersed active material and carbon. This film was scraped and ground with a solution of P3HT dissolved in xylenes (20 mg/mL). Slurries were cast on Al foil with a doctor blade at 25 μm and dried overnight at 140˚C under vacuum. Electrode discs with an area of 0.71 cm^2 were punched out and assembled into 2032 coin cells. Cells were assembled with 2 stainless steel spacers, a stainless steel spring, Li metal as counter and reference electrode, 1M $LiPF_6$ in EC/DMC/DEC as electrolyte, and celgard as the separator.

Galvanostatic cycling (GV) was performed from 3.5 – 4.5 V (vs. Li^+/Li) at current densities of 1C, 5C, 10C, and 20C, where the C-rate is calculated from theoretical capacity of 148 $mAhg^{-1}$. Potentiostatic electrochemical impedance spectroscopy (PEIS) was performed on cells in the discharged stated at 3.5 V by first applying a 5 min potentiostatic hold to let residual current decay, then applying a 10 mV input between 1MHz – 100 mHz frequencies. EIS Nyquist plots were fit to the equivalent circuit $R_1 + \frac{Q_2}{R_2} + Q_3$ in the ZFit module of EC-Lab software from Biologic. Details of the EIS fitting can be found in SI. Self-discharging tests were performed by first

charging the cell up to 4.5 V with a 1C current, and then turning off the current and measuring voltage drop over time.

2.3 Results and Discussion.

2.3.1 Material characterization. XRD patterns of LMO and $LiAl_{0.1}Mn_{1.9}O_4$ (LAMO) (**Fig 2.2a**) confirm a well-crystallized spinel product and demonstrate the Al^{3+} has been incorporated into the structure without phase separation. From the full-width-at-half-maximum of the peak at 18˚ and Scherrer equation, an approximate crystallite domain size was calculated to be 35 nm. SEM images of LMO (Fig 1c) and LAMO (Fig 1d) show a uniform porous structure with pores on the order of 50 – 100 nm, consistent with the size of colloidal PMMA template. Porosity is further confirmed by the rapid increase in adsorbed nitrogen in the adsorption and desorption branches of the BET isotherm at higher pressures (Fig 1b), corresponding to capillary condensation in the pores. Pure LMO has a surface area of 9.9 m^2g^{-1} while the LAMO has a surface area of 18.8 m^2g^{-1}. The LAMO also shows more nitrogen adsorption in the capillary condensation regime. Both of these facts suggest somewhat higher porosity and smaller pores in the LAMO material. It is possible that this arises because Al^{3+} hydrolyzes more quickly in aqueous solution under acidic conditions than Mn^{3+},[56] and therefore the LAMO reaction is able to trap more PMMA template in the amorphous gel precursor, resulting in a more porous product. It may also be related to the difference in crystallization kinetics, which are discussed in more detail below. It is important to note that based on surface area alone, the LAMO should show more self-discharge and lower capacity than the LMO, so that any deviations from that expected result can be ascribed to positive effects from Al^{3+} inclusion.

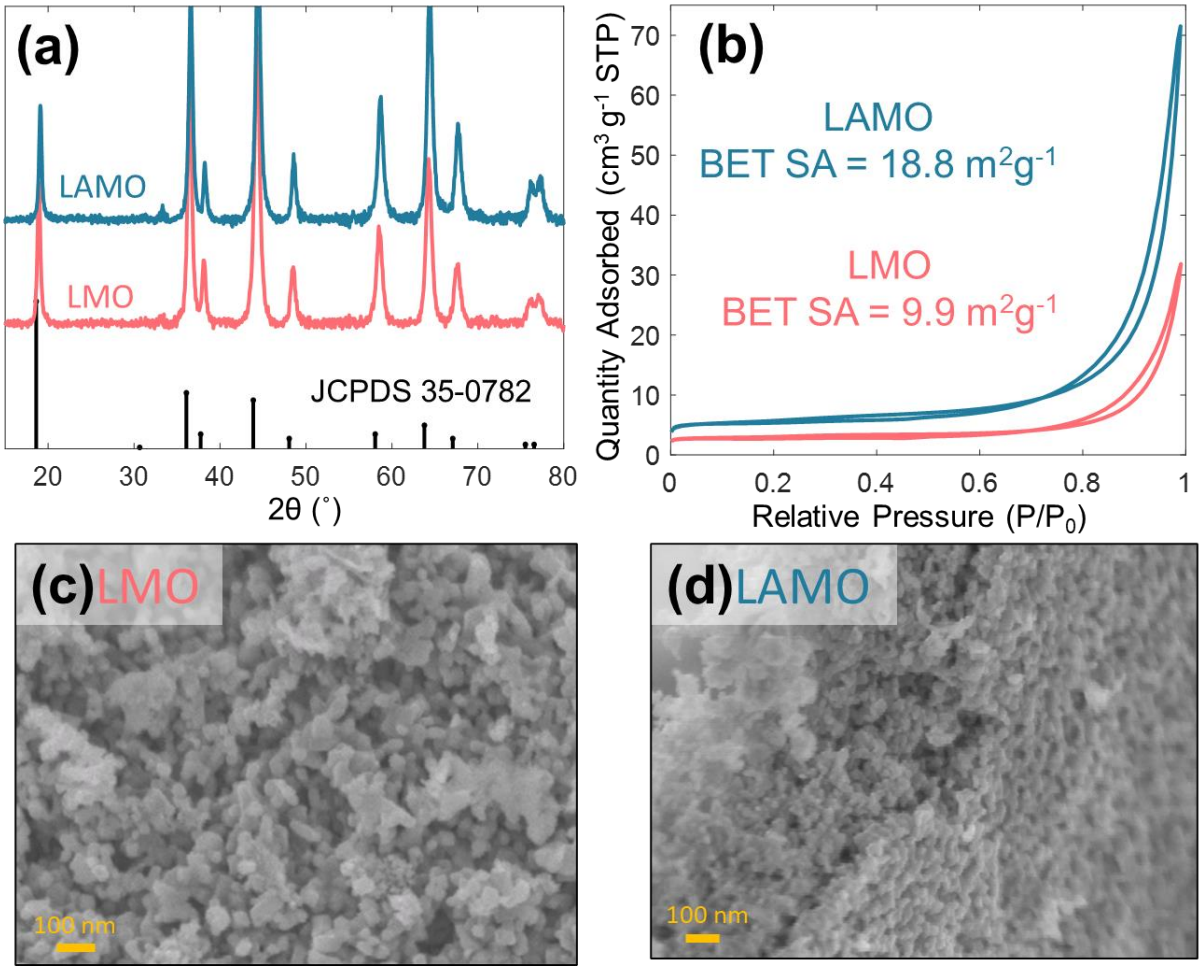

Figure 2.2. a) XRD patterns of pure LMO (pink) and LAMO (turquoise) showing a well-crystallized spinel product. b) BET isotherms and surface area for LMO and LAMO. c,d) SEM images of nanoporous LMO (c) and nanoporous LAMO (d). Both samples are highly porous, phase pure spinel material, but the pores size appears to be smaller and the pore volume and surface area higher in the LAMO.

XPS spectra of LAMO powder (**Figure 2.3a,b**) confirm the presence of both Mn and Al. Mn 2p peak has been fit to contributions from Mn^{2+}, Mn^{3+}, and Mn^{4+}. Assuming the target stoichiometry of $LiAl_{0.1}Mn_{1.9}O_4$ has been achieved, the average ratio of Mn:Al should be 19:1.

Since XPS only probes the surface of a material, Ar ion plasma etching was also performed to quantify the Mn:Al ratio beneath the surface. XPS quantification (Fig 2.3c) shows that the surface Mn:Al ratio is 8.3, while the etched Mn:Al ratio is 12.5. Therefore, the surface of LAMO has a higher ratio of Al^{3+} than the interior, confirming that the Al^{3+} dopant is concentrated on the surface and has a surface stabilization effect. Since the etched Mn:Al ratio is still lower than the target bulk ratio of 19:1, this may suggest there is a gradient of Al^{3+} through the material, with Al^{3+} preferring the surface and the particle center having a Mn-rich stoichiometry. This spontaneous preference of dopant ions for the spinel surface has been observed previously. A report by Shin *et al*. demonstrated that doping bulk LMO spinel with Cr, Ga, and Fe ions results in surface segregation of the dopant Cr, Ga, and Fe ions, shown by time-of-flight secondary-ion mass spectroscopy (TOF-SIMS) depth profiling.[57] The dopants segregate to the surface to lower the surface energy, and contribute to a more stable SEI during cycling. Therefore, by simple incorporation of Al^{3+} in our nanoporous LAMO solution precursor, we are able to protect the surface.

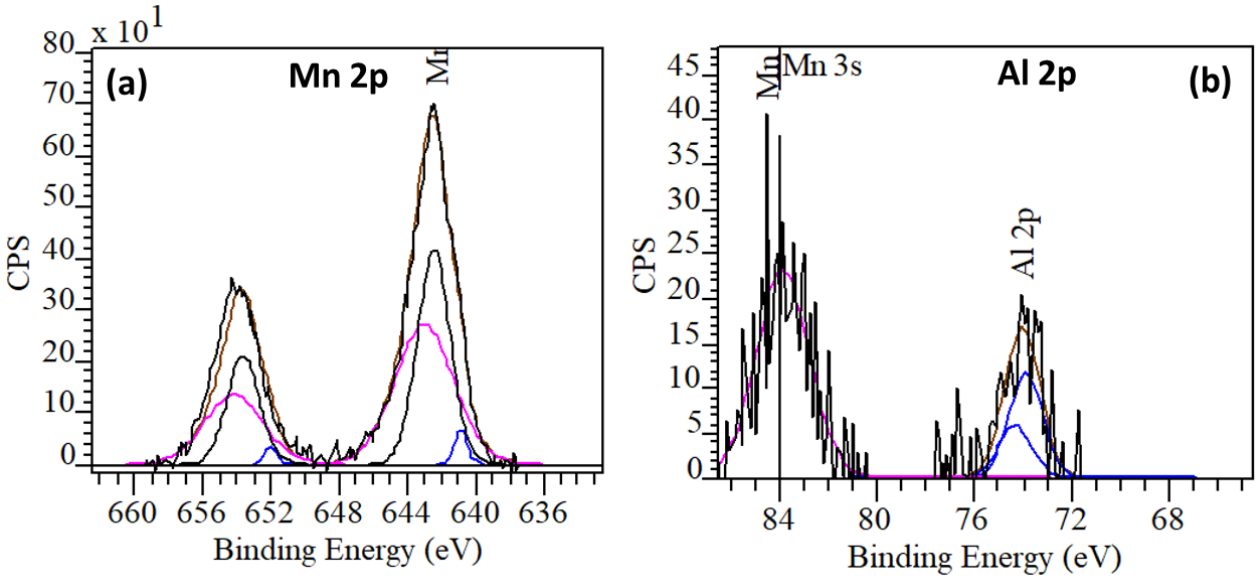

(c)

	surface	after etching
Mn:Al ratio	8.3	12.5

Figure 2.3: XPS data obtained on $LiAl_{0.1}Mn_{1.9}O_4$ for a) Mn and b) Al without surface etching. c) Quantification of the Mn:Al ratio on the surface nanoporous LAMO surface for the as-formed material, and after Ar etching for 1 min.

2.3.2. Electrochemical characterization. Galvanostatic cycling was performed on LMO and LAMO cells at multiple C-rates to measure total charge stored and charge retention at high rates. The first cycle shows a large Coulombic inefficiency (Fig S3) that is attributed to formation of the solid electrolyte interphase (SEI) and some surface Mn^{2+} formation and dissolution. The first cycle inefficiency is improved in LAMO compared to LMO, suggesting that the Al^{3+} doping has improved surface stability. After the first cycle, the cell stabilizes and there is minimal capacity fade. It is interesting to note that the GV curve of LMO (**Fig 2.4a**) has a region near 4.2 V where there is a "kink" where the slope changes. In bulk LMO, this appears as a well-defined plateau at

4.2 V which has been attributed to a Li^+ disorder-to-order phase transition.[58] In contrast, the kink is absent in the GV curve of LAMO (Fig 2.4b), which shows a nearly constant linear slope from 4.3 – 3.9 V. This sloping behavior is characteristic of a solid-solution type intercalation mechanism, suggesting that the addition of Al^{3+} has induced a more gradual lattice expansion to accommodate Li^+ during cycling and has disrupted the disorder-to-order transition. This phase-transition suppression should be favorable for fast charging or pseudocapacitive behavior, as discussed above.

Here we compare discharge (lithiation) capacities as the most accurate representation of the reversible capacity. The pure nanoporous LMO obtained a discharge capacity of 106 mAh/g at 1C and 88 mAh/g at 20C (Fig 2.4a), while LAMO obtains a discharge capacity of 86 mAh/g at 1C and 61 mAh/g at 20C (Fig 2.4b). It is expected that the overall total capacity of LAMO should be lower in comparison to LMO because we are substituting some of the redox active Mn^{3+} with Al^{3+}, which does not undergo redox within this voltage window. Because of the Mn^{3+} disproportionation, the surface of LMO is known to be electrochemically inactive.[41,48] The higher surface area observed for the LAMO is likely thus the primary cause for the slightly lower capacity in that material.[26] By normalizing the capacity at higher C-rates to the measured 1C capacity, we can compare percentage drop of initial capacity. At 20C, corresponding to a full charge within 3 minutes, LMO retains 83% of the initial capacity and LAMO retains 71% of initial capacity, indicating that both are suitable as fast-charging electrodes, and the Al-doping surface stabilization does not hinder the charge transfer process.

The impedance for both samples was measured in the discharged (lithiated) state at 3.5 V (Fig 2.4d). By fitting to an equivalent circuit of $R_1 + \frac{Q_2}{R_2} + Q_3$, the charge transfer resistance of

pure LMO is calculated to be 74 Ohm, while LAMO has a charge transfer resistance of 111 Ohm. Therefore, the Al-doping slightly increases the resistance in comparison to pure LMO, but both are relatively low.

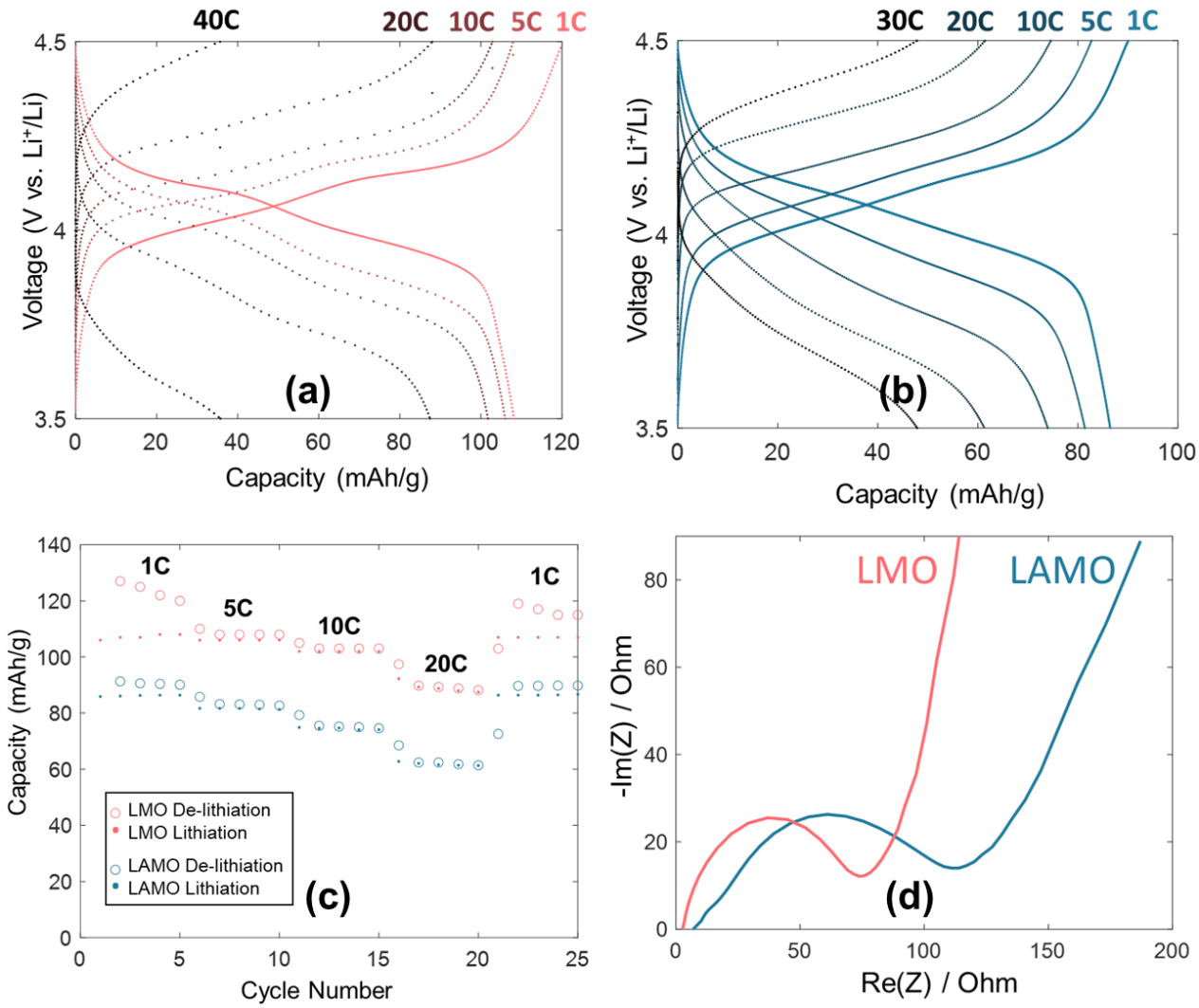

Figure 2.4. a) GV curves for LMO cycled at 1C, 5C, 10C, 20C, and 40C. b) GV curves for LAMO cycled at 1C, 5C, 10C, 20C, and 30C. c) Total capability from GV cycling for both LMO and LAMO during de-lithiation (charge) and lithiation (discharge). d) Nyquist plots showing charge-transfer resistance for LMO and LAMO in the lithiated state at 3.5 V.

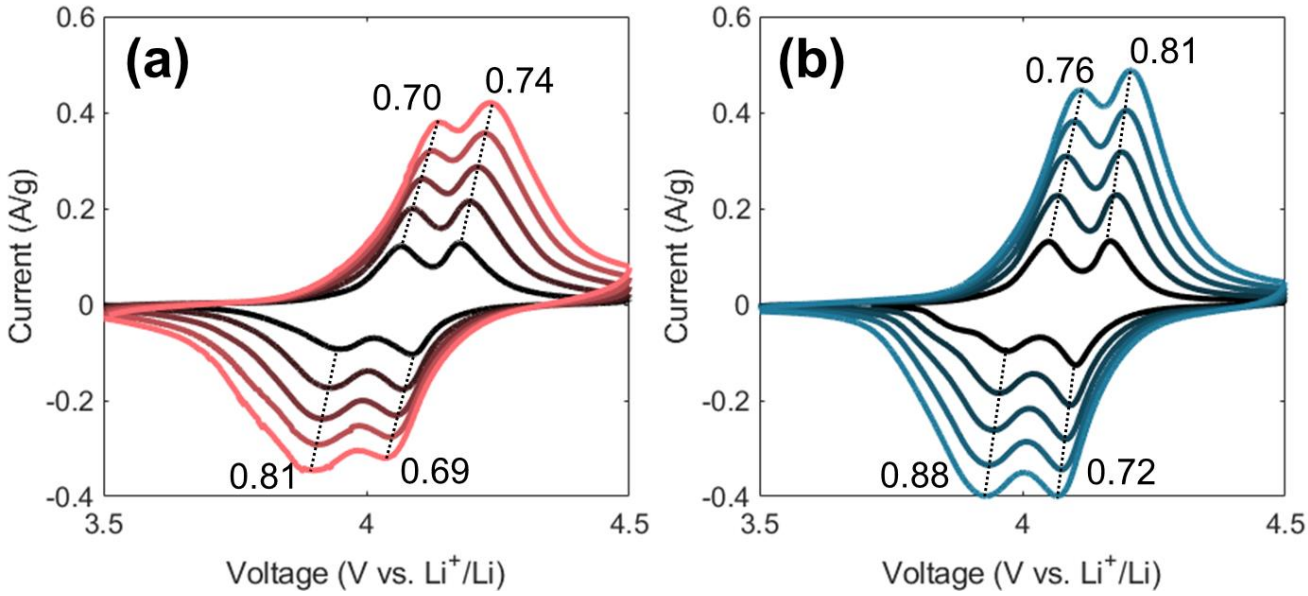

Figure 2.5. CVs taken at 0.1, 0.2, 0.3, 0.4, and 0.5 mV/s for (a) LMO and (b) LAMO. Calculated b-values for each peak are listed near each peak.

To quantify the extent of capacitive versus diffusion-limited charge storage in the material, we utilize a kinetic analysis based on a simplification of the Randles-Sevcik equation.[59] The "b-value analysis" assumes that the current measured in a CV experiment follows the power law of Equation (2.1), where ν is the scan rate and 'a' and 'b' are fitted parameters.[60] By measuring CVs at multiple scan rates and taking the current value at the redox peaks (to account for polarization effects which cause the peaks to shift), we can obtain the value of b from the slope of a linear fit to a plot of log(i) vs. log(ν) (Equation (2.2)).

$$i = a\nu^b \tag{2.1}$$

$$\log(i) = \log(a) + b * \log(\nu) \tag{2.2}$$

The CVs for both LMO (**Fig 2.5a**) and LAMO (Fig 2.5b) were taken at 0.1, 0.2, 0.3, 0.4, and

0.5 mV/s and b-values for both cathodic and anodic peaks have been calculated. For pure LMO, b-values range from 0.70 – 0.81, indicating behavior that is intermediate between diffusion-limited and capacitive charge storage processes. In contrast, the Al-doped sample demonstrates a higher b-value at all redox peaks, ranging from 0.72 – 0.88, indicating somewhat more capacitive charge storage behavior. Therefore, we have confirmed that Al^{3+} doping does not hinder the fast redox reactions in our nanoporous LMO.

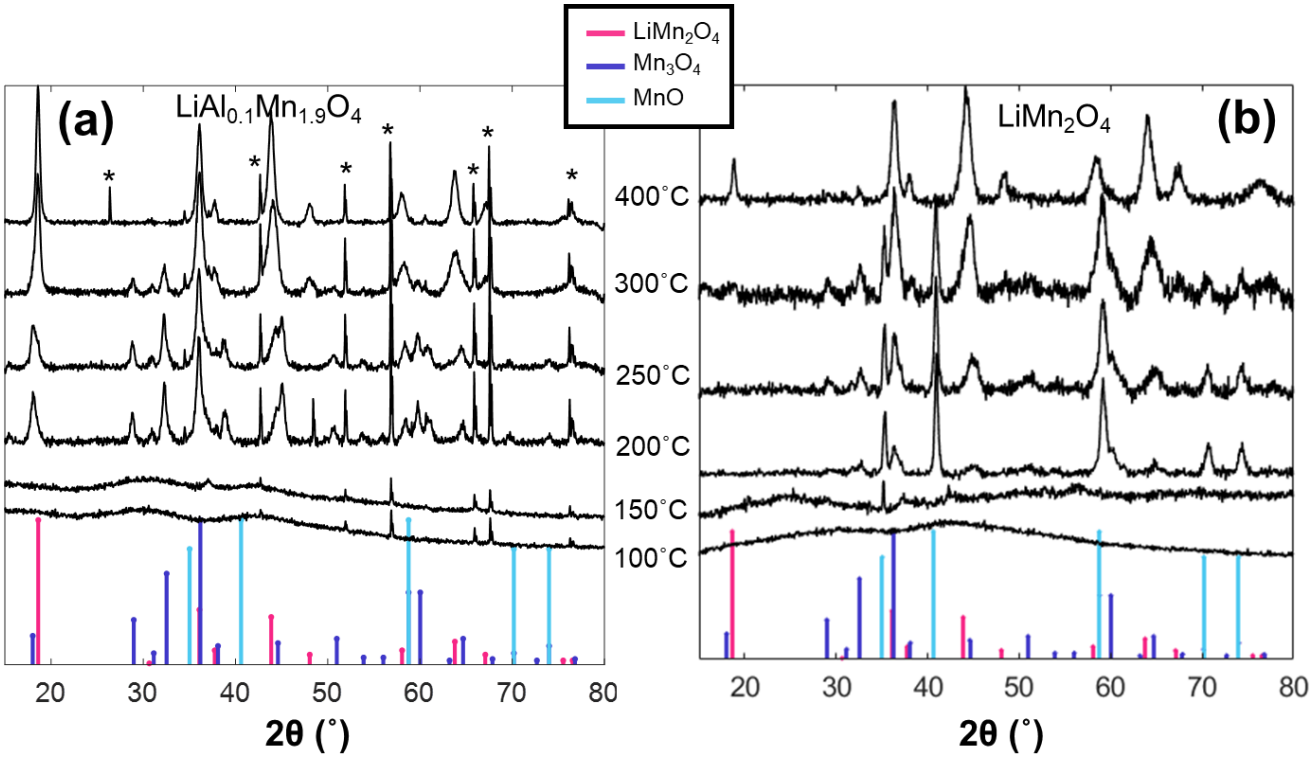

Figure 2.6. Variable temperature XRD obtained on the amorphous gel precursor for nanoporous (a) LAMO and (b) LMO as it is heated to 100˚C, 150˚C, 200˚C, 250˚C, 300˚C, and 400˚C. Sharp peaks marked with * are due to ceramic sample holder. The spinel structure starts to form at 200˚C and is complete by 400˚C in the Al-doped material, while the spinel structure does not form until 400˚C in LMO.

2.3.3. Effect of Al-doping on gel calcination.

To study the crystalline intermediates that form during calcination, the amorphous gel precursors for both nanoporous LMO and LAMO were subjected to *in-situ* high temperature diffraction to follow the crystallization process. XRD patterns were collected at various temperatures during calcination (**Fig 2.6**). Sharp peaks marked with an asterisk correspond to the ceramic sample holder and are more prominent at higher temperatures due to the loss of the PMMA template, which exposes more of the sample holder to X-rays. Both precursors are amorphous until 200˚C when crystalline peaks begin to form. In the pure LMO sample at 200˚C (Fig 2.6ba mixture of MnO (rock salt) and Mn_3O_4 (spinel) forms first, as shown by the peaks appearing at 35˚ and 40.6˚ 2θ for rock salt and at 32.5˚ and 36.2˚ 2θ for Mn_3O_4. At 400˚C, the (111) peak of the spinel structure at 18˚ 2θ first starts to appear, while the MnO has disappeared, and a little bit of Mn_3O_4 remains. Rock salt MnO contains Mn in the (2+) oxidation state, and Mn_3O_4 contains a mixture of Mn(2+, 3+). The final $LiMn_2O_4$ spinel product contains Mn(+3, +4). Therefore, as the temperature is raised, the Mn gets increasingly oxidized, preferring spinel over rock salt as the more stable crystal structure in the oxidized state. For comparison, the LAMO (Fig 2.6a) starts to crystallize with a mixture of MnO, Mn_3O_4, and $LiMn_2O_4$ at 200˚C. The presence of $LiMn_2O_4$ (or $LiAl_{0.1}Mn_{1.9}O_4$) is evidenced by the 18˚ 2θ peak, even at this low temperature. A small amount of MnO is seen by the two peaks at 70˚ and 74˚ 2θ, but most of the crystalline material is already in the spinel structure at 200˚C. By 300˚C, MnO has disappeared, and by 400˚C the Mn_3O_4 is gone, leaving the phase pure $LiAl_{0.1}Mn_{1.9}O_4$ product. In the LMO gel, the spinel $LiMn_2O_4$ has formed at 400˚C, but some Mn_3O_4 impurity phase remains.

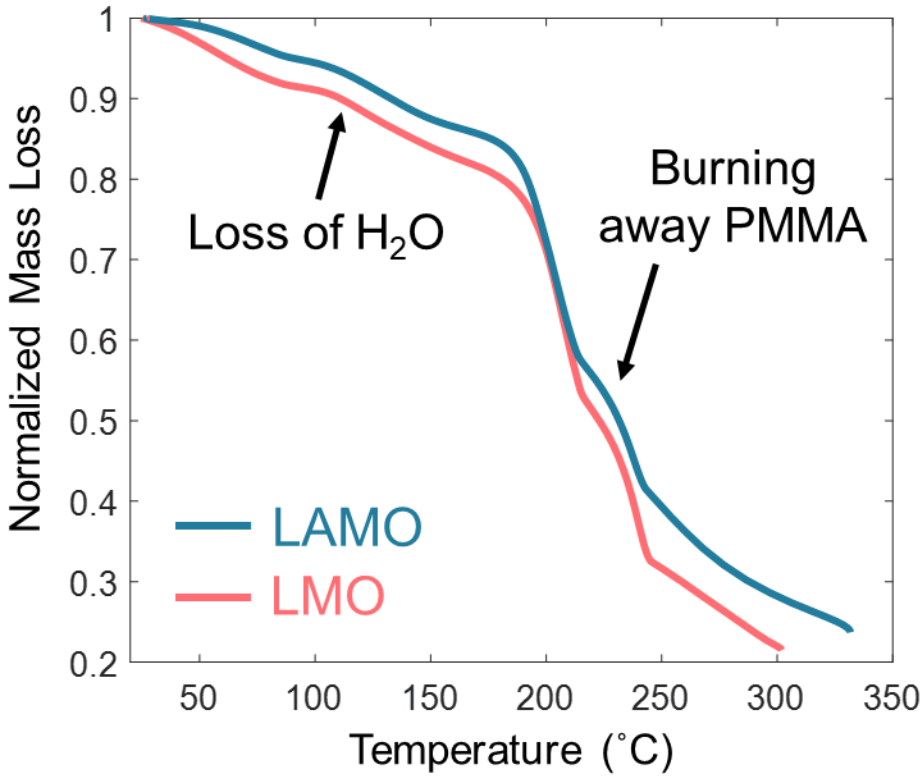

Figure 2.7. TGA performed on dried LMO and LAMO precursor gels. Mass loss has been normalized to the initial mass. The first mass loss event near 100˚C corresponds to drying off residual water that remains in the gel. The steeper mass loss beginning at 180˚C is the onset of PMMA template removal.

Including Al^{3+} in the sol-gel precursor apparently lowers the activation barrier for formation of the spinel and stabilized the structure. In the LAMO gel, crystallization of the spinel happens near or before 200˚C. During the calcination process, TGA of the dried gel shows that PMMA also begins to burn out of the structure near 200˚C (**Fig 2.7**) in both LMO and LAMO. However, in the LAMO reaction, since the spinel structure is already well-formed before PMMA template has been completely removed, a porous network is locked in before any significant

coarsening or rearrangement can happen. In the LMO gel, the PMMA template has burned away by 400˚C but some Mn_3O_4 remains, suggesting that additional heat is needed to fully convert Mn_3O_4 to $LiMn_2O_4$. At these elevated temperatures, the PMMA template has been removed and long-range diffusion still occurs, leading to LMO crystallites coarsening and a decrease in surface area. Therefore, addition of Al^{3+} to the precursor has also stabilized the nanoporous architecture and makes the synthesis of phase pure spinel product more facile.

We note that for LMO and LAMO, higher surface area is not always desirable, because of the high tendency to form an inactive surface layer and the issues with Mn dissolution. The ability to faithfully preserve the templated structure, however, means that surface can be tuned by using larger PMMA colloids to make larger pores with lower surface area.

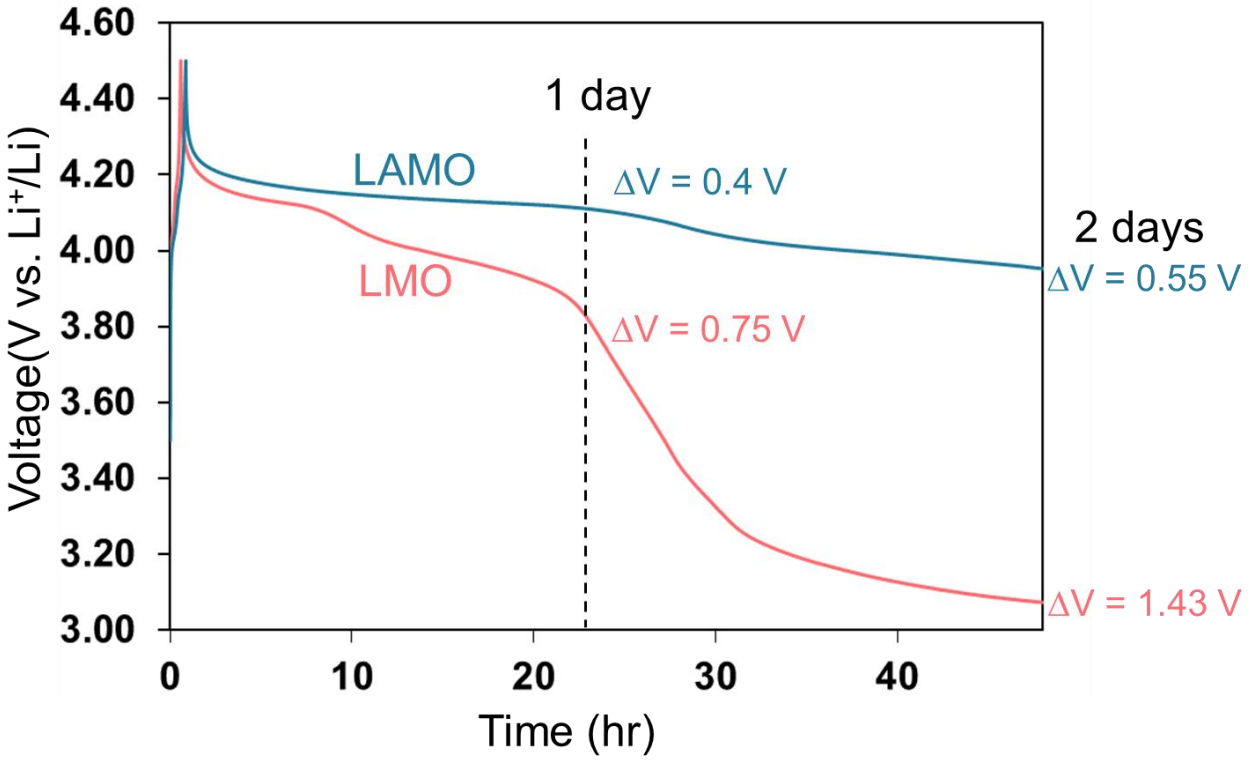

Figure 2.8. Self-discharge tests for nanoporous LAMO and nanoporous LMO. The LMO cathode shows significant capacity fade over the course of two days, while the LAMO is much more stable.

2.3.4. Self-discharge. The spontaneous disproportionation of Mn^{3+} to form Mn^{2+}, which dissolves readily in electrolyte, is the cause of self-discharge in LMO and degradation of active material. Therefore, self-discharge experiments were conducted to determine material stability in the charged state. Cells were charged at 1C to 4.5 V and rested, while the voltage drop was measured over 2 days (**Fig 2.8**). After 24 hours of resting, LMO has already lost 0.75 V, while LAMO has lost 0.4 V. After 48 hours, the difference is even more pronounced as LMO has lost 1.43 V and nearly returned to OCV, while LAMO has lost 0.55V. Although some extent of self-discharge still occurs, we have shown that Al-doping is an effective strategy for mitigating the self-discharge problem without significantly sacrificing conductivity and rate capability.

2.4 Conclusions.

We have synthesized a nanoporous Al-doped LMO spinel ($LiAl_{0.1}Mn_{1.9}O_4$) to mitigate the surface Mn^{2+} dissolution issue through a facile sol-gel method with colloidal PMMA template. The nanoporous LAMO network has a high surface area of 18.8 m^2/g and crystallites on the order of 35 nm, allowing shortened Li^+ diffusion lengths and electrolyte penetration. XPS shows that a greater ratio of Al^{3+} at the surface compared to the interior, confirming that the Al^{3+} dopant has a surface stabilization effect. Variable temperature XRD and TGA on the pre-calcined gel of LMO and LAMO have demonstrated that the Al^{3+} dopant stabilizes the spinel structure near 200˚C, resulting in a well-formed porous network and phase-pure product at lower temperatures. Self-discharging experiments show that, in the charged state, LAMO experiences a 0.55 V drop over two days compared to pure LMO which shows a 1.43 V drop over the same time frame. Rate capability shows that LAMO can retain 71% of its initial capacity at 20C. Therefore, Al-doping

has been shown to be an effective strategy for mitigating self-discharge and improving structural stability in spinel LMO while still maintaining fast-charging performance.

2.5 References.

[1] Blomgren, George E. "The Development and Future of Lithium Ion Batteries." *Journal of the Electrochemical Society*, **2017**, 164, A5019 – A5025.

[2] *National Blueprint for Lithium Batteries 2021 – 2030*; EE-2348; U.S. Department of Energy; 2021, 6 – 11.

[3] United States Congressional Archives – S.5020 Affordable Electric Vehicles for America Act of 2022. https://www.congress.gov/bill/117th-congress/senate-bill/5020 (accessed 2022-12-04)

[4] Rozier, P.; Tarascon, J.M. "Li-Rich Layered Oxide Cathodes for Next-Generation Li-Ion Batteries: Chances and Challenges." *Journal of the Electrochemical Society*, **2015**, 162, 2490 – 2499.

[5] Whittingham, M. Stanley. "Lithium Batteries and Cathode Materials." *Chemical Reviews*, **2004**, 104, 4271 – 4301.

[6] Wang, R.; Chen, X.; Huang, Z.; Yang, J.; Liu, F.; Chu, M.; Liu, T.; Wang, C.; Zhu, W.; Li, S.; Li, S.; Zheng, J.; Chen, J.; He, L.; Jin, L.; Pan, F.; Xiao, Y. "Twin boundary defect engineering improves lithium-ion diffusion for fast-charging spinel cathode materials." *Nature Communications*, **2021**, 12, 3085.

[7] Matsuo, Y.; Kostecki, R.; McLarnon, F. "Surface Layer Formation on Thin-Film $LiMn_2O_4$ Electrodes at Elevated Temperatures." *Journal of the Electrochemical Society*, **2001**, 148, A687 – A692.

[8] Thackeray, M.M.; Johnson, P.J.; de Picciotto, L.A.; Goodenough, J.B. "Electrochemical extraction of lithium from $LiMn_2O_4$." *Materials Research Bulletin*, **1984**, 19, 179 – 187.

[9] Liu, H.; Tian, R.; Jiang, Y.; Tan, X.; Chen, J.; Zhang, L.; Guo, Y.; Wang, H.; Sun, L.; Chu, W. "On the drastically improved performance of Fe-doped $LiMn_2O_4$ nanoparticles prepared by a facile solution-gelation route." *Electrochimica Acta*, **2015**, 180, 138 – 146.

[10] Marchini, F.; Rubi, D.; del Pozo, M.; Williams, F.J.; Calvo, E.J. "Surface Chemistry and Lithium-Ion Exchange in $LiMn_2O_4$ for the Electrochemical Selective Extraction of LiCl from Natural Salt Lake Brines." *Journal of Physical Chemistry C*, **2016**, 120, 29, 15875 – 15883.

[11] Radzi, Z.I.; Arifin, K.H.; Kufian; M.Z.; Balakrishnan, V.; Raihan, S.R.S.; Rahim, N.A.; Subramaniam, R. "Review of spinel $LiMn_2O_4$ cathode materials under high cut-off voltage in lithium-ion batteries: Challenges and strategies." *Journal of Electroanalytical Chemistry*, **2022**, 920, 116623.

[12] Thackeray, M.M; Lee, E.; Shi, B.; Croy, J.R. "Review-From $LiMn_2O_4$ to Partially-Disordered Li_2MnNiO_4: The Evolution of Lithiated-Spinel Cathodes for Li-Ion Batteries." *Journal of the Electrochemical Society*, **2022**, 169, 020535.

[13] Thackeray, M.M; David, W.I.F; Bruce, P.G.; Goodenough, J.B. "Lithium insertion into manganese spinels." *Materials Research Bulletin*, **1983**, 18, 461 – 472.

[14] Thackeray, M.M.; Amine, K. "$LiMn_2O_4$ spinel and substituted cathodes." *Nature Energy*, **2021**, 6, 566.

[15] Thackeray, M.M. "Exploiting the Spinel Structure for Li-ion Battery Applications: A Tribute to John B. Goodenough." *Advanced Energy Materials*, **2021**, 11, 2001117.

[16] Greeley, J.; Warburton, R.E.; Castro, F.C. "Oriented $LiMn_2O_4$ particle fracture from delithiation-driven surface stress." *ACS Applied Materials and Interfaces*, **2020**, 12, 49182 – 49191.

[17] Liu, J.; Wang, X.; Borkiewicz, O.J.; Hu, E.; Xiao, R.-J.; Chen, L.; Page, K. "Unified View of the Local Cation-Ordered State in Inverse Spinel Oxides." *Inorganic Chemistry*, **2019**, 58, 14389 – 14402.

[18] Zhan, C.; Wu, T.; Lu, J.; Amine, K. "Dissolution, migration, and deposition of transition metal ions in Li-ion batteries exemplified by Mn-based cathodes – A critical review." *Energy and Environmental Science*, **2018**, 11, 243 – 257.

[19] Lee, M.-J.; Lee, S.; Oh, P.; Kim, Y.; Cho, J. "High Performance $LiMn_2O_4$ Cathode Materials Grown with Epitaxial Layered Nanostructure for Li-Ion Batteries." *Nano Letters*, **2014**, 14, 993 – 999.

[20] Zhu, Z.; Wang, M.; Meng, Y.; Lin, Z.; Cui, Y.; Chen, W. "A High-Rate Lithium Manganese Oxide-Hydrogen Battery." *Nano Letters*, **2020**, 20, 3278 – 3283.

[21] Young, M. J.; Letourneau, S.; Warburton, R.E.; Dose, W.M.; Johnson, C.; Greeley, J.; Elam, J.W. "High-Rate Spinel $LiMn_2O_4$ (LMO) Following Carbonate Removal and Formation of Li-Rich Interface by ALD Treatment." *Journal of Physical Chemistry C*, **2019**, 123, 23783 – 23790.

[22] Thackeray, M.M.; de Kock, A.; David, W.I.F. "Synthesis and structural characterization of defect spinels in the lithium-manganese-oxide system." *Materials Research Bulletin*, **1993**, 28, 1041 – 1049.

[23] NEI Corporation High Performance Battery Materials – Lithium Manganese Oxide Specification Sheet. https://www.neicorporation.com/products/batteries/cathode-anode-powders/lithium-manganese-oxide. (accessed 2022-12-06)

[24] Abou-Rjeily, J.; Bezza, I.; Laziz, N.A.; Autret-Lambert, C.; Sougrati, M.T.; Ghamouss, F. "High-rate cyclability and stability of $LiMn_2O_4$ cathode materials for lithium-ion batteries from low-cost natural β-MnO_2." *Energy Storage Materials*, **2020**, 26, 423 – 432.

[25] Lu, Q.; Chen, J.G.; Xiao, J.Q. "Nanostructured Electrodes for High-Performance Pseudocapacitors." *Angewandte Chemie – International Edition*, **2013**, 52, 1882 – 1889.

[26] Lesel, B.K.; Cook, J.B.; Yan, Y.; Lin, T.C.; Tolbert, S.H. "Using Nanoscale Domain Size to Control Charge Storage Kinetics in Pseudocapacitive Nanoporous $LiMn_2O_4$ Powders." *ACS Energy Letters*, **2017**, 2, 2293 – 2298.

[27] Fleischmann, S.; Mitchell, J.B.; Wang, R.; Zhan, C.; Jiang, D.-e.; Presser, V.; Augustyn, V. "Pseudocapacitance: From Fundamental Understanding to High Power Energy Storage Materials." *Chemical Reviews*, **2020**, 120, 6738 – 6782.

[28] Conway, B.E.; Pell, W.G. "Double-layer and pseudocapacitance types of electrochemical capacitors and their applications to the development of hybrid devices." *Journal of Solid State Electrochemistry*, **2003**, 7, 637 – 644.

[29] Conway, B.E. "Two-dimensional and quasi-two-dimensional isotherms for Li intercalation and upd processes at surfaces." *Electrochimica Acta*, **1993**, 38, 1249 – 1258.

[30] Conway, B.E.; Gileadi, E. "Kinetic Theory of Pseudo-Capacitance and Electrode Reactions at Appreciable Surface Coverage." *Trans. Faraday Soc.*, **1962**, 28, 2493 – 2509.

[31] Liu, T.-C.; Pell, W.G.; Conway, B.E.; Roberson, S.L. "Behavior of Molybdenum Nitrides as Materials for Electrochemical Capacitors." *Journal of the Electrochemical Society*, **1998**, 145, 1882 – 1888.

[32] Cook, J.B.; Kim, H.-S.; Lin, T.; Lai, C.-H.; Dunn, B.; Tolbert, S.H. "Pseudocapacitive Charge Storage in Thick Compose MoS_2 Nanocrystal-Based Electrodes." *Advanced Energy Materials*, **2017**, 7, 1601283.

[33] Okubo, M.; Mizuno, Y.; Yamada, H.; Kim, J.; Hosono, E.; Zhou, H.; Kudo, T.; Honma, I. "Fast Li-Ion Insertion into Nanosized $LiMn_2O_4$ without Domain Boundaries." *ACS Nano*, **2010**, 4, 741 – 752.

[34] Cook, J.B.; Lin, T.C.; Kim, H.-S.; Siordia, A.; Dunn, B.S.; Tolbert, S.H. "Suppression of Electrochemically Drive Phase Transitions in Nanostructured MoS_2 Pseudocapacitors Probed Using Operando X-ray Diffraction." *ACS Nano*, **2019**, 13, 1223 – 1231.

[35] Kim, H.-S.; Cook, J.B.; Tolbert, S.H.; Dunn, B.S. "The Development of Pseudocapacitive Properties in Nanosized-MoO_2." *Journal of the Electrochemical Society,* **2015**, 162, A5083 – A5090.

[36] Massarotti, V.; Capsoni, D.; Bini, M.; Chiodelli, G. "Characterization of Sol-Gel $LiMn_2O_4$ Spinel Phase." *Journal of Solid State Chemistry,* **1999**, 147, 509 – 515.

[37] Barboux, P.; Tarascon, J.M.; Shokoohi, F.K. "The Use of Acetates as Precursors for the Low-Temperature Synthesis of $LiMn_2O_4$ and $LiCoO_2$ Intercalation Compounds." *Journal of Solid State Chemistry,* **1991**, 94, 185 – 196.

[38] Li, X.; Cheng, F.; Guo, B.; Chen, J. "Template-Synthesized $LiCoO_2$, $LiMn_2O_4$, and $LiNi_{0.8}Co_{0.2}O_2$ Nanotubes as the Cathode Materials of Lithium Ion Batteries." *Journal of Physical Chemistry B,* **2005**, 109, 14017 – 14024.

[39] Hunter, James C. "Preparation of a New Crystal Form on Manganese Dioxide: λ-MnO_2." *Journal of Solid State Chemistry,* **1981**, 39, 142 – 147.

[40] Benedek, R. and M. M. Thackeray. "Simulation of the surface structure of lithium manganese oxide spinel." *Physical Review B,* **2011**, 83, 195439.

[41] Amos, C.D.; Roldan, M.A.; Varela, M.; Goodenough, J.B.; Ferreira, P.J. "Revealing the Reconstructed Surface of $Li[Mn_2]O_4$." *Nano Letters,* **2016**, 16, 2899 – 2906.

[42] Tang, X.; Zhou, J.; Bai, M.; Wu, W.; Li, S.; Ma, Y. "Investigation of the self-discharge behaviors of the $LiMn_2O_4$ cathode at elevated temperatures: in situ X-ray diffraction analysis and a co-doping mitigation strategy." *Journal of Materials Chemistry A,* **2019**, 7, 13364 – 13371.

[43] Marincas, A.H.; Ilea, P. "Enhancing Lithium Manganese Oxide Electrochemical Behavior by Doping and Surface Modifications." *Coatings,* **2021**, 11, 456.

[44] Finegan, D.P.; Vamvakeros, A.; Tan, C. Heenan, T.M.M.; Daemi, S.R.; Seitzman, N.; Michiel, M.; Jacques, S.; Beale, A.M.; Brett, D.J.L.; Shearing, P.R.; Smith, K. "Spatial quantification of dynamic inter and intra particle crystallographic heterogeneities within lithium ion electrodes." *Nature Communications,* **2020**, 11, 631.

[45] Manthiram, A.; Chemelewski, K.; Lee, E.-S. "A perspective on the high-voltage $LiMn_{1.5}Ni_{0.5}O_4$ spinel cathode for lithium-ion batteries." *Energy & Environmental Science*, **2014**, 7, 1339 – 1350.

[46] Bassett, K.L.; Warburton, R.E.; Deshpande, S.; Fister, T.T.; Ta, K.; Esbenshade, J.L.; Kinaci, A.; Chan, M.K.Y.; Wiaderek, K.M.; Chapman, K.W.; Greeley, J.P.; Gewirth, A.A. "Operando Observations and First-Principles Calculations of Reduced Lithium Insertion in Au-Coated $LiMn_2O_4$." *Advanced Materials Interfaces,* **2019**, 6, 1801923.

[47] Xiao, Y.; Zhang, X.-D.; Zhu, Y.-F.; Wang, P.-F.; Yin, Y.-X.; Yang, X.; Shi, J.-L.; Liu, J.; Li, H.; Guo, X.-D.; Zhong, B.-H.; Guo, Y.-G. "Suppressing Manganese Dissolution via Exposing

Stable {111} Facets for High-Performance Lithium-Ion Oxide Cathode." *Advanced Science*, **2019**, 6, 1801908.

[48] Hirayama, M.; Ido, H.; Kim, K.; Cho, W.; Tamura, K.; Mizuki, J.; Kanno, R. "Dynamic Structural Changes at $LiMn_2O_4$/Electrolyte Interface during Lithium Battery Reaction." *Journal of American Chemical Society*, **2010**, 132, 15268 – 15276.

[49] Lee, Y.-S.; Kumada, N.; Yoshio, M. "Synthesis and characterization of lithium aluminum-doped spinel ($LiAl_xMn_{2-x}O_4$) for lithium secondary battery." *Journal of Power Sources*, **2001**, 96, 376 – 384.

[50] Hendriks, R.; Cunha, D.M.; Singh, D.P.; Huijben, M. "Enhanced Lithium Transport by Control of Crystal Orientation in Spinel $LiMn_2O_4$ Thin Film Cathodes." *ACS Applied Energy Materials*, **2018**, 1, 7046 – 7051.

[51] Kim, S.; Aykol, M.; Wolverton, C. "Surface phase diagram and stability of (001) and (111) $LiMn_2O_4$ spinel oxides." *Physical Review B*, **2015**, 92, 115411.

[52] Duncan, H.; Hai, B.; Leskes, M.; Grey, C.P.; Chen, G. "Relationships between Mn^{3+} Content, Structural Ordering, Phase Transformation, and Kinetic Properties in $LiNi_xMn_{2-x}O_4$ Cathode Materials." *Chemistry of Materials*, **2014**, 26, 5374 – 5382.

[53] Wang, J.L.; Li, Z.H.; Yang, J.; Tang, J.J.; Yu, J.J.; Nie, W.B.; Lei, G.T.; Xiao, Q.Z. "Effect of Al-doping on the electrochemical properties of a three-dimensionally porous lithium-manganese oxide for lithium-ion batteries." *Electrochimica Acta*, **2012**, 75, 115 – 122.

[54] Wang, T.; Sel, O.; Djerdj, I.; Smarsly, B. "Preparation of a large Mesoporous CeO_2 with crystalline walls using PMMA colloidal crystal templates." *Colloid and Polymer Science*, **2006**, 285, 1 – 9.

[55] Lai, C.-H.; Ashby, D.S.; Lin, T.C.; Lau, J.; Dawson, A.; Tolbert, S.H.; Dunn, B. "Application of Poly(3-hexylthiophene-2,5-diyl) as a Protective Coating for High Rate Cathode Materials." *Chemistry of Materials*, **2018**, 30, 2589 – 2599.

[56] Baes, Charles F.; Mesmer, Robert E. *The Hydrolysis of Cations*; John Wiley & Sons, 1976.

[57] Shing, D.W.; Bridges, C.A.; Huq, A.; Paranthaman, M.P.; Manthiram, A. "Role of Cation Ordering and Surface Segregation in High-Voltage Spinel $LiMn_{1.5}Ni_{0.5-x}M_xO_4$ (M = Cr, Fe, and Ga) Cathodes for Lithium-Ion Batteries." *Chemistry of Materials*, **2012**, 24, 3720 – 3731.

[58] Wohlfahrt-Mehrens, M.; Butz, A.; Oesten, R.; Arnold, G.; Hemmer, R.P.; Huggins, R.A. "The influence of doping on the operation of lithium manganese oxide spinel." *Journal of Power Sources*, **1997**, 68, 582 – 585.

[59] Bard, A.J. and Larry R. Faulkner. *Electrochemical Methods: Fundamentals and Applications*; John Wiley & Sons, Inc, 1980.

[60] Lindström, H.; Södergren, S.; Solbrand, A.; Rensmo, H.; Hjelm, J.; Hagfeldt, A.; Lindquist, S.-E. "Li^+ Ion Insertion in TiO_2 (Anatase). 2. Voltammetry on Nanoporous Films". *Journal of Physical Chemistry B,* **1997**, 101, 7717-7722.

CHAPTER 3: Crystal Size and Lattice Disorder as Design Principles for the Suppression of Intercalation-Induced Phase Transitions in Pseudocapacitive Mesoporous MoS_2

3.1 Introduction.

As we move towards replacing traditional combustion engine-based vehicles with electric vehicles (EVs), some drawbacks inhibiting widespread usage of EVs are the short driving range and long charging times.[1] These limitations are a direct result of the slow Li-ion diffusion rate in bulk battery materials. Li-ion batteries (LIB) reach full charge within hours but re-fueling a gasoline-powered vehicle takes only minutes. This disparity highlights the need for energy storage devices that can support both high energy density and power density. A class of materials attracting increasing interest, pseudocapacitors offer higher energy density than electric double layer capacitors (EDLCs) by undergoing redox, while simultaneously providing higher power density than standard LIB materials.[2-3]

Conventional LIB materials store charge through Faradaic redox reactions occurring in the entire bulk material. This mechanism affords high energy density, but the power density is limited by slow solid-state Li^+ diffusion. As Li^+ is inserted, at some critical Li^+ concentration, a first-order phase transformation occurs between the Li-poor and Li-rich phases.[4-6] The intercalation-induced phase transformation requires symmetry breaking and large rearrangements of the crystal lattice and limits kinetic performance since the Li^+ diffusion rate is linked to the movement of the phase boundary. Repeated charging and discharging with large structural changes also induce stress in the material and long-term capacity fade.

Pseudocapacitors also store charge through redox reactions, but the rate performance is no longer limited by semi-infinite diffusion. This can often be achieved by nanostructuring a battery

material so that more redox occurs near the surface and ion diffusion lengths are shortened. As a result, the material can charge within minutes, and the electrical response of a pseudocapacitive material more closely resembles that of a capacitor. This can be observed in a plot of the voltage vs. charge stored during galvanostatic cycling (GV), where a capacitor shows a linear response as function of charge, while a battery material exhibits voltage plateaus at the redox potential where a phase transformation occurs. These two mechanisms can also be distinguished in the cyclic voltammogram (CV), where a battery material shows large peak currents near the redox potentials but little current elsewhere in the potential window. In contrast, a capacitor shows a broad current response throughout the entire voltage window, resulting in a more "box-like" CV. A pseudocapacitive material often exhibits a pseudo-linear GV curve, indicating lack of intercalation-induced phase transitions, and a nearly rectangular CV with significantly broadened redox peaks. Therefore, a pseudocapacitor utilizes the charge storage mechanism of a battery while demonstrating electrochemical performance like a capacitor. Most importantly, an essential structural feature of pseudocapacitive materials is the suppression of first-order phase transition upon Li (de-)intercalation.

Numerous studies have shown that by decreasing the crystallite size of conventional battery materials, pseudocapacitive charge storage (or fast-charging rate performance) can be achieved in materials such as $LiCoO_2$,[7] MoO_2,[8] TiS_2,[9] nanocrystal MoS_2,[10] and others. In an ion intercalation host, the diffusion coefficient, *D*, is related to the diffusion length, *L*, by the Equation (3.1) for time constant, τ_d, which represents a characteristic time scale for diffusion.

$$\tau_d = \frac{L^2}{D} \tag{3.1}$$

Decreasing the crystal size can be seen as effectively shortening the diffusion length that intercalating ions must travel, thereby speeding up the charging and discharging time. The diffusion coefficient is also a kinetic rate constant for Li hopping through lattice sites and can be expressed as a function of the hopping activation energy barrier by Equation (3.2).[11-12]

$$D = D_0 e^{\frac{-E_a}{k_B T}} \quad (3.2)$$

To increase the diffusion coefficient, we also consider material design principles that modify the energy landscape and lower the barrier for traversing the crystal structure.

One strategy is to intentionally incorporate disorder into the crystal. An extensively studied example of this approach is the development of the fast-charging layered cathode material, $LiNi_{0.80}Co_{0.15}Al_{0.05}O_2$ (NCA), from parent structures $LiNiO_2$ and $LiCoO_2$ by introducing substitutional disorder in the form of cation dopants.[13-14] Both $LiNiO_2$ and $LiCoO_2$ undergo first-order phase transformations during Li cycling, evidenced by distinct voltage plateaus in the GV profile and *operando* x-ray diffraction (XRD) studies.[15-16] However, the inclusion of both cations and Al^{3+} results in stabilization of the crystal lattice, solid-solution Li intercalation behavior, and an increase in the diffusion coefficient.[17] Another example of disorder enabling faster Li diffusion is the reduction of MoO_3 to pseudocapacitive MoO_{3-x} by including oxygen vacancies.[18] Besides these examples, a systematic understanding of how disorder leads to pseudocapacitive charge storage is lacking. Therefore, we aim to elucidate the role of both size and disorder effects in enabling pseudocapacitive charge storage.

Molybdenum disulfide (MoS_2) is a layered van der Waals (vdW) material that has demonstrated success as a Li^+ intercalation material due to its tunable vdW gap size. Many studies focus on its four-electron conversion reaction reducing MoS_2 to Mo metal and Li_2S by cycling

down to 0.0 V vs Li^+/Li.[19-21] Although this reaction provides a high gravimetric capacity, it results in large structural distortions and poor reversibility. Therefore, we focus on the highly reversible one-electron intercalation reaction occurring between 1.0 – 2.7 V with a theoretical capacity of 167 mAh g^{-1}.[22] MoS_2 has been synthesized in a variety of architectures such as exfoliated graphene-like sheets,[23-24] nanoparticles, [25-26] nanorods,[27-28] thin films,[29] nanoflowers[30-31] which have shown improved Li^+ insertion performance compared to bulk MoS_2.[32] This faster and more reversible Li^+ intercalation in MoS_2 nanostructures has been attributed to the higher surface area, shortened diffusion length, and expanded vdW gap size, enabling faster ion diffusion. However, it has been difficult to resolve to what extent pseudocapacitive charge storage in nanostructured MoS_2 is caused by the reduced crystal size as opposed to lattice disorder because nano-MoS_2 also tends to be significantly disordered. The disorder may take the form of stacking faults, expanded vdW layer spacing, vacancies, strain, and more.

As synthesized, MoS_2 exists in the 2H structure, where the molybdenum atom exists in a trigonal prismatic coordination environment with the six neighboring sulfur atoms.[33] Upon intercalation of Li^+ during the first few cycles, an irreversible phase transition from the 2H to the 1T phase occurs where the sulfur planes glide and the molybdenum atom is now in an octahedral coordination environment.[34-36] Li^+ insertion is also accompanied by reduction of Mo(IV) to Mo(III) which changes the band structure from the semiconducting 2H to metallic 1T phase.[37-38] Therefore, it is important to complete transformation of all the material to the 1T phase before rate cycling and to differentiate the 2H to 1T phase transition (evidenced by a voltage plateau at ~ 1.1 V vs Li^+/Li) from the reversible Li intercalation reaction that will be discussed throughout this paper.

In this paper, we have synthesized a set of mesoporous MoS_2 samples with controlled size and disorder to deconvolute the contribution of both these effects in enabling pseudocapacitive charge transfer. We demonstrate that both reducing the crystal size and introducing lattice disorder can cause suppression of Li-intercalation induced phase transitions and synergistically enhance kinetic performance. Overall, this work suggests that either nanoscale size or crystal disorder can lead to pseudocapacitive properties, but the mechanism by which they do so may vary significantly.

3.2 Experimental.

Materials: Ammonium molybdate (para) tetrahydrate $(NH_4)_6Mo_7O_{24}•4H_2O$ (99%, Alfa Aesar), ammonium persulfate (APS) (98%, Alfa Aesar), ammonium lauryl sulfate (ALS) (~30% in H_2O, Sigma Aldrich), methyl methacrylate (MMA) (contains ≤30 ppm MEHQ as inhibitor, 99%, Sigma Aldrich). Bulk MoS_2 was purchased from Beantown Chemical and stored inside an Ar glovebox. H_2S for sulfurization was purchased as a mixture of H_2 (95%)/H_2S (5%) from Airgas.

3.2.1 Synthesis of poly(methyl methacrylate) (PMMA) colloids: PMMA colloids 60 – 80 nm in diameter were used as organic template to create a porous structure in the MoO_2 precursor. The synthesis is adapted from Wang *et al.*[39] A three-neck flask fitted with a condenser and septum was loaded with 165 mL of milliQ water, 0.3 mL of ALS solution, and 0.075 g of APS. The solution was bubbled under N_2 for 20 – 30 mins while stirring to remove O_2 and prevent premature polymerization. Then, the three-neck flask with MMA was heated in an oil bath to 65˚C, and 12.55 mL MMA was injected. After, the reaction was stirred and heated at 70 – 75˚C for 1 hour. The final colloid solution was purified by liquid-liquid extraction in a separatory funnel with hexanes

to remove any unreacted precursors. Size of the colloids was confirmed by scanning electron microscopy. Mass density of the colloid solution was measured using thermogravimetric analysis (TGA).

3.2.2.a Synthesis of mesoporous MoO_2 precursor: Mesoporous MoO_2 was used as the precursor for the small disordered (sd) and small crystalline (sc) samples. In a typical synthesis, 200 mg ammonium molybdate tetrahydrate was dissolved in the PMMA solution with a fixed amount of PMMA.[40] The precursor solution was frozen by adding dropwise to liquid nitrogen. Once frozen, the solution was lyophilized for at least 12 hours to obtain a dried white powder. The dried powder was calcined under Ar at 675˚C for 1 hour to burn out polymer templates and crystallize the porous MoO_2. The MoO_2 product was a black powder.

3.2.2.b Synthesis of α-MoO_3 nanoparticle precursor: Nanoparticle MoO_3 was used as the precursor for the large disordered (LD) and large crystalline (LC) samples. The method is adapted from Nagabhushana *et al*.[41] Approximately 3 g (2.5 mmol) of ammonium molybdate tetrahydrate was dissolved in de-ionized water and stirred for 30 mins at RT. 5 mL of 2 M nitric acid was added to reach pH ~ 1, causing the remaining precursor to complete dissolution and the solution to clear up. Then the solution was heated at low heat (~ 60˚) for 1 hour. The h-MoO_3 product, a white powder, was washed with milliQ water and centrifuged for 10 mins at 4000 rpm. The h-MoO_3 was heated to 450˚C in a muffle furnace and soaked at 450˚C for 6 hours to produce α-MoO_3, a white powder with a grey tint.

3.2.3. Sulfurization of mesoporous MoO_2/MoO_3 to MoS_2**:** Approximately 50 mg of mesoporous MoO_2 or nanoparticle MoO_3 was ground up with mortar and pestle to expose more surface area to flowing gas. The powder was loaded into a graphite boat and placed in a tube furnace. The furnace atmosphere was purged with Ar for 30 mins to remove O_2. Then the atmosphere was changed to a mixture of H_2 (95%) /H_2S (5%) (**Figure 3.1**). The oven was ramped to 700˚C in 1 hour and soaked for 12 hours to produce the disordered samples. The crystalline samples were annealed at 900˚C and soaked for 12 hours. Once the furnace cooled down, the atmosphere was flushed again with Ar for 30 mins to remove any traces of H_2S. The MoS_2 product was a gray powder.

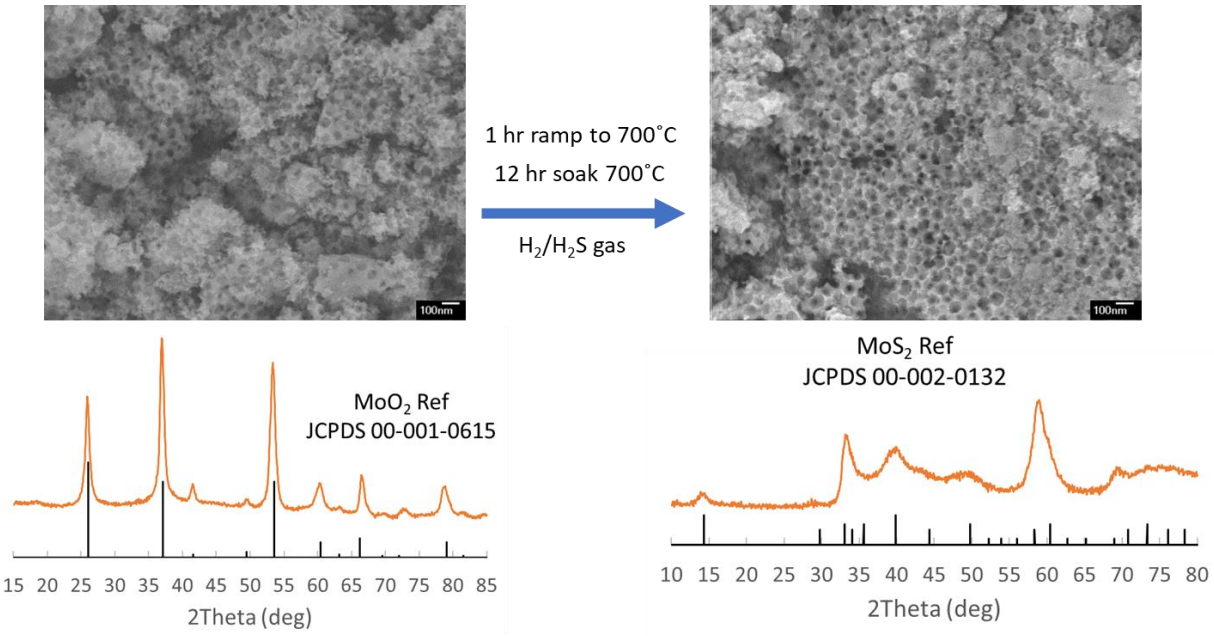

Figure 3.1. SEM image and XRD pattern of MoO_2 precursor and MoS_2 product, demonstrating preservation of pore structure.

3.2.4. Raw material characterization**:** Scanning electron microscopy (SEM) images were obtained using a JEOL model 6700F electron microscope. X-ray diffraction (XRD) patterns were collected

with a PANalytical X'Pert Pro diffractometer operating with Cu Kα (λ = 1.5418 Å) using a 0.05° step size, an accelerating voltage of 45 kV, and a current of 40 mA. XRD patterns were collected from 10 – 80˚. Nitrogen porosimetry was carried out using a Micromeritics TriStar II 3020 porosimeter.

3.2.5. Total scattering (TS) / pair distribution function (PDF) analysis: Powder samples of MoS_2 were submitted to the mail-in program at the Advanced Photon Source (APS) Beamline 11-ID-B for ambient measurements. Powder was loaded into 1.1 mm Kapton capillaries, which were sealed with epoxy on both ends. X-ray energy of 58.6 keV (λ = 0.2115 Å) was used. CeO_2 was used as a calibration standard. 2D data calibration, integration, and Fourier transform to obtain PDF was done in GSAS-II.[42] PDFgui was used to simulate reference phase PDF patterns and refine structural parameters of experimental PDF data.[43] Crystal structures for the 2H and 3R MoS_2 (Schonfeld, COD ID: 9007660) and Petkov $LiMoS_2$ (Petkov, COD ID: 1531962) phases were obtained from Crystallography Open Database.[44-45] Crystal structures for 1T-MoS_2 and triclinic $LiMoS_2$ (material ID: mp-30248) were obtained from Materials Project Database.[46] An expanded layer model was constructed by expanding the unit cell of the 2H phase to a 2 x 2 supercell and removing a layer of S-Mo-S units. Although we recognize this model is likely not an energetic minimum, it is sufficient for modelling the changes in scattering intensity as layers of MoS_2 are no longer correlated. Values of Q_{damp} = 0.038 and Q_{braod} = 0.02 were used to correct for instrument broadening.

3.2.6. Electrode fabrication and electrochemical cycling**:** Slurry was composed of 70% active material, 10% carbon black, 10% carbon nanofibers, and 10% polyacrylic acid (PAA) as the

binder. Dry powders were first ground up in a mortar and pestle several times. PAA was added as a 3% by mass solution in benzyl alcohol. The wet mixture was ground up several more times until it became a viscous paste. Slurries were cast using a doctor blade onto carbon-coated aluminum foil with ~1 mg/cm^2 mass loading and dried overnight in a vacuum oven at 140˚C to remove residual solvent. Electrode discs with area of 0.71 cm^2 were punched out and assembled inside an Ar-filled glovebox into 2032 coin cells with 2 stainless steel spacers, a stainless steel spring, and a glass fiber separator. Polished Li foil was used as the counter and reference electrode. Commercial grade 1 M $LiPF_6$ in 1:1 ethylene carbonate (EC):dimethylene carbonate (DMC) was purchased from Sigma-Aldrich and used as the electrolyte. Before any electrochemical characterization, all samples were first pre-conditioned by galvanostatic cycling (GV) at 1C ten times to completely transform 2H-MoS_2 to 1T-MoS_2 for good conductivity (**Figure 3.2**). GV was performed from between 1.0 – 2.7 V (vs. Li/Li$^+$) at multiple C-rates (1C, 5C, 10C, 20C, 40C, 60C, 80C, 100C), normalized to the theoretical capacity for Li$^+$ insertion of 167 mAh/g. Cyclic voltammetry (CV) data was collected between 1.0 – 3.0 V (vs Li/Li$^+$) at multiple scan rates (0.1, 0.2, 0.3, 0.4, 0.5, 1.0 mV/s) to perform kinetic analyses. To estimate diffusion coefficient as a function of state of charge (SOC), galvanostatic intermittent titration technique (GITT) was performed. For the GITT experiment, cells were first de-lithiated to 2.7 V using C/2 current, then a C/10 current pulse was applied for 30 mins followed by a 2 hr rest period (no current applied). The pulse-rest-pulse-rest sequence was repeated until the cell reached 1.0 V.

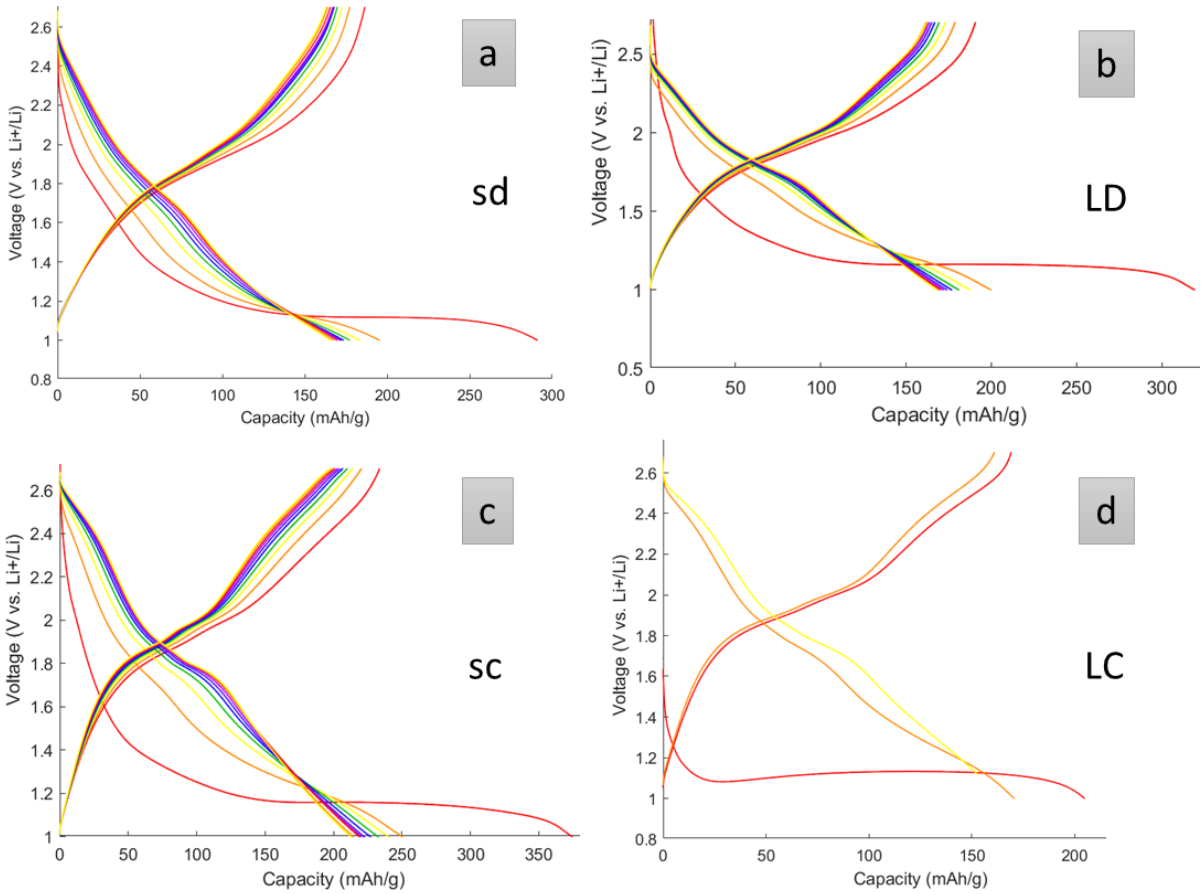

Figure 3.2. Galvanostatic traces of 1C preconditioning for (a) small disordered, (b) large disordered, (c) small crystalline, and (d) large crystalline MoS_2. Voltage plateau at 1.1 V on first cycle corresponds to 2H → 1T phase transition.

3.2.7. Operando XRD**:** *Operando* diffraction experiments were conducted at the Advanced Photon Source (APS) and Stanford Synchrotron Radiation Lightsource (SSRL). Two electrochemical cell constructions were tested: a modified coin cell and pouch cells. For modified coin cells, the outer casing for positive and negative electrodes were machined with a 1/8 hole in center, taped over with Kapton, while the two 0.5 mm spacers inside the cell were machined with 3/16 holes in center.

Pouch cells were made of aluminized mylar, Ni and Al leads, and glass fiber separator. 1M $LiPF_6$ in EC:DMC was used as electrolyte. Li metal was used as counter and reference electrode. Pouch cells were pressurized using beryllium windows during operation. X-ray energy at SSRL beamline 11-3 was 12.7 keV ($\lambda = 0.9763$ Å). Exposure time to x-rays at SSRL ranged from 30 – 60 seconds. X-ray energy at APS beamline 17-BM is 51.5 keV ($\lambda = 0.24075$ Å). Exposure time to x-rays at APS ranged from 3 – 10 seconds. All cells were cycled at 1C unless otherwise noted. LaB_6 placed at the same sample-to-detector distance as the electrodes was used as calibration standard. Data integration and reduction was performed using GSAS-II.[43] Peak fitting was performed in Igor.

3.3 Results and Discussion.

3.3.1. Material Characterization

A set of four representative samples of MoS_2 were synthesized and compared to de-convolute the effects of size and disorder. The small disordered (sd) and small crystalline (sc) samples were synthesized using gas-phase sulfurization of crystalline mesoporous MoO_2. Compared to direct crystallization, this method allows for improved retention of nanoscale architecture and introduction of crystal disorder in the resulting MoS_2.[47] The large disordered (LD) and large crystalline (LC) sample was produced through the same gas-phase sulfurization process on MoO_3 nanoparticles.

SEM images of the small disordered (**Figure 3.3a**) and small crystalline (Figure 3.3c) samples show a well-preserved porous structure with pore wall thicknesses around 20 nm. Large disordered (Figure 3.3b) and large crystalline (Figure 3.3d) samples show particle sizes 200 – 400 nm in diameter. X-ray diffraction (XRD) patterns of synthesized mesoporous MoS_2 (Figure 3.3e)

match JCPDS reference 2-0132 for MoS_2. No remaining MoO_2 or MoO_3 impurities are observed in the XRD, demonstrating the reaction goes to completion. There is significant peak broadening and overlap, such that only the (002) peak at 14.4˚ is well-resolved. By fitting the (002) peak to a Voigt function and using the full width at half max (FWHM) in the Scherrer equation, an average particle size was estimated to be ~ 5 nm.

The observed size in SEM is much larger than the size predicted by the Scherrer equation, suggesting that the diffraction broadening is dominated by lattice disorder effects rather than size alone. Because size and disorder both contribute to peak broadening in the XRD, the calculated "size" from the Scherrer equation is more suitably called a "crystalline coherence length." The lattice disorder can also be directly observed in the high-resolution transmission electron microscopy (HR-TEM) images (Figure 3.3f,g), showing different orientations of lattice planes in the LD sample. The large amount of lattice disorder in these samples is typical of many MoS_2 nanomaterials.[**Error! Bookmark not defined.**,20,23-31] Since the large samples also show some peak broadening, it is likely that disorder is introduced during the sulfurization process. The conversion of the existing crystal domains of MoO_2 or MoO_3 to MoS_2 can result in a strained, disordered lattice, even when the physical particle size remains large. For reference, the XRD pattern of bulk MoS_2 (**Figure 3.4**) shows very narrow and well-resolved peaks.

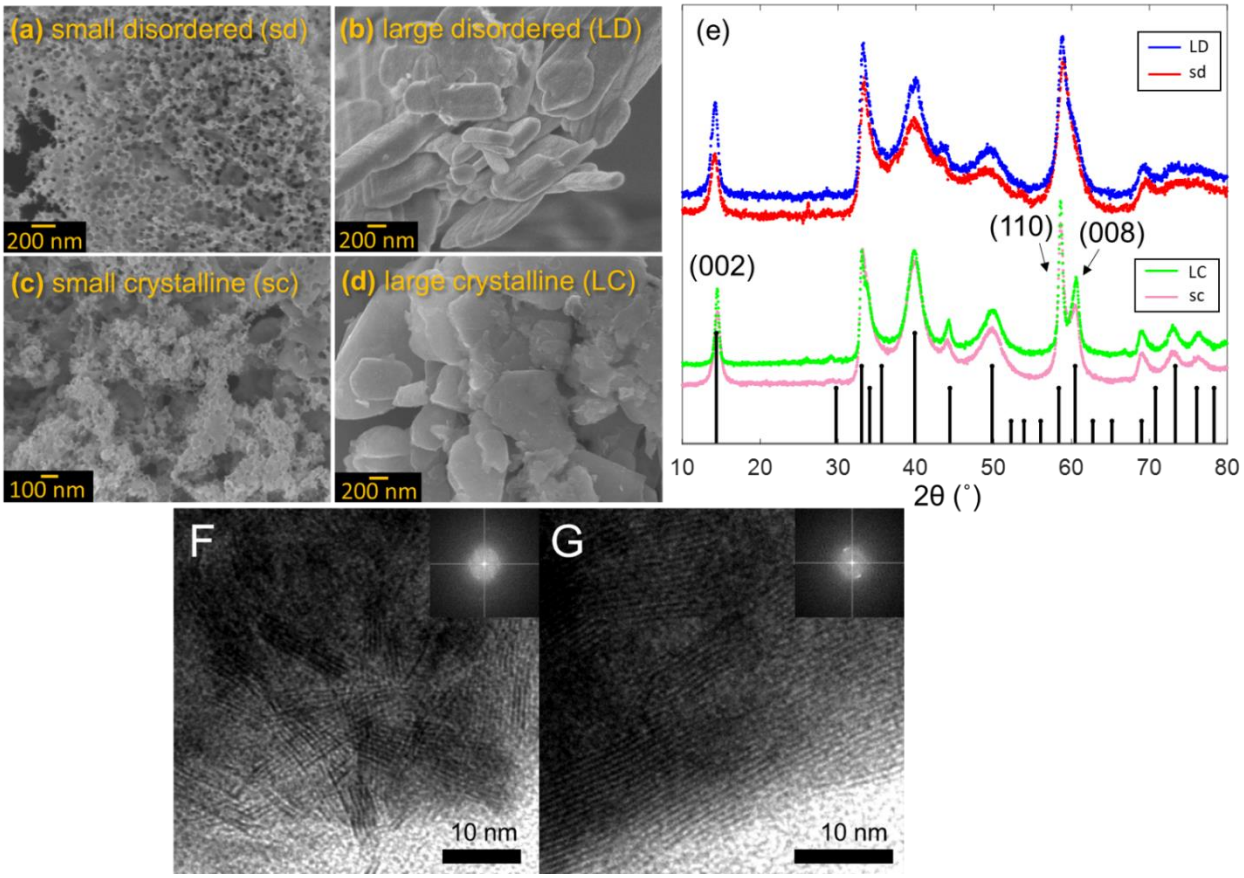

Figure 3.3. SEM images of a) small disordered (sd) MoS_2, b) large disordered (LD) MoS_2, c) small crystalline (sc) MoS_2, and d) large crystalline (LC) MoS_2. Panel e) shows that the XRD patterns for sd-MoS_2 (red) and LD-MoS_2 (blue) display significant peak broadening and disorder while sc-MoS_2 (pink) and LC-MoS_2 (green) show more well-resolved diffraction peaks, especially at 60˚ and 70-80˚. Black reference pattern is JCPDS 2-0132 for MoS_2. (F) High resolution transmission electron micrographs (HR-TEM) of LD-MoS_2 showing a disordered region with small grains oriented in different directions. (G**)** HR-TEM showing a more ordered region of LD-MoS_2 with several coherent crystal domains extending across tens of nanometers. Insets show Fourier transforms of the micrographs.

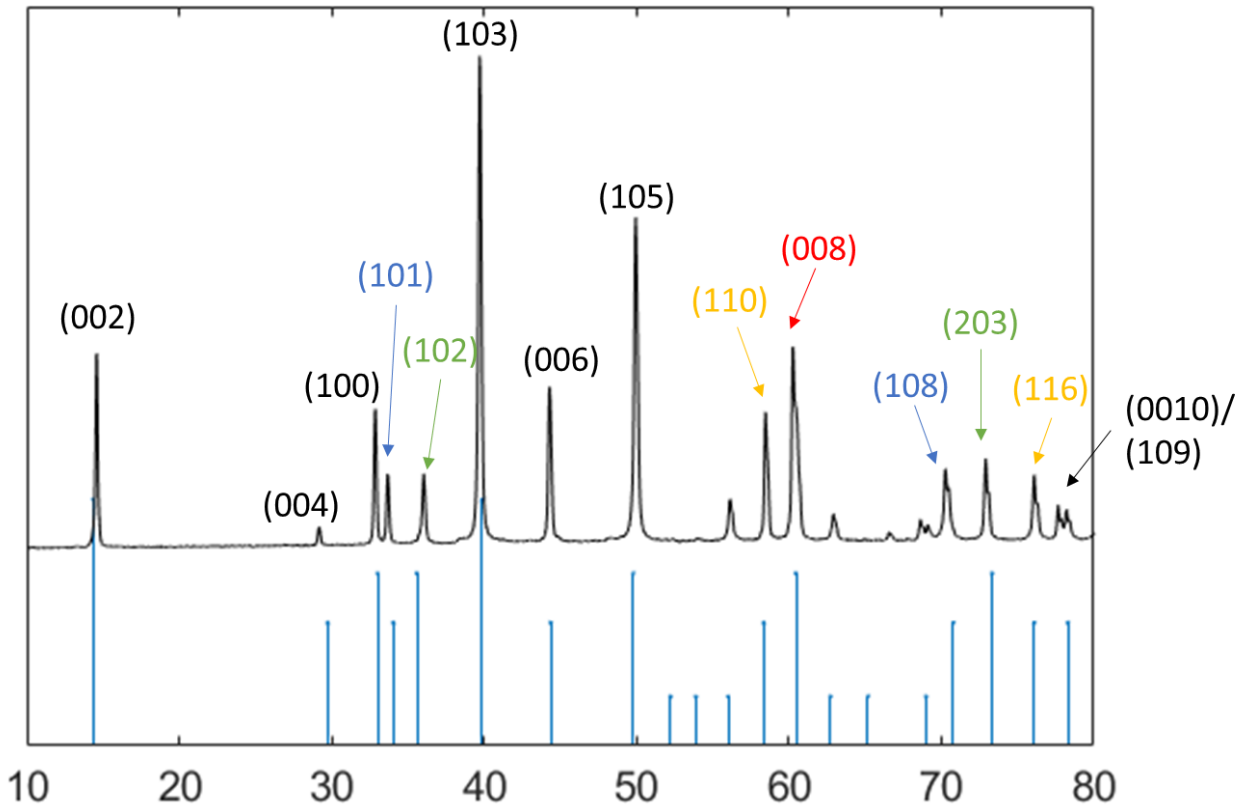

Figure 3.4. XRD for bulk MoS_2 powder with MoS_2 reference pattern JCPDS 2-0132 and corresponding lattice planes.

By increasing the sulfurization temperature from 700˚C (small disordered) to 900˚C (small crystalline), the diffraction peaks sharpen while the physical crystal size according to SEM looks nearly the same. In the region near 60˚, the two peaks corresponding to (110) and (008) planes are broadened into one peak in the disordered (Fig 3.3e, top) samples, while in the crystalline samples (Fig 3.3e, bottom), the peaks are well resolved. Similarly, in the 70 – 80˚ region, there are three peaks distinguishable in the crystalline samples, but they are broadened into one feature in the disordered samples. Because the physical particle size looks nearly the same between sd/sc and LD/LC, we attribute the diffraction peak sharpening to increasing order in the lattice as the

annealing temperature is increased, rather than grain growth. Because “disorder” is a property which is often ambiguously defined, we use this diffraction sharpening criterion to distinguish between “disordered” and “crystalline” samples, although all samples contain some degree of lattice disorder in comparison to bulk material. Therefore, we have demonstrated that we can synthetically control the degree of lattice disorder by simply increasing the annealing the temperature, and we can independently control particle size by increasing the size of the MoO_2 or MoO_3 precursor.

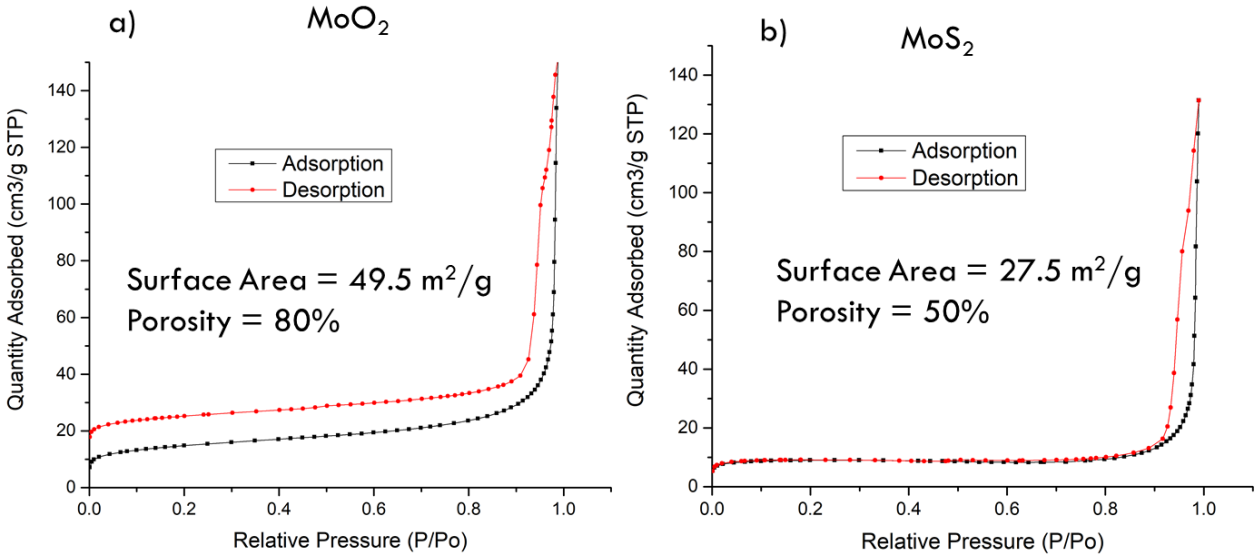

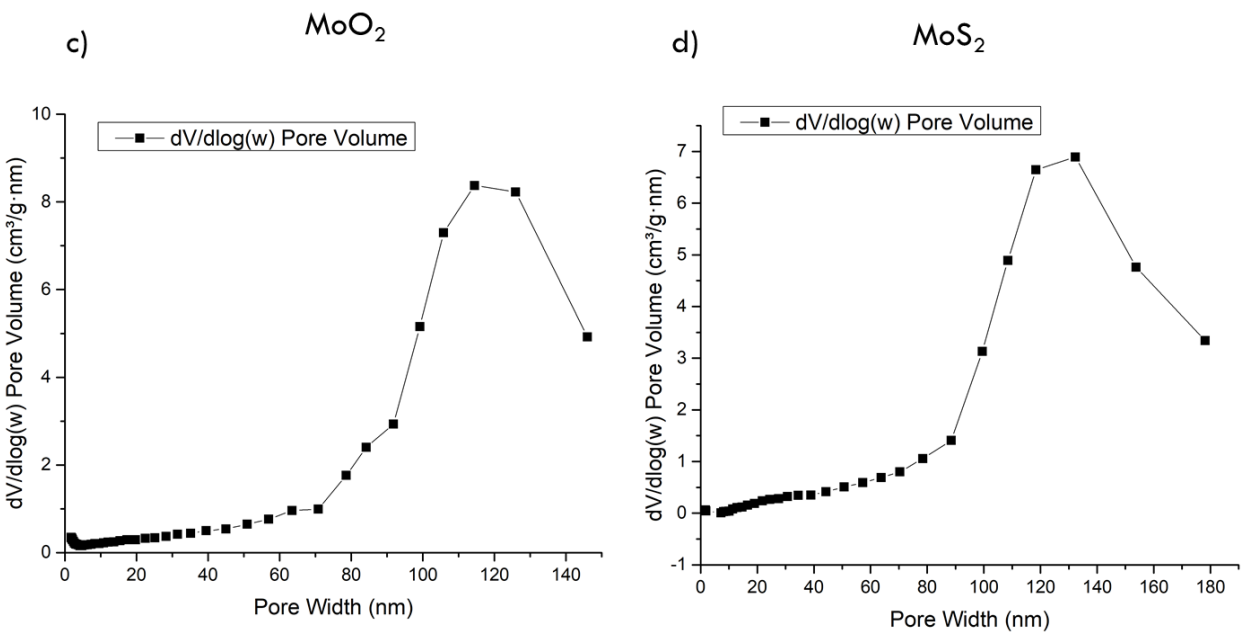

Figure 3.5. Nitrogen adsorption porosimetry isotherm for a) precursor mesoporous MoO_2 and b) product mesoporous MoS_2. Pore size distribution dV/dlog(w) for c) MoO_2 and d) MoS_2.

Nitrogen adsorption porosimetry shows that both the precursor MoO_2 and product MoS_2 have high surface area and mesoporosity, exhibited by the hysteresis in the adsorption and desorption branches of the isotherms (**Figure 3.5**). Surface area and porosity are decreased in MoS_2 because of the larger sulfur atom leads to expansion of the material into pores. If we look at the dV/dlog(w) pore size distribution (Figure 3.5c,d), the pore structure is well retained in MoS_2 but the peak of pore size is slightly larger than MoO_2. This seems to be inconsistent with material expansion into pores, which would lead to smaller pores. However, we reconcile these facts by speculating that the material expansion due to replacing oxygen with sulfur leads to filling up some of the smaller pores, effectively removing them from the distribution. Surface area of the MoS_2

was measured to be 27.5 m^2 g^{-1} (Figure 3.5a, b) and the porosity was calculated to be 50%, demonstrating a highly mesoporous network for conductivity and electrolyte penetration.

To elucidate the nature of disorder present in our mesoporous MoS_2, we collected total x-ray scattering at APS BL 11-ID-B. The total scattering technique collects both Bragg and diffuse scattering from the sample.[48-50] By taking the Fourier transform of the total scattering, the atomic pair distribution function (PDF) is calculated, which gives all atom-atom correlations within the material, regardless of long-range order. Therefore, the PDF enables us to characterize structural information (atom-atom distances) about amorphous or disordered regions in the material and give insight to short-range order.

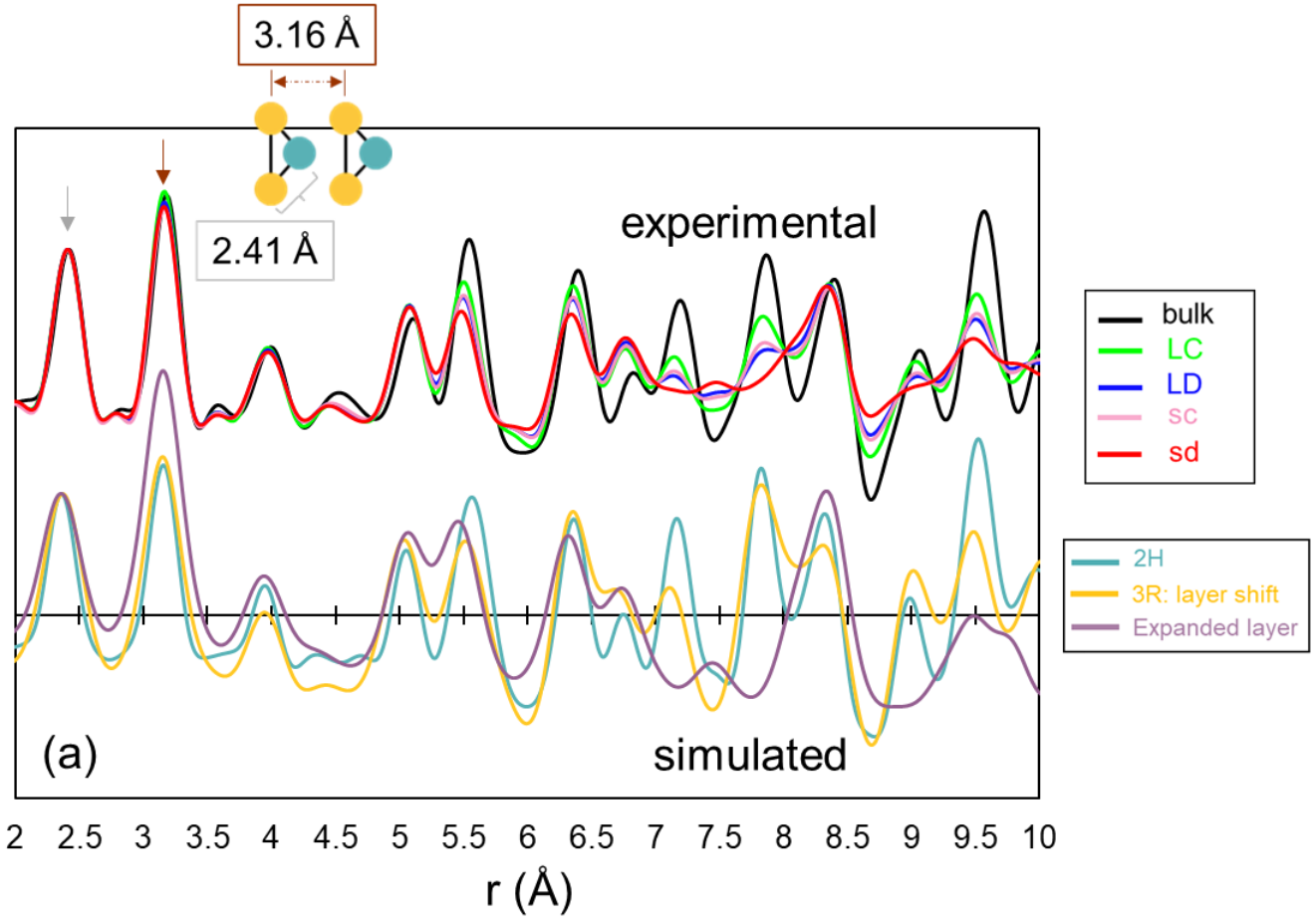

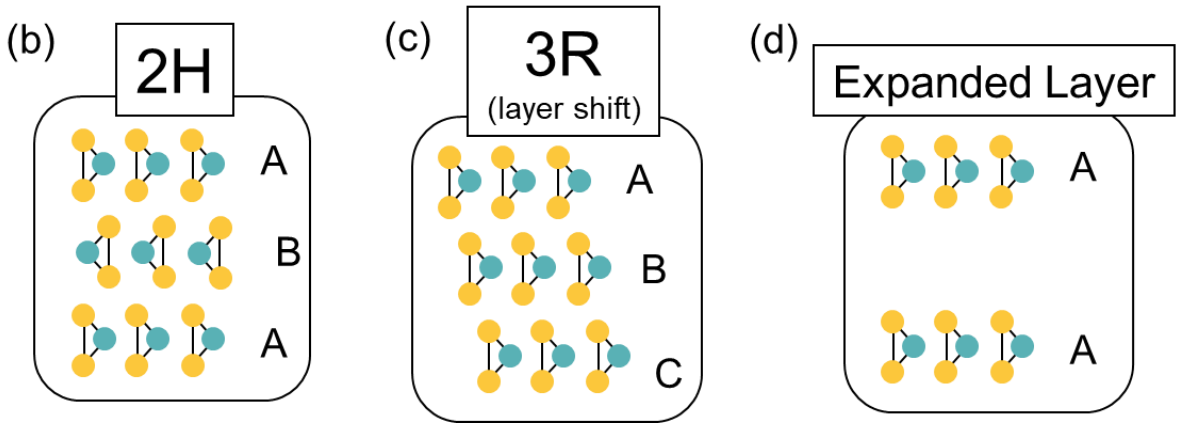

Figure 3.6. Crystal structure models used to simulate PDF. (a) Experimental PDF for bulk, large crystalline, large disordered, small crystalline, and small disordered MoS_2 overlaid with simulated PDF patterns. (b) standard 2H MoS_2 with A-B-A layer stacking. (c) 3R MoS_2 polymorph with A-B-C layer stacking, used to simulate the effect of stacking faults and layer shifting. (d) Expanded layer model derived from the 2H structure with an expanded vdW gap.

The first two peaks in the PDF at 2.41 Å and 3.16 Å (**Figure 3.6a**) correspond to the nearest Mo-S bond within one trigonal prism and the Mo-Mo/S-S correlations within one layer in the neighbouring unit cell (Figure 3.6a), respectively. Peaks below 5 Å can be assigned to distinguishable bond distances within the MoS_2 unit cell by observation, but above 5 Å, the PDF peaks are no longer unique bonds, as they contain contributions from multiple atom-atom distances within a periodic system. However, the presence of higher-r peaks indicate the extent of long-range order. By simulating the PDF from crystal structures of MoS_2, higher-r peaks can also be decomposed into contributions from Mo-Mo, Mo-S, or S-S correlations (**Figure 3.7**). We can see the sulfur contribution to the total PDF is significantly less than that of molybdenum, since x-ray scattering power is proportional to atomic number. Therefore, we might expect that sulfur atom

positions in the sample that deviate from the crystal structure would result in a modulation of PDF peak intensity rather than appearance of new PDF peaks. The bulk MoS_2 shows high amplitude correlations going out to 7 nm and higher (**Figure 3.8**), as expected for a fully crystalline material. For all mesoporous samples, the PDF up to 5 Å is nearly identical, indicating that all have the same local ordering within one unit cell. However, differences begin to appear in the 5.5 – 8 Å region. The peaks at 7.2 Å and 7.88 Å show a systematic decline in intensity as both size and order decrease.

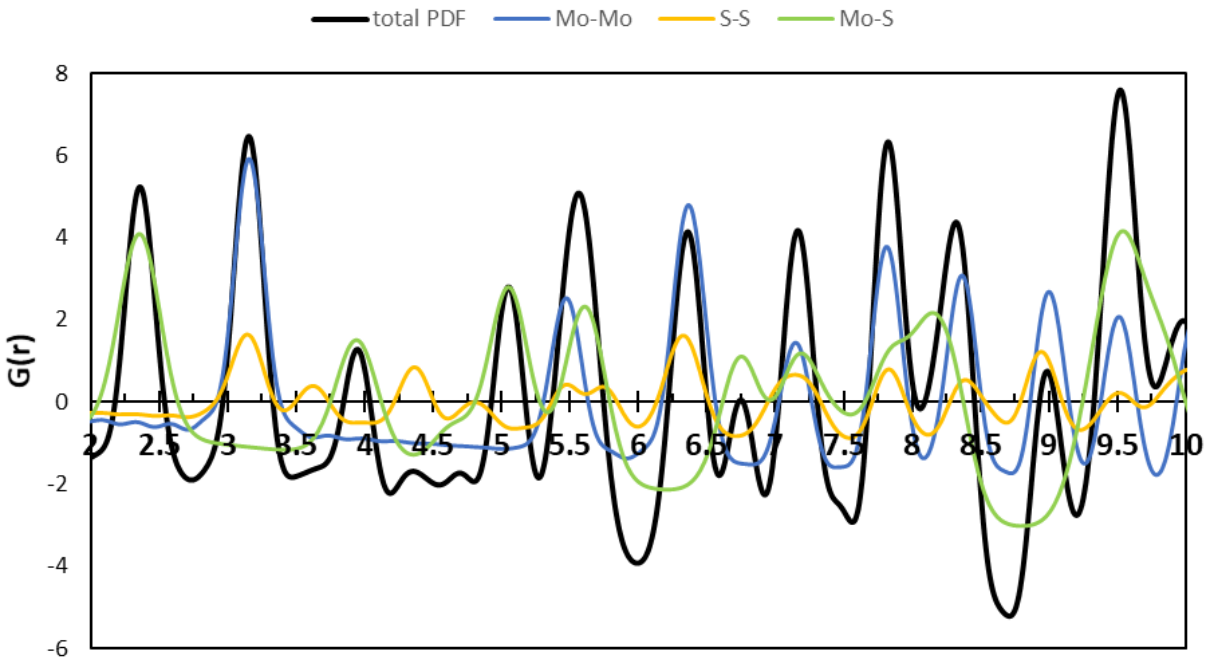

Figure 3.7. Simulated PDF of 2H MoS_2 (Schonfeld structure) decomposed into contributions from Mo-Mo, S-S, and Mo-S correlations.

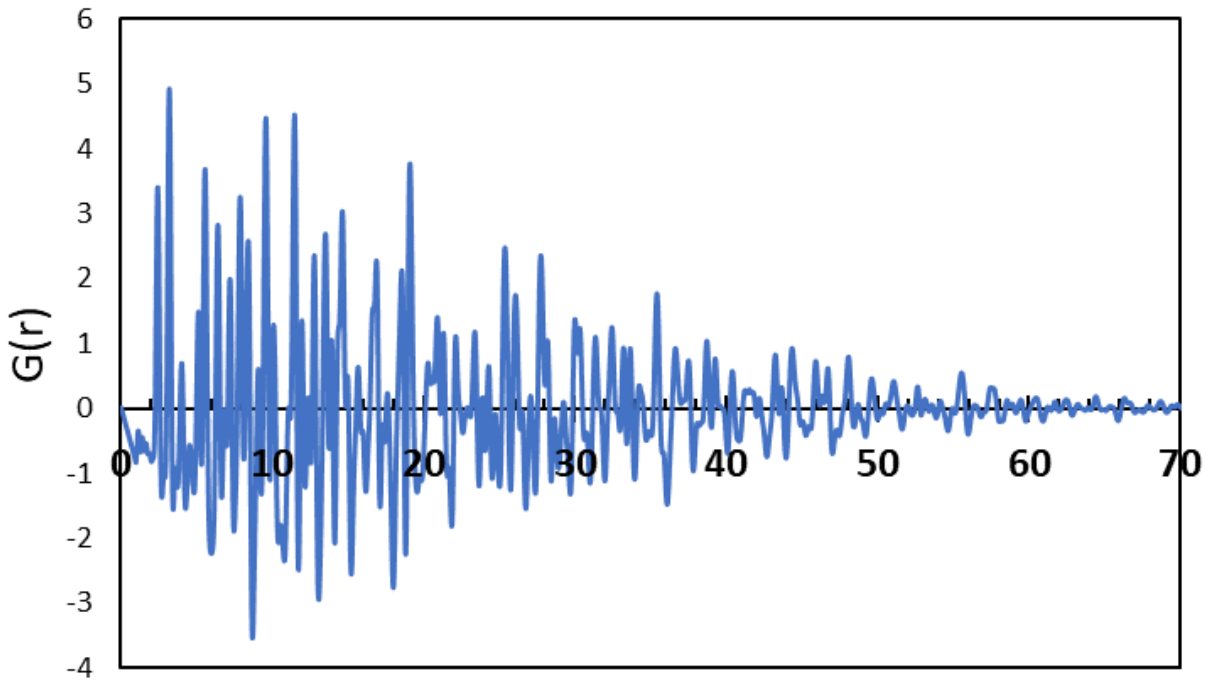

Figure 3.8. Experimental PDF of commercial bulk MoS_2. Although it may appear that long range correlations are significantly lost after 6 nm or so, this dampening out is due to the instrument function.

To determine what types of lattice disorder affect specific correlations, reference PDF patterns were simulated for the standard 2H MoS_2 crystal structure (Fig 3.6b), the 3R polymorph (Fig 3.6c), and a model with only vdW layer expansion (Fig 3.6d). 3R-MoS_2 is another naturally occurring polymorph, though less common than 2H, that has a rhombohedral unit cell with Mo atoms in a trigonal prismatic coordination environment.[44,51-52] The unit cell of 2H-MoS_2 contains two S-Mo-S layers oriented anti-parallel to each other (illustrated by the direction of the S-Mo-S triangle cartoon in Fig 3.6b-d) in an A-B-A-B stacking pattern. 3R-MoS_2 has three distinct S-Mo-S layers oriented parallel to one another, with the third layer is offset so that 3R has an A-B-C stacking pattern. Therefore, the 3R-MoS_2 crystal structure is used to simulate the effect of layer

shifting disorder or stacking faults in PDF. The expanded layer model (Fig 3.6d) is derived from the 2H structure and used to simulate the effect of layer expansion disorder in the PDF. From the simulated patterns, it is evident that both layer shifting and layer expansion cause a decline in intensity at 7.2 Å, while the decline in intensity at 7.88 Å is primarily due to layer expansion. Therefore, we have demonstrated that both layer shifting and layer expansion disorder exist in mesoporous MoS_2 and contribute to faster Li^+ ion diffusion.

To quantify the extent of layer shifting compared to layer expansion disorder occurring in each sample, a multi-phase refinement using 2H, 3R, and expanded layer crystal structures was performed (Table 1). For reference, a multi-phase fit was also performed on the bulk MoS_2 PDF, which shows 97% of the material corresponds well to the standard 2H phase. It is interesting to note that even the large crystalline (LC) sample has significant layer shifting compared to bulk MoS_2. By comparing the LC/sc samples, we can see that order in the crystal lattice manifests as a 52 – 57% fit with the 2H phase, while both contain 36% fit with layer shifted structure. By reducing the size from LC to sc, the extent of layer expansion increases from 7% to 12%. Therefore, the primary effect of reducing the crystal size is to introduce layer expansion disorder. By comparing the LD/sd samples, the amount of layer shifting increases from 57% to 66%, and the amount of layer expansion increases from 16% to 19%. In both LD/sd, it is evident that the disorder largely takes the form of layer shifting or stacking faults introduced by the low annealing temperature. As the annealing temperature is raised, the layers rotate to assemble into a structure that increasingly resembles the periodic 2H crystal lattice.

Table 3.1: Normalized Scale Factor Refinements for 2H, 3R, and expanded layer models for mesoporous MoS_2

Sample	**2H**	**3R (layer shift)**	**Layer expansion**	**R_w**
bulk	0.97	0.00	0.03	0.44
Large crystalline (LC)	0.57	0.36	0.07	0.40
Large disordered (LD)	0.27	0.57	0.16	0.39
Small crystalline (sc)	0.52	0.36	0.12	0.45
Small disordered (sd)	0.15	0.66	0.19	0.38

3.3.2 Electrochemical Characterization

The MoS_2 samples were assembled into composite slurry electrodes for electrochemical testing. Galvanostatic charge and discharge was performed at multiple C-rates on all samples (**Figure 3.9a**) to characterize the rate capability. Both the small samples (sd/sc) show the best rate performance at 100C (36 second charge) achieving 80 mAh g^{-1}, while the bulk MoS_2 has little to no capacity by 60C. It can be noted that several samples (sd, LC, sc) achieve higher than theoretical capacity for 1-electron intercalation (167 mAh g^{-1}) at 1C. To show a clearer representation of the percentage capacity retained at higher C-rates, we have normalized the rate capability to the experimental 1C capacity (Figure 3.9b). From the normalized rate capability, we can see that the small disordered MoS_2 shows the best performance in terms of greater fraction of 1C capacity retained at all current densities, except at 100C where it is equal to the small crystalline MoS_2 (39% of 1C capacity retained at 100C). Therefore, both reducing the crystal size and introducing lattice disorder can shorten the ion diffusion length and improve fast-charging performance.

Comparing normalized capacity across all mesoporous samples at 80C, the large crystalline MoS_2 (green) shows the slowest rate performance (28% of 1C capacity), while the large disordered MoS_2 (blue) retains 37%. Therefore, simply introducing disorder into the lattice of large particles can speed up Li^+ intercalation significantly. We hypothesize this is because the key interactions with the intercalating ion that govern diffusion rate are only within a few nanometers distance. For example, the limited crystal coherence length can prevent ordering of Li^+ and other transitions associated with slower Li^+ diffusion. Thus, disorder may lead to improvement of rate capability even when the physical particle size, and therefore the solid-state diffusion length for Li^+, remain large. Decreasing the material size can also shorten the diffusion length and speed up Li intercalation, demonstrated by the small crystalline MoS_2 (pink) retains 42% at 80C. Size appears to be a more significant effect for rate cycling, but both size and disorder can be leveraged to enhance the rate capability synergistically. Small disordered MoS_2 (red) shows the highest capacity, with 45% retained at 80C.

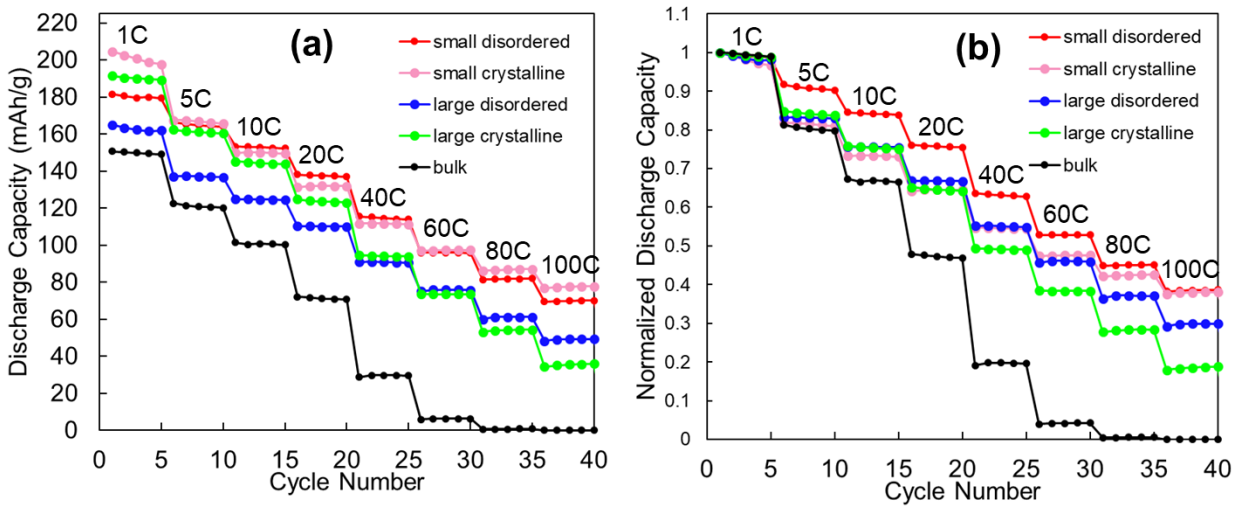

Figure 3.9. a) Rate capability of bulk and mesoporous MoS_2 in terms of absolute discharge capacities. b) Discharge capacities normalized to the 1C capacity to show percentage drop from 1C capacity.

To deconvolute the fraction of charge storage coming from near-surface or "capacitive" processes versus diffusion-limited or "bulk battery-like" processes, we employ several kinetic analyses. The first, termed the "b-value analysis", is a simplification of the Randles-Sevcik equation and assumes that the current measured in a CV experiment follows the power law of Equation (3.3), where ν is the scan rate and 'a' and 'b' are fitted parameters.[53] By taking CVs at multiple scan rates and taking the current value at peak positions (voltages where redox events are happening), we can fit a line through of a plot of log(i) vs. log(ν) to obtain 'b' as the slope (Equation (3.4)).

$$i = a\nu^b \tag{3.3}$$

$$\log(i) = \log(a) + b * \log(\nu) \tag{3.4}$$

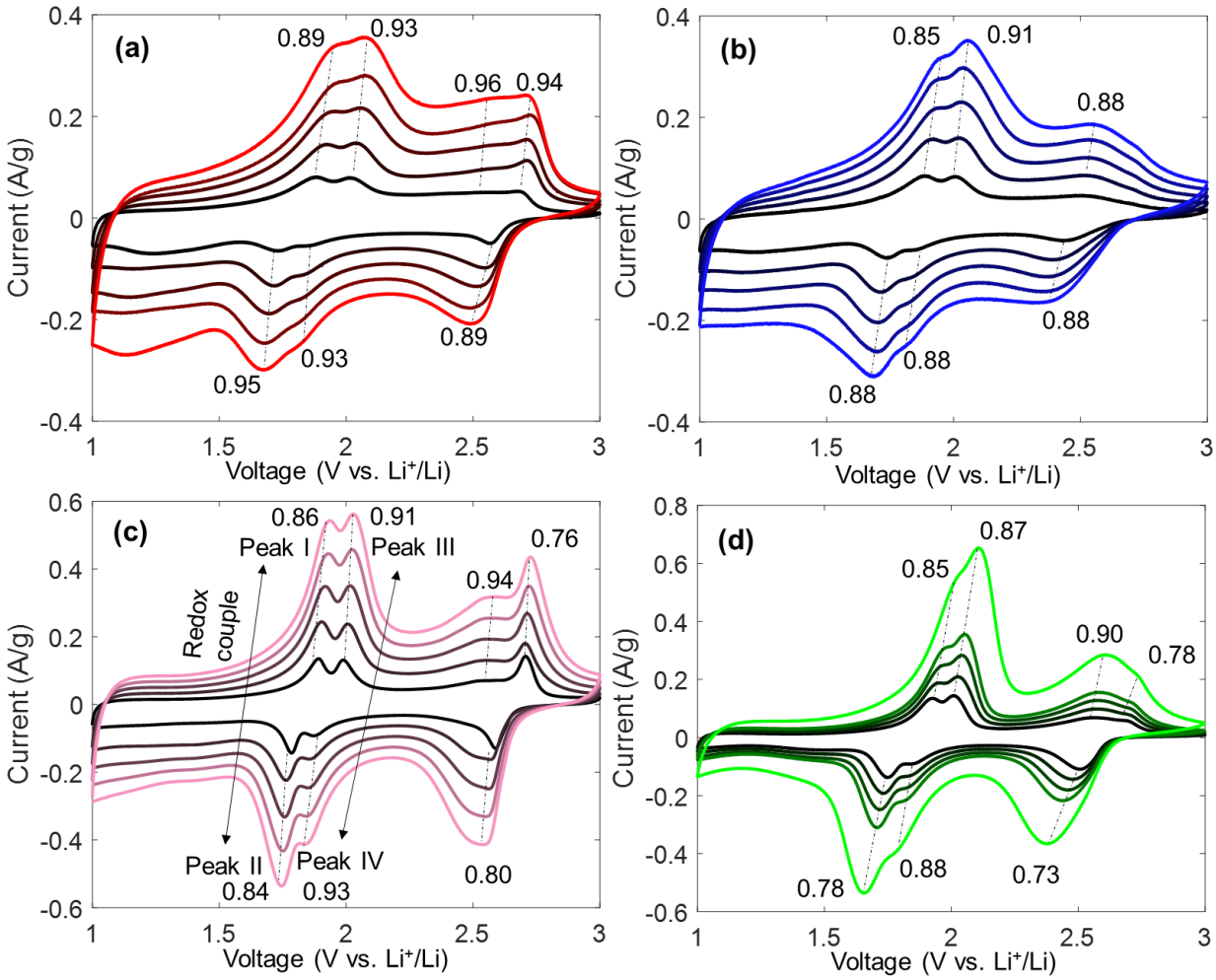

Figure 3.10. CVs with peak b values of (a) small disordered, (b), large disordered, (c) small crystalline, and (d) large crystalline mesoporous MoS_2 samples.

Values of b ~ 0.5 indicate current limited by semi-infinite diffusion or "bulk battery-like" behavior. In contrast, when b ~ 1.0, the current varies linearly with the scan rate and is no longer limited by diffusion, indicating "capacitor-like" behavior. Even in the large crystalline sample (**Figure 3.10d**), the b-values are relatively high, but it is evident that by decreasing crystal size (Figure 3.10c), or by introducing lattice disorder (Figure 3.10b), the capacitive contribution to

charge storage can be increased. Both size and disorder effects can be leveraged to further improve pseudocapacitive charge storage and enhance fast-charging performance.

It is also interesting to note that by comparing both the sc/sd and LC/LD pairs, the shape of the CV is also significantly altered. In both crystalline samples (Figure 3.10c,d), the redox peaks near 1.8 V and 2.6 V are more well-defined than in their disordered counterparts (Figure 3.10a,b). The CV suggests that introducing disorder into the lattice creates a broader distribution of redox potentials, as the Li sites in a more disordered lattice will not be energetically equivalent. As disorder increases, the relative height of the current peak at 2.6 V compared to the 1.8 V peak appears to diminish, but the total charge stored in the same voltage window is the same or higher. This suggests that, in the disordered MoS_2, the same amount of total charge is stored, but the thermodynamic potential of some redox sites has been lowered.

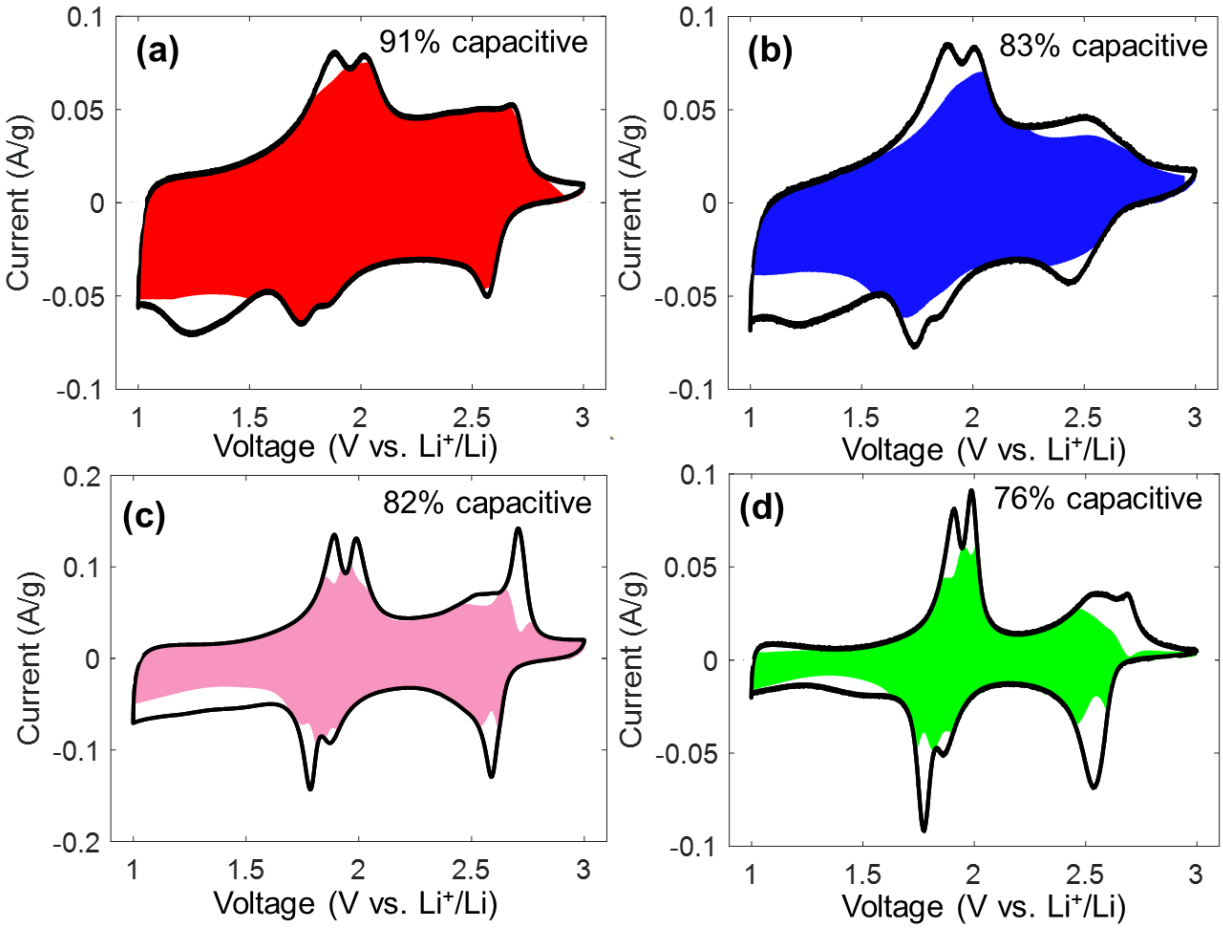

Figure 3.11. k_1 k_2 analysis of (a) small disordered, (b), large disordered, (c) small crystalline, and (d) large crystalline mesoporous MoS_2 samples, CVs taken at 0.1 mV/s.

Another kinetic analysis method is the "k_1 k_2 analysis", first introduced by Conway and coworkers to characterize capacitive charge storage in molybdenum nitride, which assumes that the current behavior depends on the sweep rate according to Equation (3.5):[54]

$$i = k_1 v + k_2 v^{\frac{1}{2}} \tag{3.5}$$

Equation (3.5) is another way of separating out the fraction of current originating from capacitive processes compared to diffusion-limited processes. After shifting the CV peak voltages at higher

scan rates to account for polarization, a plot of $iv^{-1/2}$ vs $v^{1/2}$ can be fit to a line to obtain k_1 as the slope and k_2 as the intercept (Equation (3.6)). By multiplying the k_1 value at each voltage point by $v^{1/2}$, we can obtain an estimated CV corresponding to only the capacitive contribution to charge storage, shown by the colored shaded region of each CV in **Figure 3.11**. This analysis has been performed on the CV taken at the slowest sweep rate, 0.1 mV/s because we are approaching the maximum charge storage at slow rates. By integrating the total current obtained from the "capacitive CV" and dividing it by the integrated total current from the entire CV, the percentage of capacitive charge storage is calculated. At voltages where the redox peaks occur, there is less capacitive contribution to the charge storage due to diffusion limitations.

$$iv^{\frac{-1}{2}} = k_1 v^{\frac{1}{2}} + k_2 \quad (3.6)$$

We observe again that the large crystalline sample shows the lowest capacitive fraction at 76% (Figure 3.11d), while the small crystalline and large disordered show a similar increase in capacitive fraction to 82% and 83% (Figures 3.11b,c).

To estimate an effective Li diffusion coefficient as a function of state of charge, we performed GITT experiments, where the voltage change is monitored during multiple constant current pulses and subsequent rest periods.[55-56] GITT theory is based on Fick's law of one-dimensional diffusion and expresses the solid-state Li diffusion coefficient D as a function of the steady-state voltage change after current pulse, corrected by voltage change during current pulse, given by Equation (3.7)[57]

$$D = \left(\frac{4}{\pi\tau}\right)\left(\frac{n_m V_m}{S}\right)^2\left(\frac{\Delta E_s}{\Delta E_t}\right)^2 \quad (3.7)$$

where τ is the duration of current pulse (s), n_m is the number of moles of active material, V_m is the molar volume, S is the active material surface area, ΔE_s is the steady-state voltage change, and ΔE_t

is the voltage change during current pulse. **Figure 3.12a** shows the voltage versus time graph for all size and disorder samples of MoS_2 during a GITT pulse-rest protocol. To calculate a value for D, the electroactive surface area (S) is needed, but in practice, this is difficult to measure accurately for a mesoporous material in a slurry electrode. Therefore, we plot the squared corrected voltage change $(\frac{\Delta E_s}{\Delta E_t})^2$, which is directly proportional to the diffusion coefficient, as a function of state of charge (Figure 3.12b).[58] This value has been normalized to compare relative drops in diffusion coefficient. The Li diffusion coefficient is largest at the onset of Li intercalation, consistent with the fact that the Li gradient is largest in the beginning. As Li content increases, the Li diffusion coefficient drops in all samples due to more cation-cation interactions that increase the energy barrier to hopping between lattice sites.

A known shortcoming in traditional GITT theory is the underestimation of Li diffusion coefficient in voltage ranges where a first-order phase transformation occurs between Li-rich and Li-poor phases.[59] Mathematically, this can be seen as ΔE_s becomes very small during a voltage plateau corresponding to a phase transformation. Physically, this is because Li ions are transported not only by solid state diffusion, but also through the movement of the phase boundary. Therefore, the diffusion coefficient calculated during the two-phase coexistence region is artificially low. A more complex GITT theory for phase transformation electrodes has been developed by Zhu et al. to provide more accurate diffusion coefficients during a phase transition. However, since we are looking at trends in $(\frac{\Delta E_s}{\Delta E_t})^2$ rather than trying to estimate absolute values for D, we simply note this limitation and utilize it to confirm that an intercalation-induced phase transformation is occurring in the bulk and large crystalline porous MoS_2. This artificial drop in diffusion coefficient is observed in the bulk MoS_2 (Figure 3.12b, black) and large crystalline MoS_2 (Figure 3.12b, green)

near x = 0.4 – 0.5. In contrast, the small disordered, small crystalline, and large disordered samples all show a gradual decrease in Li diffusion coefficient with no abrupt drops, consistent with the observation in *operando* XRD (discussed below) that these 3 samples do not undergo a first-order phase transition during Li (de)-intercalation.

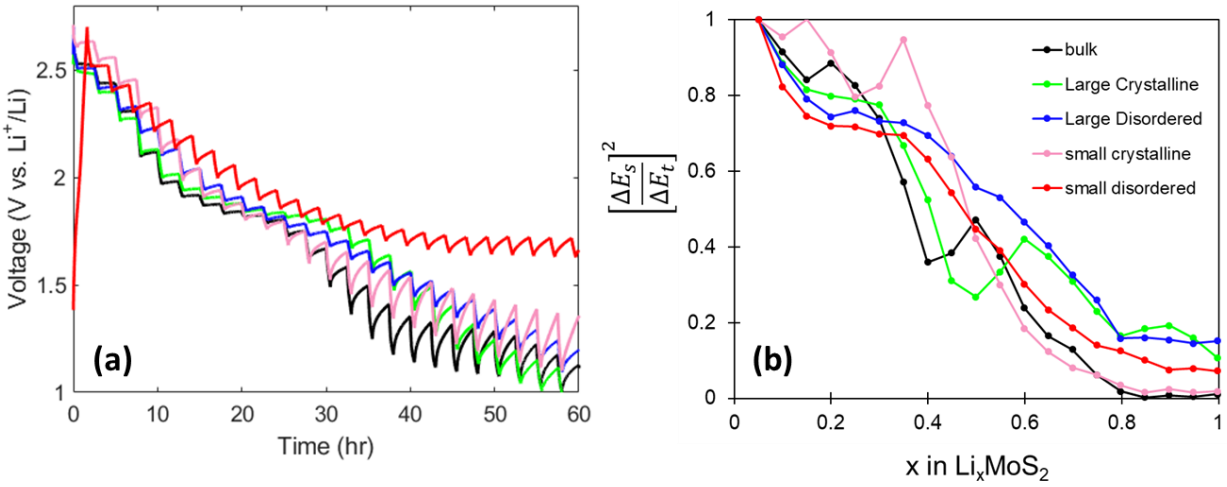

Figure 3.12. GITT of all samples, showing a) voltage vs time during pulse-rest cycles and b) calculated diffusion coefficient vs state of charge.

3.3.3 *Operando* XRD

To monitor the change in crystal structure during electrochemical cycling, *operando* X-ray diffraction was conducted on the samples. For clarity, only the time evolution of the (002) peak is plotted since the (002) peak corresponds to the vdW gap and the Li^+ diffusion pathway. Again, we observe that the small disordered (**Figure 3.13a**) and large disordered (Figure 3.13b) samples show significant diffraction peak broadening due to the lattice disorder, while the small crystalline (Figure 3.13c) and large crystalline (Figure 3.13d) show sharper (002) diffraction peaks. Only the large crystalline MoS_2 (Figure 3.13d) shows a distinct phase transition upon Li^+ intercalation, evidenced by the appearance of a new peak at Q ~ 1.05 $Å^{-1}$ corresponding to the triclinic Li_xMoS_2

phase.[60] In contrast, all other samples (sd, sc, LD) show only a slight shift in the lattice spacing during both lithiation and de-lithiation. Therefore, our results confirm that both size and disorder effects can cause the suppression of intercalation-induced phase transitions. By fitting the peak positions to Voigt functions, we have calculated the d-spacing throughout the *operando* experiment and observe that the (002) plane undergoes an initial expansion then contraction during both lithiation and de-lithiation (Figure 3.13e,f). The lattice "breathing" behavior is the result of a tradeoff between attractive interactions of Li^+ and S^{2-} causing lattice contraction, and repulsive interactions between nearby Li-Li pairs and volume change to accommodate ions causing lattice expansion. During lithiation, the lattice spacing of sd/LD samples shows a gradual, linear expansion from 1.0 – 1.8 V, while the sc/LC samples show a more abrupt lattice expansion. Paired with the observation that the CVs of sd/LD samples are more similarly broadened (Figure 3.10a,b), while the CVs of sc/LC samples show more distinct redox peaks (Figure 3.10c,d), we suggest that size and disorder effects cause suppress phase transitions and enhance rate capability through different mechanisms.

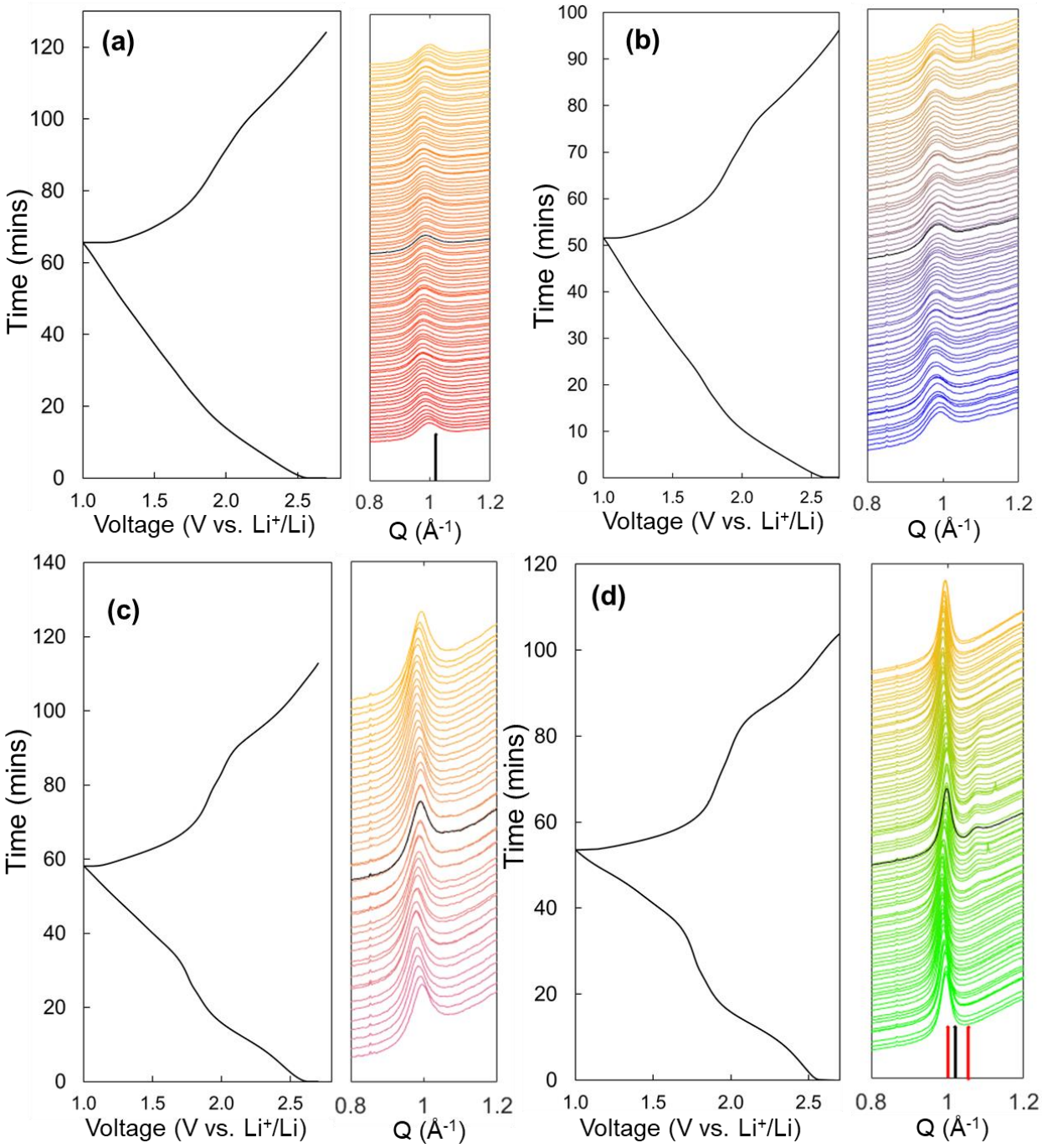
(a)
(b)
(c)
(d)
Time (mins)
Voltage (V vs. Li+/Li)
Q (Å-1)

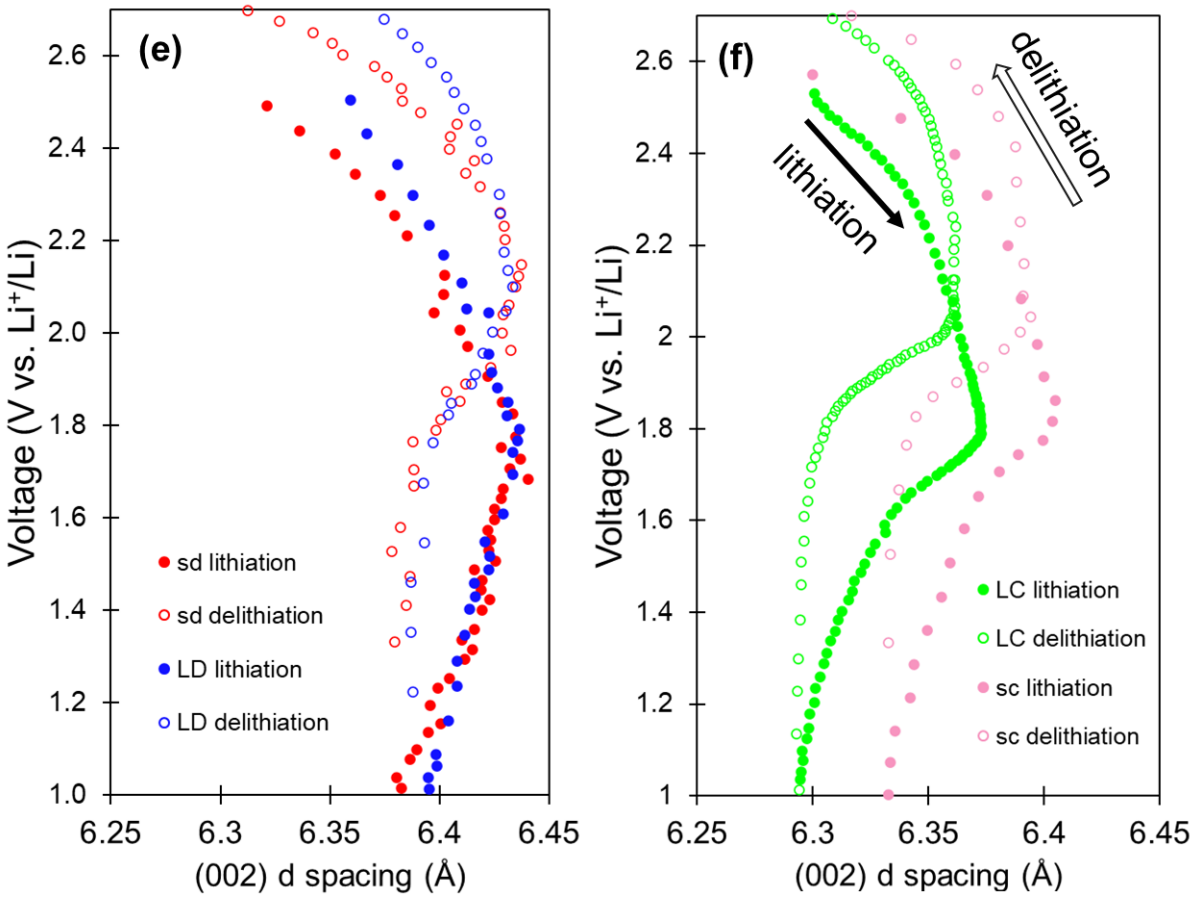

Figure 3.13. Operando XRD of (a) small disordered, (b) large disordered, (c) small crystalline, and (d) large crystalline MoS_2 samples cycled at 1C in pouch cells. Left panels shows the corresponding GV trace. (002) lattice spacing calculated from fitted peak positions for (e) small and large disordered samples, and (f) small and large crystalline samples. Black sticks in (a) and (d) show the reference pattern for 2H MoS_2. Red stick patterns in (d) show reference pattern for triclinic Li_xMoS_2.

It is also interesting to note that, although there is some variation in the (002) d-spacing between all size and disorder samples, the lattice spacing in the LC sample (which showed a phase transition) is only moderately smaller, contrary to what might be expected. This suggests that only

a small lattice expansion is needed to suppress Li^+ intercalation-induced phase transitions and that at some critical vdW gap size (6.4 - 6.5 Å), the disorder plays the dominant role in facilitating faster Li^+ diffusion.

3.4 Conclusions.

We have synthesized a matrix of mesoporous MoS_2 through gas-phase sulfurization with different crystal sizes and degrees of crystallinity to decouple the effects of both size and disorder on electrochemical performance and phase transition behavior. Pair distribution function (PDF) measurements and simulations confirm that both layer shifting and layer expansion disorder are present. The primary effect of reducing particle size is to expand the vdW gap size, while the lower annealing temperature used to produce the "disordered" samples results in stacking faults. Rate capability experiments show that both decreasing particle size and increasing disorder are effective ways to promote faster Li^+ diffusion and 40% rate retention up to 100C. CV demonstrates that disorder creates a broader distribution of redox potentials. Both b-value and k_1-k_2 analyses reveal that size and disorder effects increase the fraction of non-diffusion-limited pseudocapacitive charge storage in the material. *Operando* XRD demonstrates that only the large crystalline MoS_2 undergoes a first-order phase transition from 1T-MoS_2 to the triclinic Li_xMoS_2 phase, while small disordered, small crystalline, and large disordered MoS_2 show gradual lattice expansion and contraction of the vdW gap without any appearance of new phases during cycling. Therefore, tuning both size and lattice disorder are effective methods for suppressing intercalation-induced phase transitions and introducing pseudocapacitive charge storage.

3.5 References

[1] Li, Matthew; Feng, Ming; Luo, Dan; Chen, Z. "Fast Charging Li-Ion Batteries for a New Era of Electric Vehicles." *Cell Reports Physical Science*, **2020**, 1, 100212.

[2] Simon, Patrice; Gogotsi, Yuri; Dunn, B. "Where Do Batteries End and Supercapacitors Begin?" *Science*, **2014**, 343, 1210 – 1211.

[3] Fleishmann, Simon; Mitchell, James B.; Wang, Ruocun; Zhan, Cheng; Jiang, De-en; Presser, Volker; Augustyn, V. "Pseudocapacitance: From Fundamental Understanding to High Power Energy Storage Materials." *Chemical Reviews*, **2020**, 120, 6738 – 6782.

[4] Conway, B.E.; Pell, W.G. "Double-layer and pseudocapacitance types of electrochemical capacitors and their applications to the development of hybrid devices." *Journal of Solid State Electrochemistry*, **2003**, 7, 637 – 644.

[5] Conway, B.E. "Two-dimensional and quasi-two-dimensional isotherms for Li intercalation and upd processes at surface." *Electrochimica Acta*, **1993**, 38, 1249 – 1258.

[6] Van der ven, A.; Bhattacharya, J.; Belak, A.A. "Understanding Li Diffusion in Li-Intercalation Compounds." *Accounts of Chemical Research*, **2013**, 46, 1216 – 1225.

[7] Okubo, M.; Hosono, E.; Kim, J.; Enomoto, M.; Kojima, N.; Kudo, T.; Zhou, H.; Honma, I. "Nanosize Effect on High-Rate Li-Ion Intercalation in $LiCoO_2$ Electrode." *Journal of the American Chemical Society*, **2007**, 129, 7444 – 7452.

[8] Kim, H.-S.; Cook, J.B.; Tolbert, S.H.; Dunn, V. "The Development of Pseudocapacitive Properties in Nanosize-MoO_2". *Journal of the Electrochemical Society*, **2015**, 162, A5083 – A5090.

[9] Muller, G.A.; Cook, J.B.; Kim, H.-S.; Tolbert, S.H.; Dunn, B. "High Performance Pseudocapacitor Based on 2D Layered Metal Chalcogenide Nanocrystals". *Nano Letters*, **2015**, 15, 1911-1918.

[10] Cook, J.B.; Kim, H.-S.; Lin, T.C.; Lai, C.-H.; Dunn, B.; Tolbert, S.H. "Pseudocapacitive Charge Storage in Thick Composite MoS_2 Nanocrystal-Based Electrodes". *Advanced Energy Materials*, **2017**, 7, 1601283.

[11] Xu, Y.; Wang, Z.; Yang, Z.; Na, J.; Azhar, A.; Wang, S.; Yu, J.; Yamauchi, Y. "New Insights into the Lithium-Ion Diffusion transport Mechanism in Vanadate Compounds". *ACS Energy Letters*, **2021**, 6, 886-892.

[12] Wu, M.; Xu, B.; Ouyang, C. "Physics of electron and lithium-ion transport in electrode materials for Li-ion batteries". *Chinese Physics B*, **2016**, 25, 018206.

[13] Robert, R.; Bünzli, C.; Berg, E.J.; Novák, P. "Activation Mechanism of $LiNi_{0.80}Co_{0.15}Al_{0.05}O_2$: Surface and Bulk Operando Electrochemical, Differential Electrochemical Mass Spectrometry, and X-ray Diffraction Analyses". *Chemistry of Materials*, **2015**, 27, 526 – 536.

[14] Purwanto, A.; Yudha, C.S.; Ubaidillah, U.; Widiyandari, H.; Ogi, T.; Haerudin, H. "NCA cathode material: synthesis methods and performance enhancement efforts". *Materials Research Express*, **2019**, 5, 122001.

[15] Moshtev, R.V.; Zlatilova, P.; Manev, V.; Sato, A. "The $LiNiO_2$ solid solution as a cathode material for rechargeable lithium batteries". *Journal of Power Sources*, **1995**, 54, 329 – 333.

[16] Biasi, L.; Schiele, A.; Roca-Ayats, M.; Garcia, G.; Brezesinski, T.; Hartmann, P.; Janek, J. "Phase Transformation Behavior and Stability of $LiNiO_2$ Cathode Material for Li-Ion Batteries Obtained from In Situ Gas Analysis an Operando X-Ray Diffraction". *ChemSusChem*, **2019**, 12, 2240 – 2250.

[17] Castro-García, S.; Castro-Coucerio, A.; Señarís-Rodríguez, M.A.; Soulette, F.; Julien, C. "Influence of aluminum doping on the properties of $LiCoO_2$ and $LiNi_{0.5}Co_{0.5}O_2$ oxides". *Solid State Ionics*, **2003**, 156, 15 – 26.

[18] Kim, H.-S.; Cook, J.B.; Lin, H.; Ko, J.S.; Tolbert, S.H.; Ozolins, V.; Dunn, B. "Oxygen vacancies enhance pseudocapacitive charge storage properties of MoO_{3-x}". *Nature Materials*, **2017**, 16, 454 – 460.

[19] Liu, X.; Wang, Y.; Yang, Y.; Lv, W.; Lian, G.; Golberg, D.; Wang, X.; Zhao, X.; Ding, Y. "A MoS_2/Carbon hybrid anode for high-performance Li-ion batteries at low temperature." *Nano Energy*, **2020**, 70, 104550.

[20] Shan, T.-T.; Xin, S.; You, Y.; Cong, H.-P.; Yu, S.-H.; Manthiram, A. "Combining Nitrogen-Doped Graphene Sheets and MoS_2: A Unique Film-Foam-Film Structure for Enhanced Lithium Storage." *Angewandte Chemie – International Edition*, **2016**, 55, 12783-12788.

[21] Liu, Y.; Zhang, L.; Wang, H.; Yu, C.; Yan, X.; Liu, Q.; Xu, B.; Wang, L-M. "Synthesis of severe lattice distorted MoS_2 coupled with hetero-bonds as anode for superior lithium-ion batteries." *Electrochimica Acta*, **2018**, 262, 162-172.

[22] Stephenson, T.; Li, Z.; Olsen, B.; Mitlin, D. "Lithium ion battery applications of molybdenum disulfide (MoS_2) nanocomposites". *Energy & Environmental Science*, **2014**, 7, 209-231.

[23] Huang, X.; Zeng, Z.; Zhang, H. "Metal dichalcogenide nanosheets: preparation, properties and applications." *Chemical Society Reviews*, **2013**, 42, 1934-1946.

[24] Huang, G.; Chen, T.; Chen, W.; Wang, Z.; Chang, K.; Ma, L.; Huang, F.; Chen, D.; Lee, J.Y. "Graphene-Like MoS_2/Graphene Composites: Cationic Surfactant-Assisted Hydrothermal Synthesis and Electrochemical Reversible Storage of Lithium". *Small*, **2013**, 9, 3693-3703.

[25] Zhang, X.; An, C.; Wang, S.; Wang, Z.; Xia, D. "Green synthesis of metal sulfide nanocrystals through a general composite-surfactants-aided-solvothermal process". *Journal of Crystal Growth*, **2009**, 311, 3775-3780.

[26] Liu, H.; Su, D.; Zhou, R.; Sun, B.; Wang, G.; Qiao, S.Z. "Highly Ordered Mesoporous MoS_2 with Expanded Spacing of the (002) Crystal Plane for Ultrafast Lithium Ion Storage". *Advanced Energy Materials*, **2012**, 2, 970-975.

[27] Zhang, C.; Wu, H.B.; Guo, Z.; Lou, X.W. "Facile synthesis of carbon-coated MoS_2 nanorods with enhanced lithium storage properties". *Electrochemistry Communications*, **2012**, 20, 7-10.

[28] Hu, X.; Zhang, W.; Liu, X.; Mei, Y.; Huang, Y. "Nanostructured Mo-based electrode materials for electrochemical energy storage". *Chemical Society Reviews*, **2015**, 44, 2376-2404.

[29] Cook, J.B.; Kim, H.-S.; Yan, Y.; Ko, J.S.; Robbennolt, S.; Dunn, B.; Tolbert, S.H. "Mesoporous MoS_2 as a Transition Metal Dichalcogenide Exhibiting Pseudocapacitive Li and Na-Ion Charge Storage". *Advanced Energy Materials*, **2016**, 6, 1-12.

[30] Wu, J.; Dai, J.; Shao, Y.; Cao, M.; Wu, X. "Carbon dot-assisted hydrothermal synthesis of flower-like MoS_2 nanospheres constructed by few-layered multiphase MoS_2 nanosheets for supercapacitors". *RSC Advances*, **2016**, 6, 77999-78007.

[31] Fang, L.; Qiu, Y.; Li, W.; Wang, F.; Lan, M.; Huang, K.; Jing, Q. "Three-dimensional flower-like MoS_2-$CoSe_2$ heterostructure for high performance supercapacitors". *Journal of Colloid and Interface Science*, **2018**, 512, 282-290.

[32] Fang, X.; Hua, C.; Guo, X.; Hu, Y.; Wang, Z.; Gao, X.; Wu, F.; Wang, J.; Chen, L. "Lithium storage in commercial MoS_2 in different potential ranges". *Electrochimica Acta*, **2012**, 81, 155-160.

[33] Jin, Q.; Liu, N.; Chen, B.; Mei, D. "Mechanisms of Semiconducting 2H to Metallic 1T Phase Transition in Two-dimensional MoS_2 Nanosheets". *Journal of Physical Chemistry C*, **2018**, 122, 28215-28224.

[34] Gan, X.; Lee, L.Y.S.; Wong, K.-Y.; Lo, T.W.; Ho, K.H.; Lei, D.Y.; Zhao, H. "2H/1T Phase Transition of Multilayer MoS_2 by Electrochemical Incorporation of S Vacancies". *ACS Applied Energy Materials*, **2018**, 1, 4754-4765.

[35] Wypych, F.; Schöllhorn, R. "1T-MoS_2, a New Metallic Modification of Molybdenum Disulfide". *Journal of the Chemical Society, Chemical Communications*, **1992**, 1386-1388.

[36] Goloveshkin, A.S.; Bushmarinov, I.S.; Korlyukov, A.A.; Buzin, M.I.; Zaikovskii, V.I.; Lenenko, N.D.; Golub, A.S. "Stabilization of 1T-MoS_2 Sheets by Imidazolium Molecules in Self-Assembling Hetero-layered Nanocrystals". *Langmuir*, **2015**, 31, 8953-8960.

[37] Py, M.A.; Haering, R.R. "Structural destabilization induced by lithium intercalation in MoS_2 and related compounds". *Canadian Journal of Physics*, **1983**, 61, 76-84.

[38] Mattheiss, L.F. "Band Structures of Transition-Metal-Dichalcogenide Layer Compounds". *Physical Review B*, **1973**, 8, 3719-3740.

[39] Wang, T.; Sel, O.; Djerdj, I.; Smarsly, B. "Preparation of a large Mesoporous CeO_2 with crystalline walls using PMMA colloidal crystal templates." *Colloid Polymer Science*, **2006**, 285, 1-9.

[40] Yan, Y.; Chin, M.A.; Robertson, D.D.; Lesel, B.K.; Tolbert, S.H. "Tuning the Porous Structure in PMMA-Templated Mesoporous MoO_2 for Pseudocapacitive Li-Ion Electrodes." *Journal of the Electrochemical Society*, **2022**, 169, 040545.

[41] Nagabhushana, G.P.; Samrat, D.; Chandrappa, G.T. "α-MoO_3 nanoparticles: solution combustion synthesis, photocatalytic and electrochemical properties." *RSC Advances*, **2014**, 4, 56784.

[42] Toby, B.H. and R.B. Von Dreele. "GSAS-II: the genesis of a modern open-source all purpose crystallography software package." *Journal of Applied Crystallography*, **2013**, 46, 544 – 549.

[43] Farrow, C.L.; Juhas, P.; Liu, J.W.; Bryndin, D.; Bozin, E.S.; Block. J.; Proffen, Th.; and S.J.L. Billinge. "PDFfit2 and PDFgui: computer programs for studying nanostructure in crystals." *J. Phys.: Condens. Mat.*, **2007**, 19, 335219.

[44] Schonfeld, B.; Huang, J.J.; Moss, S. C. "Anisotropic mean-square displacements (MSD) in single crystals of 2H- and 3R-MoS_2." *Acta Crystallographica, Section B*, **1983**, 39, 404 – 407.

[45] Petkov, V.; Vogt, T.; Billinge, S.J.L.; Mahanti, S.D.; Larson, P.; Rangan, K.K.; Kanatzidis, M.G. "Structure of nanocrystalline materials using atomic pair distribution function analysis: study of $LiMoS_2$." *Physical Review, Series 3. B – Condensed Matter*, **2002**, 65, 921051 – 921054.

[46] Jain, A.; Ong, S.P.; Hautier, G.; Chen, W.; Richards, W.D.; Dacek, S.; Cholia, S.; Gunter, D.; Skinner, D.; Ceder, G.; Persson, K.A. "Commentary: The Materials Project: A materials genome approach to accelerating materials innovation." *APL Materials*, **2013**, 1, 011002.

[47] Remskar, M.; Mrzel, A.; Virsek, M.; Godec, M.; Krause, M.; Kolitsch, A.; Singh, A.; Seabaugh, A. "The MoS_2 Nanotubes with Defect-Controlled Electric Properties." *Nanoscale Research Letters*, **2011**, 6, 1 – 6.

[48] Wang, X.; Tan, S.; Yang, X.-Q.; Hu, E. "Pair distribution function analysis: Fundamentals and application to battery materials." *Chinese Physics B*, **2020**, 29, 028802.

[49] Keen, D.A. "A comparison of various commonly used correlation functions for describing total scattering." *Journal of Applied Crystallography*, **2001**, 34, 172 – 177.

[50] Chapman, K.W. "Emerging *operando* and x-ray pair distribution function methods for energy materials development." *MRS Bulletin*, **2016**, 41, 231 – 238.

[51] Voiry, D.; Mohite, A.; Chhowalla, M. "Phase engineering of transition metal dichalcogenides." *Chemical Society Reviews*, **2015**, 44, 2702 – 2712.

[52] Strachan, J.; Masters, A.F.; Maschmeyer, T. "3R-MoS_2 in Review: History, Status, and Outlook." *ACS Applied Energy Materials*, **2021**, 4, 7405 – 7418.

[53] Lindström, H.; Södergren, S.; Solbrand, A.; Rensmo, H.; Hjelm, J.; Hagfeldt, A.; Lindquist, S.-E. "Li^+ Ion Insertion in TiO_2 (Anatase). 2. Voltammetry on Nanoporous Films". *Journal of Physical Chemistry B*, **1997**, 101, 7717-7722.

[54] Liu, T.-C.; Pell, W.G.; Conway, B.E. "Behavior of Molybdenum Nitrides as Materials for Electrochemical Capacitors: Comparison with Ruthenium Oxide". *Journal of the Electrochemical Society*, **1998**, 145, 1882 -1888.

[55] Wepper, W.; Huggins, R.A. "Determination of the Kinetic Parameters of Mixed-Conducting Electrodes and Application to the System Li_3Sb". *Journal of the Electrochemical Society*, **1977**, 124, 1569-1578.

[56] Verma, A.; Smith, K.; Santhanagopalan, S.; Abraham, D.; Yao, K.P.; Mukherjee, P.P. "Galvanostatic Intermittent Titration and performance Based Analysis of $LiNi_{0.5}Co_{0.2}Mn_{0.3}O_2$ Cathode". *Journal of the Electrochemical Society*, **2017**, 164, 3380-3392.

[57] Zou, J.; Li, F.; Bissett, M.A.; Kim, F.; Hardwick, L.J. "Intercalation behavior of Li and Na into 3-layer and multilayer MoS_2 flakes". *Electrochimica Acta*, **2020**, 331, 135284.

[58] Nickol, A.; Schied, T.; Heubner, C.; Schneider, M.; Michaelis, A.; Bobeth, M.; Cuniberti, G. "GITT Analysis of Lithium Insertion Cathodes for Determining the Lithium Diffusion Coefficient at Low Temperature: Challenges and Pitfalls". *Journal of the Electrochemical Society*, **2020**, 167, 090546.

[59] Zhu, Y.; Wang, C. "Galvanostatic Intermittent Titration Technique for Phase-Transformation Electrodes". *Journal of Physical Chemistry C*, **2010**, 114, 2830-2841.

[60] Cook, J.B.; Lin, T.C.; Kim, H.-S.; Siordia, A.; Dunn, B.S.; Tolbert, S.H. "Supression of Electrochemically Driven Phase Transitions in Nanostructured MoS_2 Pseudocapacitors Probed Using Operando X-ray Diffraction". *ACS Nano*, **2019**, 13, 1223-1231.

CHAPTER 4: Nucleation and Frustrated Phase Growth Investigate with *Operando* Pair Distribution Function Analysis in Mesoporous MoS_2 Pseudocapacitors

4.1 Introduction.

As global energy demand grows and we look towards electrochemical energy storage devices to provide sustainable energy solutions such as electric vehicle and smart energy grids, the need for materials that can supply both high energy density and high power density is evident.[1-2] Typical battery materials store charge through Faradaic redox reactions, which provides high energy density, but their charging time is on the scale of hours. In contrast, electric double layer capacitors (EDLC) store charge through the surface adsorption of ions, providing the ability to charge and discharge within seconds, but their energy density is lower.[3-5] Pseudocapacitors are an exciting class of materials that can bridge this gap between high energy density and high power density.[6-8]

Like batteries, pseudocapacitors store charge through redox reactions occurring through the entirety of the material. However, due to fast ion diffusion channels and reduced diffusion lengths, the current is no longer limited by slow solid-state ion diffusion, which allows pseudocapacitors to reach full charge within minutes. Therefore, pseudocapacitors utilize the charge storage mechanism of a battery while demonstrating electrochemical performance more similar to a capacitor.[4,9] A key material feature enabling pseudocapacitance is minimal structural change upon Li^+ (de)intercalation, and the lack of any significant two-phase coexistence, which is typical of most battery materials. Several *operando* X-ray diffraction (XRD) studies (including from our group) have demonstrated that suppression of first-order intercalation-induced phase

transition between the Li-rich and the Li-poor phase is well correlated with enhanced Li^+ diffusion.[10-14]

A first-order phase transition between Li-rich and Li-poor structures requires nucleation of the new phase and propagation of the phase front through the material.[15-17] Therefore, the movement of Li^+ is tied to the movement of the phase boundary. A common strategy aimed at suppression of phase transition is to increase surface area and reduce the crystal size, thereby increasing the energy penalty for maintaining a phase boundary.[18] In this case, rather than a distinct phase transition via a nucleation-and-growth type mechanism, where one observes abrupt jumps in physical properties, Li^+ intercalation induced structure change is more gradual and follows a solid-solution-like mechanism to transform from the Li-poor to the Li-rich phase.

Previous work by our group aimed to de-convolute the contribution of crystal size and lattice disorder in the suppression of intercalation-induced phase transitions in mesoporous molybdenum disulfide (MoS_2). MoS_2 presents a model system to study disorder because it is a layered material with S-Mo-S layers weakly bound by van der Waals (vdW) interactions.[19-26] Nanostructured MoS_2 can display disorder primarily in the form of stacking faults and expansion of the vdW gap. Through *operando* XRD, we showed that both reducing the crystal size and introducing lattice disorder were effective methods for suppressing phase transition between 1T-MoS_2 and triclinic Li_xMoS_2 phase.

However, *operando* diffraction only provides an average picture of the long-range structure during cycling. To gain greater insight into the local structural changes happening upon Li^+ insertion, in this work, we turn to X-ray total scattering (TS) and atomic pair distribution function (PDF) analysis.[27-32] The total scattering technique collects all elastic scattering, including both

Bragg scattering (diffraction) arising from well-ordered crystalline domains and diffuse scattering from amorphous and/or nanostructured regions of the material. After subtracting all the appropriate background signal, a Fourier transform is applied to obtain the atomic pair distribution function G(r), which gives a histogram of all atom-atom correlations within the material, regardless of whether it is crystalline or not.[33,34] To obtain a meaningful and well-resolved Fourier transform, the total scattering needs to be collected up to high scattering vectors (Q ~ 24 $Å^{-1}$), requiring the usage of high-energy synchrotron-based radiation. Therefore, PDF is a powerful tool to understand the local structure and provides information complementary to XRD, which gives a picture of average periodic structure. We have performed *operando* PDF to investigate the dynamic local structural changes occurring during Li^+ (de)intercalation.

To the best of our knowledge, this work presents the first reported *operando* PDF study on MoS_2 as a Li^+ intercalation electrode. By comparing the local structural evolution of bulk, small crystalline (sc) nanostructured, large disordered (LD) nanostructured, and small disordered (sd) nanostructured MoS_2, we discover that all samples show the appearance of a triclinic Li_xMoS_2 phase during Li^+ intercalation in the short-range. In contrast, the *operando* XRD study of all size and disorder MoS_2 samples only showed the triclinic Li_xMoS_2 phase appearing in bulk and and large crystalline (LC) nanostructured MoS_2 during Li^+ intercalation. Unfortunately, for the *operando* PDF study, we were unable to collect data on the LC-MoS_2, and therefore use bulk MoS_2 as a comparison for the largest and most ordered crystal structure. In the disordered samples (sd and LD), the coherence length of the triclinic nuclei is approximately 10 Å, while in sc-MoS_2, the coherence length extends to 20 Å. The absence of triclinic Li_xMoS_2 in XRD and its presence in PDF indicate that nucleation of the triclinic Li_xMoS_2 phase is happening on a local length scale of

1 – 2 nm. However, the effect of reducing crystal size and/or introducing lattice disorder is to prevent further growth of these triclinic Li_xMoS_2 nuclei and their organization into a long-range periodic structure. Combined with electrochemical rate capability showing that the smaller and more disordered MoS_2 enables fast-charging performance, we conclude that the growth of the Li-rich phase is rate-limiting. By frustrating this phase boundary propagation and growth through size and disorder effects, we are able to significantly improve Li^+ diffusion rate, enabling pseudocapacitive charge storage with nearly 40% capacity retention at 100C.

4.2 Experimental.

Materials: Ammonium molybdate (para) tetrahydrate $(NH_4)_6Mo_7O_{24}•4H_2O$ (99%, Alfa Aesar), ammonium persulfate (APS) (98%, Alfa Aesar), ammonium lauryl sulfate (ALS) (~30% in H_2O, Sigma Aldrich), methyl methacrylate (MMA) (contains ≤30 ppm MEHQ as inhibitor, 99%, Sigma Aldrich). Bulk MoS_2 was purchased from Beantown Chemical and stored inside an Ar glovebox. H_2S for sulfurization was purchased as a mixture of H_2 (95%)/H_2S (5%) from Airgas.

4.2.1 Synthesis of poly(methyl methacrylate) (PMMA) colloids

: PMMA colloids 60 – 80 nm in diameter were used as organic template to create a porous structure in the MoO_2 precursor. The synthesis is adapted from Wang *et al.*[35] A three-neck flask was loaded with 165 mL of milliQ water, 0.3 mL of ALS solution, and 0.075 g of APS. The solution was bubbled under N_2 for 20 – 30 mins while stirring to remove O_2 and prevent premature polymerization. Then, the three-neck flask with MMA was heated in an oil bath to 65˚C, and 12.55 mL MMA was injected. After, the reaction was stirred and heated at 70 – 75˚C for 1 hour. The final colloid solution was purified by

liquid-liquid extraction in a separatory funnel with hexanes to remove any unreacted precursors. Size of the colloids was confirmed by scanning electron microscopy. Mass density of the colloid solution was measured using thermogravimetric analysis (TGA).

4.2.2.a Synthesis of mesoporous MoO_2 precursor: Mesoporous MoO_2 was used as the precursor for the small disordered (sd) and small crystalline (sc) samples.[36] In a typical synthesis, 200 mg ammonium molybdate tetrahydrate was dissolved in the PMMA solution with a fixed amount of PMMA. The precursor solution was frozen by adding dropwise to liquid nitrogen. Once frozen, the solution was lyophilized for at least 12 hours to obtain a dried white powder. The dried powder was calcined under Ar at 675˚C for 1 hour to burn out polymer templates and crystallize the porous MoO_2. The MoO_2 product was a black powder.

4.2.2.b Synthesis of α-MoO_3 nanoparticle precursor: Nanoparticle MoO_3 was used as the precursor for the large disordered (LD) and large crystalline (LC) samples. The method is adapted from Nagabhushana *et al*.[37] Approximately 3 g (2.5 mmol) of ammonium molybdate tetrahydrate was dissolved in de-ionized water and stirred for 30 mins at RT. 5 mL of 2 M nitric acid was added to reach pH ~ 1, causing the remaining precursor to complete dissolution and the solution to clear up. Then the solution was heated at low heat (~ 60˚) for 1 hour. The h-MoO_3 product, a white powder, was washed with milliQ water and centrifuged for 10 mins at 4000 rpm. The h-MoO_3 was heated to 450˚C in a muffle furnace and soaked at 450˚C for 6 hours to produce α-MoO_3, a white powder with a grey tint.

4.2.3 Sulfurization of mesoporous MoO_2/MoO_3 to MoS_2**:** Approximately 50 mg of mesoporous MoO_2 or nanoparticle MoO_3 was ground up with mortar and pestle to expose more surface area to flowing gas. The powder was loaded into a graphite boat and placed in a tube furnace. The furnace atmosphere was purged with Ar for 30 mins to remove O_2. Then the atmosphere was changed to a mixture of H_2 (95%) /H_2S (5%). The oven was ramped to 700˚C in 1 hour and soaked for 12 hours to produce the disordered samples. The small crystalline sample was annealed at 900˚C and soaked for 12 hours. Once the furnace cooled down, the atmosphere was flushed again with Ar for 30 mins to remove any traces of H_2S. The MoS_2 product was a gray powder.

4.2.4. Materials characterization.

Scanning electron microscopy (SEM) images were obtained using a JEOL model 6700F electron microscope. X-ray diffraction (XRD) patterns were collected with a PANalytical X'Pert Pro diffractometer operating with Cu Kα (λ = 1.5418 Å) using a 0.05° step size, an accelerating voltage of 45 kV, and a current of 40 mA. XRD patterns were collected from 10 – 80˚.

4.2.5. Electrode fabrication and electrochemical characterization.

Slurry was composed of 70% active material, 10% carbon black, 10% carbon nanofibers, and 10% polyacrylic acid (PAA) as the binder. Dry powders were first ground up in a mortar and pestle several times. PAA was added as a 3% by mass solution in benzyl alcohol. The wet mixture was ground up several more times until it became a viscous paste. Slurries were cast using a doctor blade onto carbon-coated aluminum foil with ~1 mg/cm^2 mass loading and dried overnight in a vacuum oven at 140˚C to remove residual solvent. Electrode discs with area of 0.71 cm^2 were punched out and assembled inside an Ar-filled glovebox into 2032 coin cells with 2 stainless steel

spacers, a stainless steel spring, and a glass fiber separator. Polished Li foil was used as the counter and reference electrode. Commercial grade 1 M $LiPF_6$ in 1:1 ethylene carbonate (EC): dimethylene carbonate (DMC) was purchased from Sigma-Aldrich and used as the electrolyte. Before any electrochemical characterization, all samples were first pre-conditioned by galvanostatic cycling (GV) at 1C ten times to completely transform semiconducting 2H-MoS_2 to metallic 1T-MoS_2 for good conductivity.[38]

4.2.6. *Operando* XRD.

Operando diffraction experiments were conducted at the Advanced Photon Source (APS) beamline 17-BM-B. Modified coin cells were constructed for *operando* experiments. Outer casing for positive and negative electrodes were machined with a 1/8 hole in center, taped over with Kapton, while the two 0.5 mm spacers inside the cell were machined with 3/16 holes in center. 1M $LiPF_6$ in EC:DMC was used as electrolyte. Li metal was used as counter and reference electrode. X-ray energy at APS beamline 17-BM is 51.5 keV ($\lambda = 0.24075$ Å). Exposure time to x-rays ranged from 3 – 10 seconds. LaB_6 placed at the same sample-to-detector distance as the electrodes was used as calibration standard. Data integration and reduction was performed using GSAS-II.[39] Peak fitting was performed in Igor.

4.2.7. *Operando* TS/PDF.

Operando PDF measurements were performed at APS beamline 11-ID-C. Samples were pressed into pellet electrodes with a composition of 60% active material, 20% polytetrafluoroethylene (PTFE) as binder, and 20% vulcan black. Pellet electrodes were loaded in AMPIX cells with glassy carbon windows to allow for conductivity and x-ray transparency.[40-41] Cells were constructed using Li metal as counter and reference electrode, glass fiber separator, and 1M $LiPF_6$ in EC:DMC as

electrolyte. X-ray energy of 105.7 keV (λ = 0.1173 Å) was used. CeO_2 was used as a calibration standard. Exposure time to collect each pattern was approximately 5 minutes. Cycling in AMPIX cells was done galvanostatically at C/5 due to limitations in total scattering collection time. Scattering due to Li metal was masked away during 2D integration. Scattering due to electrolyte, separator, and glassy carbon was subtracted away to minimize interference in the G(r).

4.2.8. PDF simulations.

PDFgui was used to simulate reference phase PDF patterns and refine structural parameters of experimental PDF data.[42] Crystal structures for the 2H and 3R MoS_2 (Schonfeld, COD ID: 9007660) and Petkov $LiMoS_2$ (Petkov, COD ID: 1531962) phases were obtained from Crystallography Open Database.[43-44] Crystal structures for 1T-MoS_2 and triclinic $LiMoS_2$ (material ID: mp-30248) were obtained from Materials Project Database. Values of Q_{damp} = 0.038 and Q_{braod} = 0.02 were used to correct for instrument broadening. Unit cell and bond distance visualizations were performed using VESTA.[45]

4.3 Results and Discussion.

4.3.1. Material Characterization.

A matrix of size and disorder samples of nanostructured MoS_2 materials were synthesized. Small disordered (sd) and small crystalline (sc) mesoporous MoS_2 powders show crystal sizes on the order of 40 – 60 nm (**Figure 4.1a,c**), with pores sizes that correspond to the diameter of PMMA template. Large disordered (LD) MoS_2 exhibits crystal sizes of roughly 200 – 300 nm (Figure 4.1b Disorder can be observed in small domains and the randomly oriented lattice fringes found in the

high-resolution transmission electron microscope (HR-TEM) images (Figure 4.1e). The disordered samples (sd, LD) are also distinguished from the crystalline samples (sc, bulk) by the XRD patterns (Figure 4.1f), all of which can be indexed to the 2H phase of MoS_2. All nanostructure samples show broadening, but the disordered samples, in particular, show increased broadening of several peaks in the 55 – 80˚ range. In the sd-MoS_2, we note that a small amount of MoO_2 precursor remains, evidenced by the XRD peak at 26˚, but this does not significantly impact the resulting PDF data or conclusions drawn. Bulk MoS_2 consists of micro-sized particles (Figure 4.1d) and is used for reference as the largest particle size and most ordered sample.

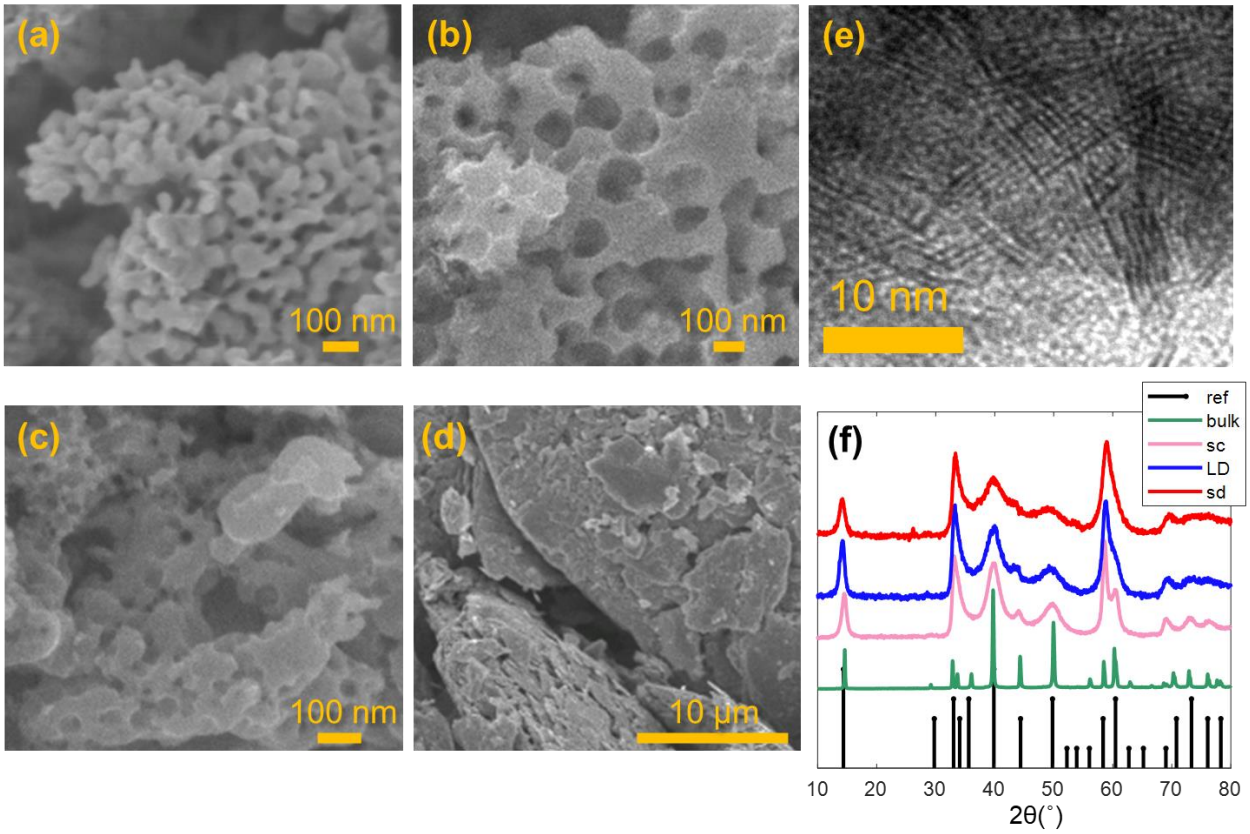

Figure 4.1. SEM images of (a) small disordered (sd), (b) Large Disordered (LD), (c) small crystalline (sc), (d) and bulk MoS_2. (e) HR-TEM image of LD MoS_2 showing disordered lattice

planes. (f) XRD patterns of bulk (forest green), sc (pink), LD (blue), sd (red) MoS_2 samples. Reference pattern of 2H-MoS_2 from JCPDS 2-0132 is shown in black sticks.

4.3.2. Simulated Total and Partial PDFs.

MoS_2 is synthesized in the semiconducting 2H phase, as shown above, but upon cycling with lithium, it is converted to the metastable metallic 1T phase.[46] Based on *operando* XRD, it then cycles between the 1T MoS_2 and triclinic Li_xMoS_2.[11] The *operando* PDF data is thus likely to show mixtures of 2H-MoS_2, 1T-MoS_2, and triclinic Li_xMoS_2 phases. We first begin with a discussion of the bond distances contributing to PDF correlations in each of these phases from simulations (**Figure 4.2**).

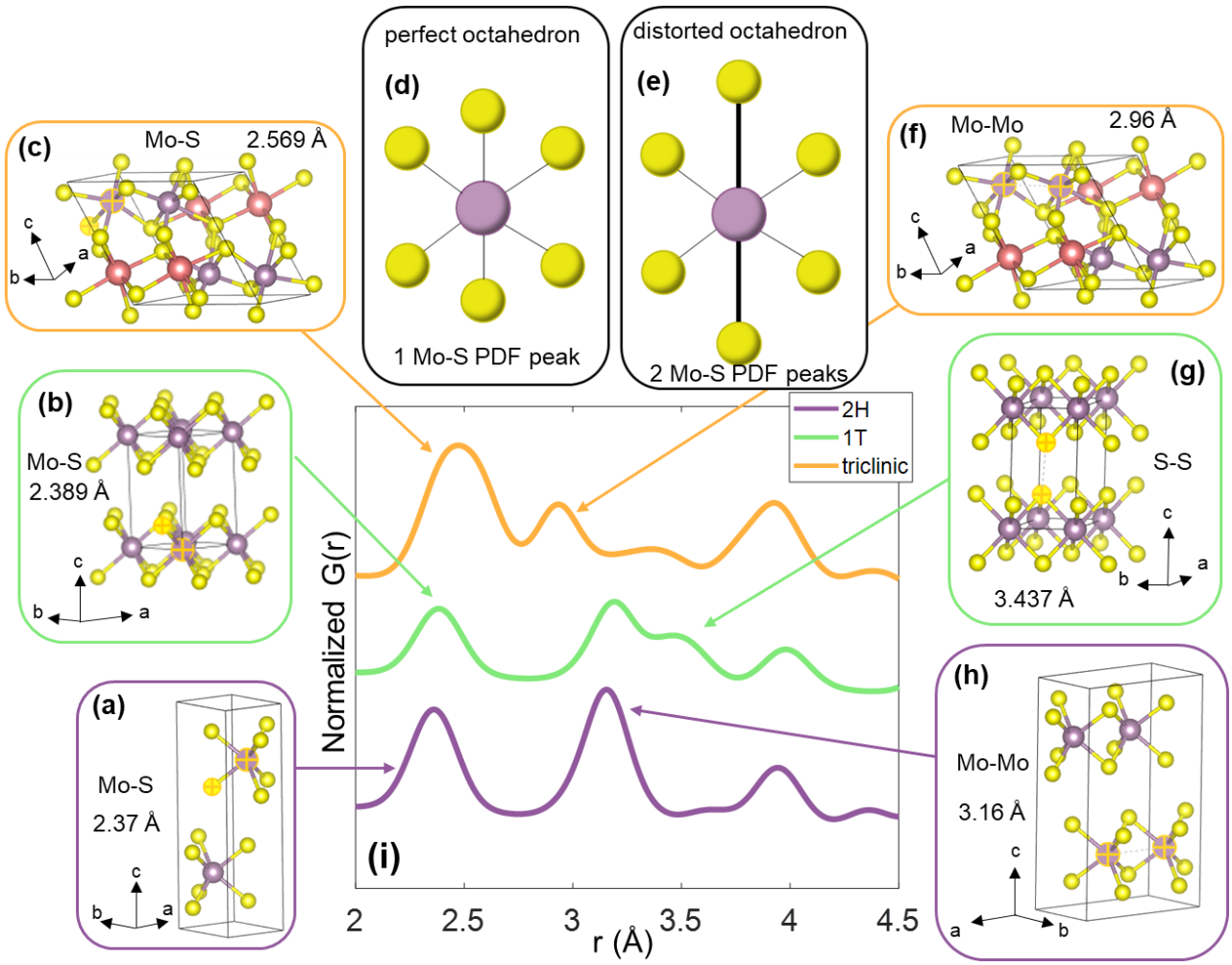

Figure 4.2. Simulated PDF patterns of 2H-MoS_2, 1T-MoS_2, and triclinic Li_xMoS_2. (a) Nearest neighbor Mo-S bonds that contribute to the correlation at 2.36 Å in 2H-MoS_2. (b) Nearest neighbor Mo-S bonds that contribute to the correlation at 2.36 Å in 1T-MoS_2. (c) Nearest neighbor Mo-S bonds in triclinic Li_xMoS_2. that contribute to the correlation at 2.47 Å. Not all Mo-S bonds in the triclinic phase are symmetric, leading to a broadening of the distribution. (d) Perfect Mo-S octahedron with all Mo-S bonds at same length will give rise to one Mo-S PDF peak. (e) Distorted Mo-S octahedron with longer axial Mo-S bonds will give rise to two Mo-S PDF peaks observed in experimental data, with axial bonds at a higher r-position and a lower intensity because there are half as many axial Mo-S bonds as equatorial Mo-S bonds. (f) Nearest Mo-Mo distance

contributing to correlation at 2.94 Å in triclinic Li_xMoS_2. (g) One of multiple sulfur-sulfur correlations across the vdW gap in 1T-MoS_2. (h) Nearest Mo-Mo distance between neighboring trigonal prisms within one layer contribute to correlate at 3.16 Å in 2H-MoS_2.

As synthesized, MoS_2 exists in the 2H structure (**Figure 4.2a**), where molybdenum sits in a trigonal prismatic coordination environment with six neighboring sulfur atoms. The unit cell has hexagonal symmetry, with lattice constants $a = b = 3.161$ Å, $c = 12.295$ Å, and angles $\alpha = \beta = 90.0^\circ$ and $\gamma = 120.0^\circ$.[47] The 2H unit cell contains two layers of trigonal prisms oriented anti-parallel to each other.[48] The first peak in the PDF pattern (Figure 4.2a) at 2.36 Å corresponds to the nearest neighbor Mo-S bond within one trigonal prism, where all Mo-S bonds are the same length.[49] The second peak at 3.16 Å contains contributions from both S-S and Mo-Mo correlations (Figure 4.2h) due to symmetry and periodicity of the unit cell. Above 4.5 Å, many peaks contain contributions from multiple atom-atom correlations, so it becomes difficult to assign them to one unique bond.

After intercalation with Li^+ (or other ions), MoS_2 undergoes a phase transition to the metastable 1T structure (**Figure 4.2b**), where each molybdenum now exists in an octahedral coordination environment with the neighboring six sulfur atoms.[50-53] The 1T unit cell also has hexagonal symmetry with lattice constants $a = b = 3.19$ Å, $c = 5.945$ Å, and angles $\alpha = \beta = 90.0^\circ$ and $\gamma = 120.0^\circ$.[54] The 1T unit cell contains one layer of octahedra. The nearest neighbor Mo-S bond gives rise to the peak at 2.36 Å (Figure 4.2b). Sulfur-sulfur distances across the vdW gap contribute to peaks at 3.44 Å (Figure 4.2g).

After transformation to 1T-MoS_2, further intercalation of Li^+ results in formation of a triclinic Li_xMoS_2 phase in bulk MoS_2 (**Figure 4.2c**).[55] The triclinic phase exhibits the least symmetry with unit cell lattice parameters a = 6.28 Å, b = 6.67 Å, c = 6.80 Å and angles $\alpha = 61.1^\circ$,

$\beta = 89.9^{\circ}$ and $\gamma = 89.8^{\circ}$. In the triclinic phase, not all Mo-S bonds are the same length (Figure 4.2c), leading to a broadening of the peak at 2.47 Å. The nearest neighbor Mo-Mo distance (Figure 4.2f) gives rise to the peak at 2.94 Å.

4.3.3. *Operando* PDF and XRD.

During (de)intercalation, bulk MoS_2 undergoes a first-order phase transition from 1T-MoS_2 to triclinic Li_xMoS_2, shown by the appearance of a new peak at Q = 1.07 $Å^{-1}$ (**Figure 4.3b**) in *operando* XRD. In contrast, the large disordered (LD) sample only shows a peak shifting, corresponding to the expansion and contraction of the vdW gap during both lithiation and delithiation, with no appearance of new peaks of the triclinic phase (Figure 4.3d). Therefore, by introducing lattice disorder and going from bulk to nanoparticle size in the LD-MoS_2, we have caused the suppression of first-order phase transition from 1T-MoS_2 to triclinic Li_xMoS_2. The galvanostatic charge and discharge curves (GV) are also consistent with this phase evolution behavior, as bulk MoS_2 shows a distinct change in slope at the voltage where the phase transition occurs (Figure 4.3a), while the GV curve of LD-MoS_2 (Figure 4.3c) shows a more gradually sloped profile. The same phase behavior is observed in sd and sc-MoS_2, where the (001) vdW gap peak shifts with no appearance of triclinic peaks. This would suggest that no phase transitions occur in the smaller or more disordered materials, however, diffraction only gives a picture of the average long-range order.

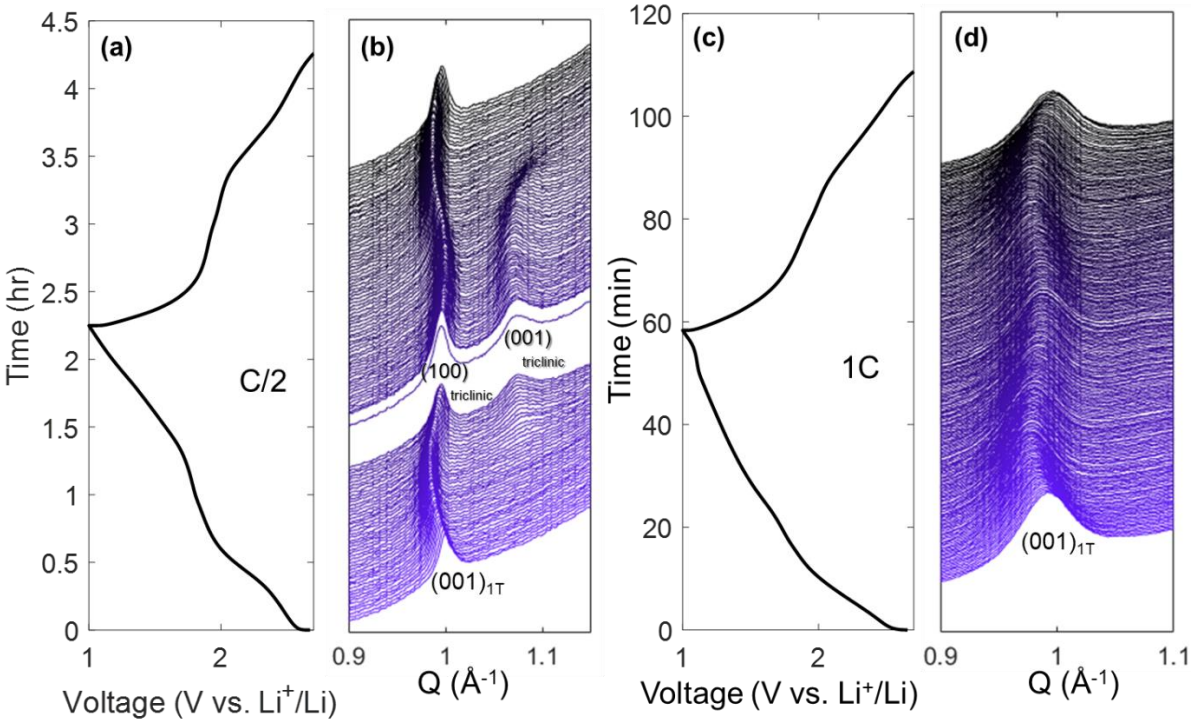

Figure 4.3. (a) Galvanostatic charge and discharge at C/2 and (b) *operando* XRD of bulk MoS_2. New peak appearing at Q = 1.07Å^{-1} corresponds to the triclinic Li_xMoS_2 phase. (c) Galvanostatic charge and discharge at 1C and (d) *operando* XRD of LD-MoS_2.

The *operando* total scattering (TS) and pair distribution function (PDF) analysis is shown for bulk MoS_2 (**Figure 4.4**). In the TS patterns (Fig 4.b), a persistent peak at Q = 1.274 Å^{-1} corresponds to the PTFE binder in the pellet electrode. In the beginning of lithiation, the TS pattern looks like a combination of 2H and 1T-MoS_2 phases, likely due to some back conversion of the metastable 1T phase, especially at Q = 2.75 Å^{-1} and Q = 3.90 Å^{-1}. At 1.76 V, we begin to see the appearance of the triclinic peak at Q = 2.16 Å^{-1}, which shifts to the 1T peak position at Q = 2.27 Å^{-1} upon delithiation. Comparing the first experimental PDF pattern at the beginning of lithiation with simulated reference PDF patterns for 2H and 1T MoS_2 (Fig 4.4.c), the local structure is also

a mixture of 2H and 1T. This is evident when looking at the peaks at 5.51 Å and 5.77 Å, as well as the pair at 6.39 Å and 6.73 Å. The small peak at 3.51 Å corresponds to the S-S distance across the van der Waals (vdW) gap (Figure 4.4.c), which increases and then decreases during both lithiation and de-lithiation. This kind of lattice expansion then contraction "breathing" behavior is consistent with the *operando* XRD (Figure 4.3) showing expansion then contraction of the (001) lattice plane during both lithiation and de-lithiation. The peak at 2.36 Å corresponds to nearest neighbor Mo-S bonds in all phases.

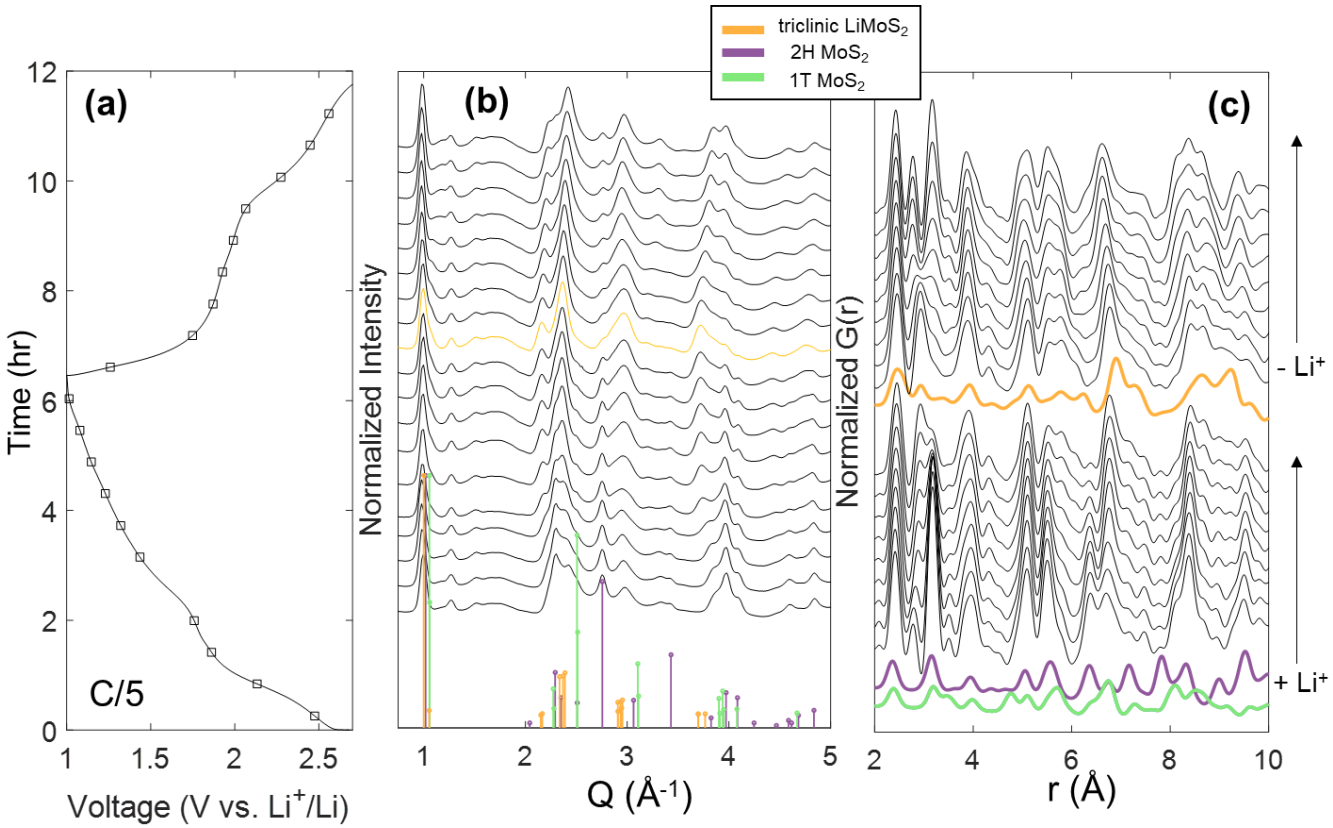

Figure 4.4. *Operando* total scattering and pair distribution function for bulk MoS_2. (a) Galvanostatic charge and discharge curve cycled at C/5. Square markers indicate voltages where total scattering patterns were taken. (b) Normalized total scattering. First delithiation scan is

plotted with a yellow line. (c) Normalized corresponding PDF patterns. Reference XRD and PDF patterns for 2H MoS_2 (purple), 1T MoS_2 (green), and triclinic $LiMoS_2$ (gold) are shown.

There is also an additional peak at 2.78 Å that does not appear in the reference pattern of 2H or 1T MoS_2 (Figure 4.2), suggesting that there are 2 distinct nearest neighbor Mo-S bond distributions. Specifically, in the 1T phase, it is assumed that Mo forms a perfect octahedron with 6 neighboring S atoms (Figure 4.2d), but the data suggests the Mo-S bonds form a distorted octahedron with 4 shorter equatorial bonds and 2 longer axial bonds (Figure 4.2e), analogous to a Jahn-Teller distortion. This is further supported by the fact that the Mo-S bond peak at 2.42 Å does not shift during cycling, while the Mo-S peak 2.78 Å gets longer and then shorter during lithiation. Therefore, the longer axial Mo-S bonds are lengthening and contracting to accommodate Li^+ during insertion and removal. At the end of lithiation at 1.0 V, the experimental pattern matches well with the triclinic Li_xMoS_2 reference pattern. Therefore, the material has been converted to triclinic Li_xMoS_2, which is consistent with phases observed in *operando* XRD (Figure 4.3).

As expected, bulk MoS_2 retains significant crystallinity during cycling, which is demonstrated by long-range correlations up to 30 Å (**Figure S4**). Though the decline in intensity after 30 Å may appear to imply there is no structural order beyond the length scale of 3 nm, we know this is not the case due to the presence of crystalline peaks through the entirety of the *operando* XRD experiment on bulk MoS_2 (Figure 4.3). Therefore, we attribute the decline in intensity of the PDF beyond 30 Å to instrument broadening and dampening effects.

We now turn to the nanostructured MoS_2 materials. In the small crystalline (sc) mesoporous MoS_2, a similar phase evolution behavior is observed (**Figure 4.5**). The TS once again

shows a mixture of 2H and 1T in the beginning of lithiation (Figure 4.5b), while the material at the end of delithiation looks more like 1T. The triclinic peak at Q = 2.18 $Å^{-1}$ appears at 1.24 V. Compared with bulk MoS_2 (Figure 4.4b), which shows the appearance of triclinic peak at 1.76 V, the effect of reducing particle size has been to increase the kinetic barrier for forming the triclinic phase. In the PDF (Figure 4.5c), a second Mo-S bond is again observed at 2.77 Å that lengthens during lithiation, which we attribute to an axial Mo-S bond changing to accommodate intercalating Li^+. The peak at 3.52 Å corresponds to a S-S correlation across the vdW gap, which expands during lithiation until correlation is lost, and contracts during de-lithiation. In the *operando* XRD of sc-MoS_2, we never observe the appearance of diffraction peaks corresponding to the triclinic $LiMoS_2$ phase. However, from the *operando* PDF, at the end of lithiation, we can see that the local structure matches well with the triclinic $LiMoS_2$ reference. This finding is significant as it suggests that long-range ordering of the lithiated phase is not necessary for fast Li^+ intercalation, and, in fact, appears to be a hindrance. By reducing the crystal size from bulk MoS_2 to sc-MoS_2, we have not suppressed formation of the triclinic phase, but instead have just reduced the ordering length scale.

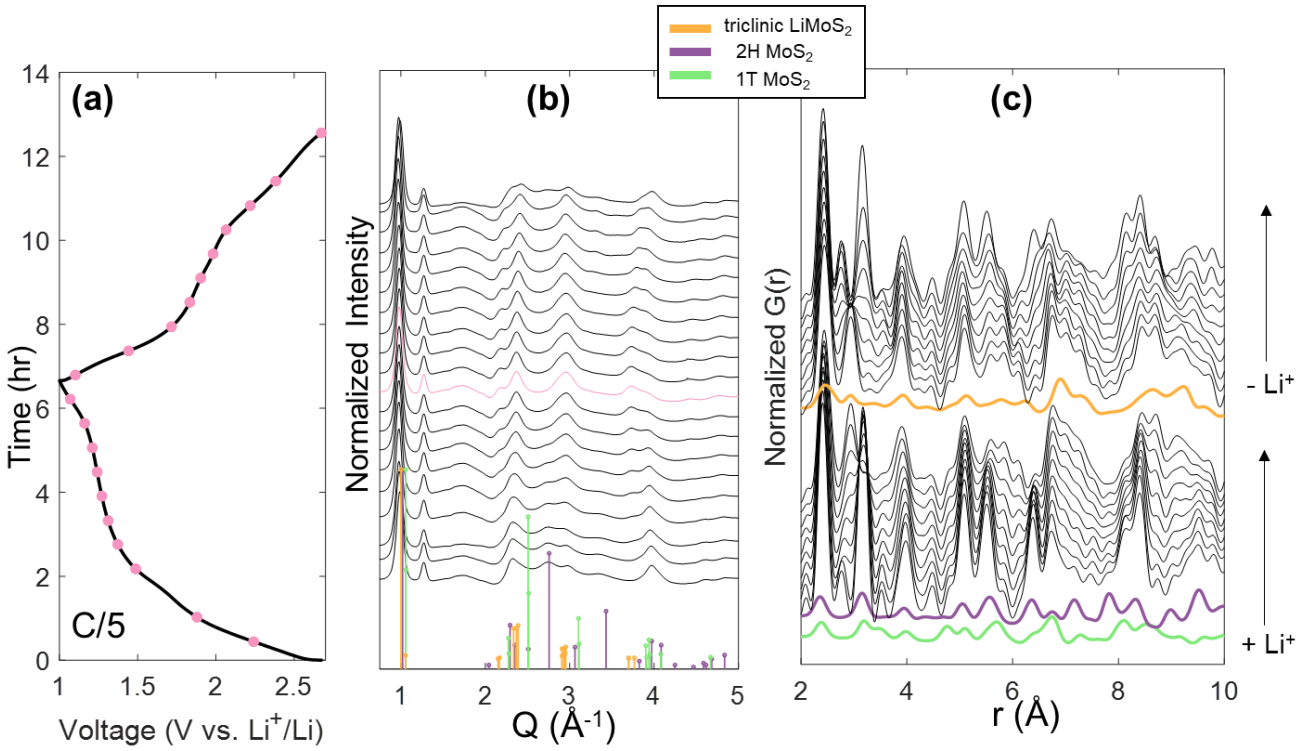

Figure 4.5. *Operando* total scattering and pair distribution function for small crystalline MoS_2. (a) Galvanostatic charge and discharge curve cycled at C/5. Pink circle markers indicate voltages where total scattering patterns were taken. (b) Normalized total scattering. First delithiation scan is plotted with a pink line. (c) Normalized corresponding PDF patterns. Simulated PDF patterns for 2H MoS_2 (purple), 1T MoS_2 (green), and triclinic $LiMoS_2$ (gold) are plotted for reference.

With this new insight, we can now attempt to quantify the length scale for triclinic ordering. Looking at the *operando* PDF of sc-MoS_2 beyond 10 Å (**Figure S5**), we can still see signatures of the triclinic $LiMoS_2$ phase at the end of lithiation up to 20 Å. In particular, the peaks at 10.65 Å and 11.61 Å stand out as characteristic features of triclinic $LiMoS_2$. In the range of 20 – 30 Å, it becomes difficult to distinguish signal from noise, although it can be argued that the peak at 24.3 Å at the beginning of delithiation corresponds to the triclinic phase. Therefore, we observe that the

sc-MoS_2 exhibits local domains of the triclinic phase up to 20 Å, despite never observing a crystalline triclinic $LiMoS_2$ phase in *operando* XRD. The difference in phases observed in *operando* XRD compared to *operando* PDF highlight the need for a paired "short-range" and "long-range" structural study to understand which structural changes are critical to enabling fast-charging behavior. From the PDF, nucleation of the triclinic phase has occurred, but the small domains of triclinic phase are limited to approximately 2 nm in size. Since the triclinic phase is not observed in XRD, these small domains are either not large enough or not ordered enough to achieve long-range "crystallinity".

When we move to the large disordered (LD) MoS_2 (**Figure 4.6**), it is evident that much correlation has been lost, as several TS (Figure 4.6b) and PDF (Figure 4.6c) peaks are broadened. In the TS, there is a more gradual evolution between the broad peaks of 1T and triclinic Li_xMoS_2 phase. The elongated axial Mo-S bond peak appears again at 2.79 Å and appears to experience a smaller magnitude of expansion and contraction. Similarly, a S-S correlation across the vdW gap at 3.5 Å shows a mild contraction until its disappearance at the end of lithiation. Although the cell was cycled at a current of C/5, each half-cycle took longer than 5 hours (Figure 4.6a) due to some back-conversion of the metastable 1T-MoS_2 to 2H-MoS_2. This can be seen in the voltage plateau around 1.1 V (Figure 4.6a) corresponding to the 1T to 2H phase transition, as well as in the PDF (Figure 4.6c) that looks like a mixture of 2H and 1T structure.

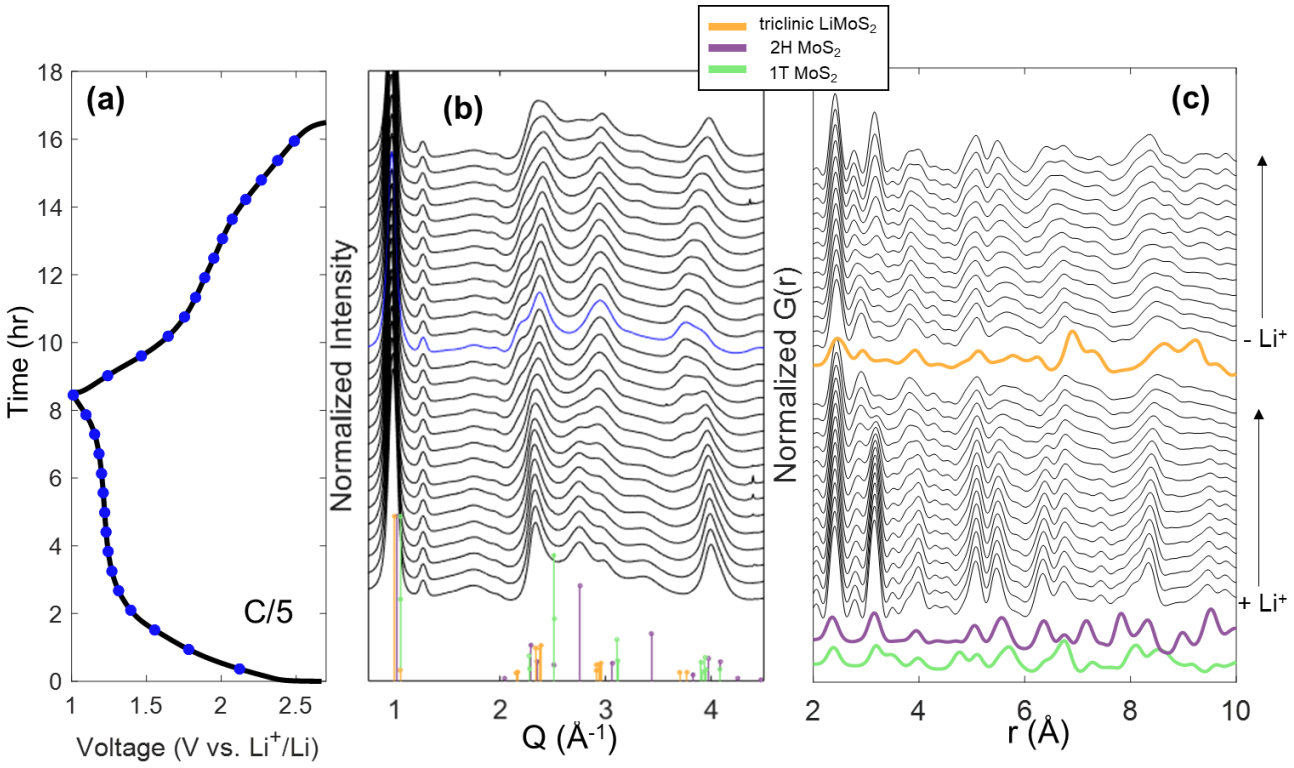

Figure 4.6. *Operando* total scattering and pair distribution function for large disordered MoS_2. (a) Galvanostatic charge and discharge curve cycled at C/5. Blue circle markers indicate voltages where total scattering patterns were taken. (b) Normalized total scattering. First delithiation scan is plotted with a blue line. (c) Normalized corresponding PDF patterns. Simulated PDF patterns for 2H MoS_2 (purple), 1T MoS_2 (green), and triclinic $LiMoS_2$ (gold) are plotted for reference.

Very similar behavior is observed in the small disordered (sd) MoS_2 sample, although this material contains a small amount of remaining MoO_2 precursor, observed in the TS by the peak at Q = 1.83 $Å^{-1}$ (**Figure 4.7b**) that shifts as MoO_2 also undergoes lithiation in this voltage window. However, the contribution of MoO_2 to the PDF (Figure 4.7c) is not significant and does not interfere with the characteristic MoS_2 correlations. From the TS peaks at Q = 2.22 $Å^{-1}$ and Q = 3.97 $Å^{-1}$ (Figure 4.7b), we see a gradual solid-solution-like evolution between the 1T and triclinic

Li_xMoS_2 phase. In the PDF (Figure 4.7c), we again observe the additional Mo-S bond at 2.78 Å which slightly expands during lithiation. A detailed discussion of the axial Mo-S bond and vdW S-S bond contraction and expansion is included in the Supporting Information (**Figure S6**).

At the end of lithiation, both the sd-MoS_2 and LD-MoS_2 PDF patterns correspond well to triclinic $LiMoS_2$ phase. In contrast, *operando* XRD of sd-MoS_2 and LD-MoS_2 never show the appearance of the triclinic $LiMoS_2$ phase. Therefore, we again conclude that local nucleation of the triclinic phase has occurred in both disordered MoS_2 samples, but growth to achieve long-range order is frustrated by the lattice disorder. In contrast to the sc-MoS_2 material, both disordered samples show no significant correlations beyond 10 Å. Therefore, we conclude that in disordered samples, the crystalline phases can again nucleate, but now they are unable to grow beyond 10 Å. The lattice disorder frustrates the growth of the phase boundary even further. By reducing the particle size, we can physically limit the phase boundary growth. By further incorporating lattice

disorder, we can limit the phase boundary to even smaller domain sizes.

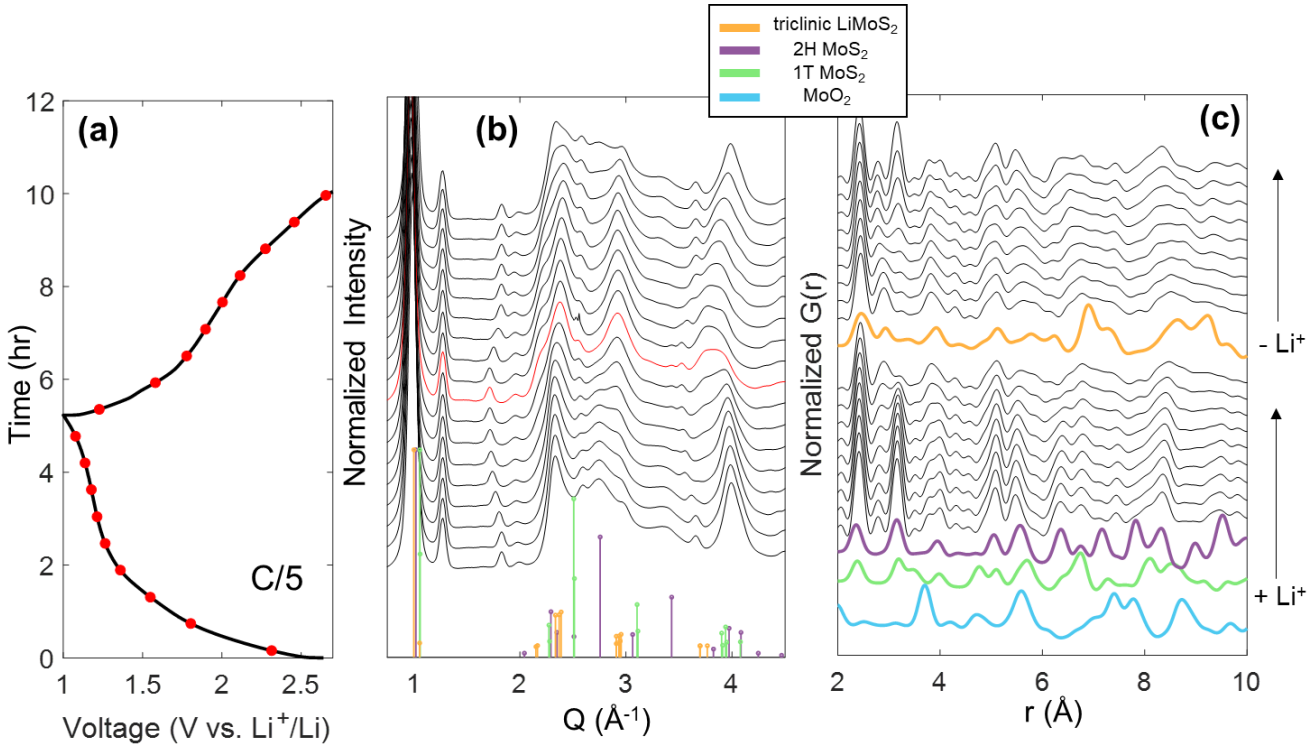

Figure 4.7. *Operando* total scattering and pair distribution function for small disordered MoS_2. (a) Galvanostatic charge and discharge curve cycled at C/5. Blue circle markers indicate voltages where total scattering patterns were taken. (b) Normalized total scattering. First delithiation scan is plotted with a blue line. (c) Normalized corresponding PDF patterns. Simulated PDF patterns for 2H MoS_2 (purple), 1T MoS_2 (green), and triclinic $LiMoS_2$ (gold) are plotted for reference.

Because the sample PDF patterns show correlations coming from multiple phases, a multi-phase refinement was carried out (**Figure 4.8**) to determine how much of the short-range structure resembles 2H-MoS_2, 1T-MoS_2, and triclinic Li_xMoS_2 phases. It is interesting to note that, while all samples begin as a mixture of 2H and 1T (which may be expected as some of the metastable 1T back-converts to 2H), the local structure looks predominantly like the 2H phase. In both the

bulk and large disordered MoS_2 (Figure 4.8b,d), the starting material shows a higher percentage of 2H (~80%) than the smaller samples (Figure 4.8a,c), which begin at roughly 70% 2H composition. In both disordered samples (Figure 4.8a,b), a greater percentage of 1T-MoS_2 persists throughout the cycling. Therefore, introducing lattice disorder appears to stabilize the 1T structure. The stabilization of the 1T structure may be attributed to the fact that lattice disorder frustrates the propagation of a phase boundary; therefore, even if local domains back-convert to 2H, a higher degree of the conductive 1T matrix is maintained. As expected, the bulk MoS_2 reaches the highest composition of triclinic Li_xMoS_2 (87% at end of lithiation). Small crystalline, large disordered, and small disordered reach 80%, 74%, and 73% triclinic Li_xMoS_2 at the end of lithiation, respectively. Again, these phase percentages from PDF represent the local structure on the scale of 10 Å, in contrast with the *operando* XRD data, where none of the sd, sc, or LD samples show triclinic diffraction peaks. This observation shows that in the short-range, the phase behavior of all samples is quite similar, with the triclinic Li_xMoS_2 phase forming upon Li^+ intercalation in all cases. Reducing the crystal size and introducing lattice disorder both inhibit further growth of this phase into larger, more ordered domains, and the effect of disorder appears to be more limiting than size alone.

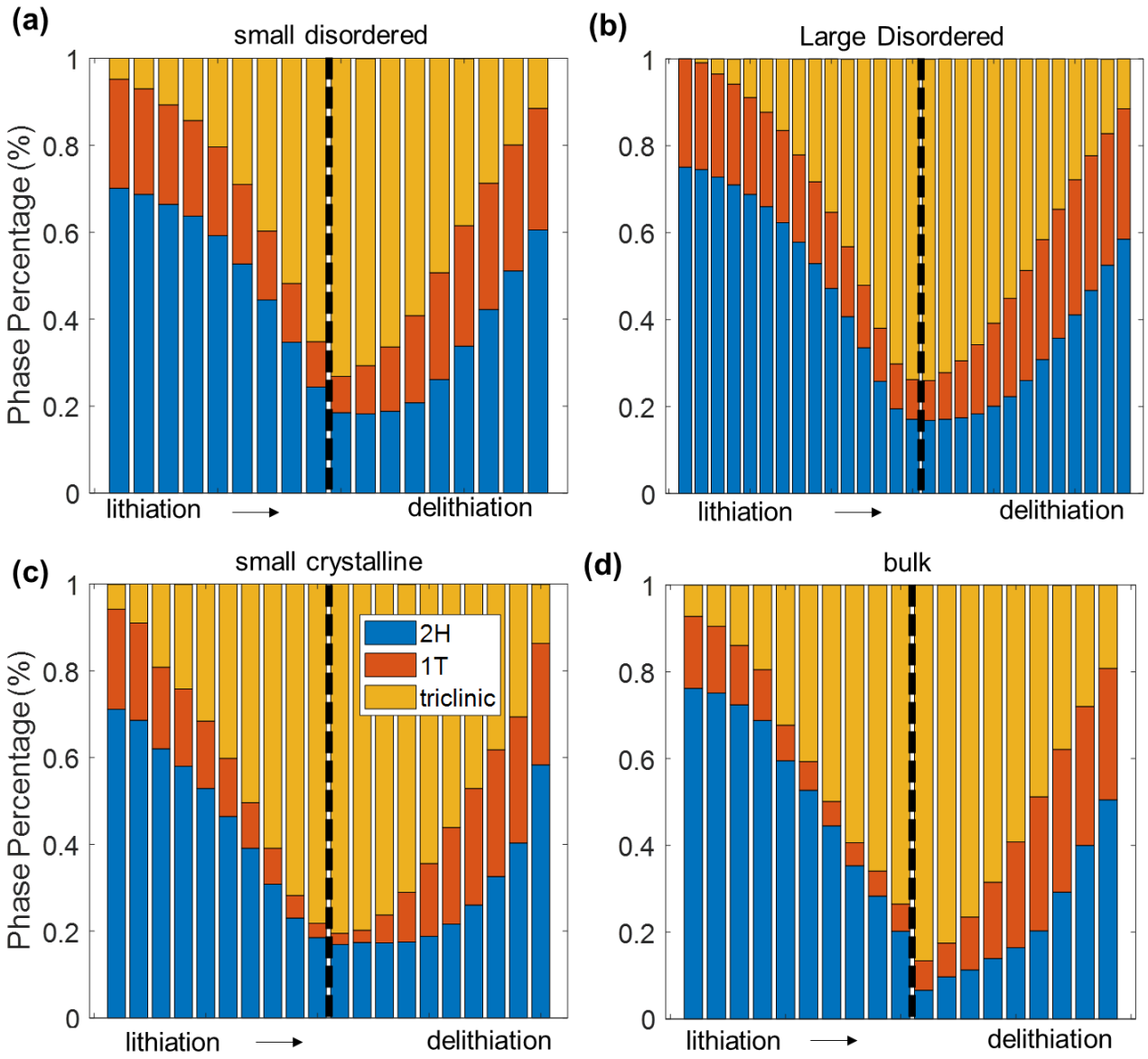

Figure 4.8. Multi-phase refinement in the 0 – 10 Å range of PDF pattern for (a) small disordered, (b) Large Disordered, (c) small crystalline, and (d) bulk MoS_2, showing the percentage of 2H-MoS_2, 1T-MoS_2, and triclinic Li_xMoS_2 present during each PDF pattern throughout the *operando* experiment. Black dotted line indicates the end of lithiation. Percentage is calculated from the fraction of each phase of total refined scale factors.

4.3.4. Electrochemical Characterization.

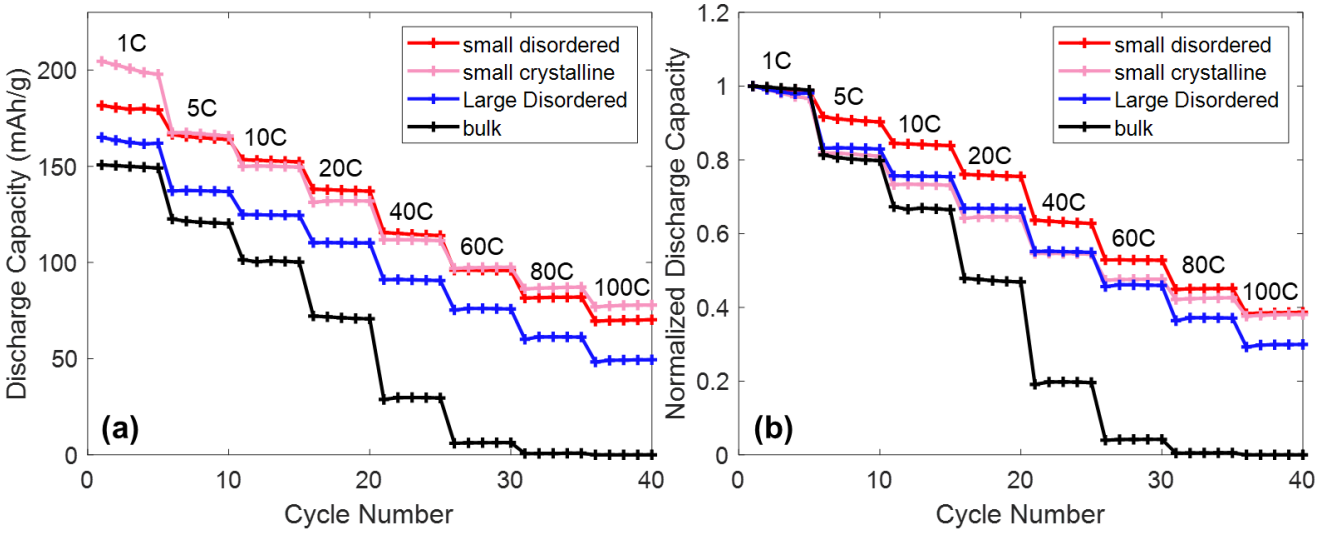

Figure 4.9. (a) Rate capability of bulk, LD, sc, and sd mesoporous MoS_2, reported as discharge capacity. (b) Discharge capacity, normalized to the obtained 1C capacity to show percentage drop.

The bulk and mesoporous MoS_2 samples were fabricated into slurry electrodes and assembled into coin cells to correlate observed structural changes with electrochemical performance. All cells were pre-cycled galvanostatically at 1C to complete the 2H to 1T transition for optimal conductivity before rate testing. Rate capability (**Figure 4.9a**) shows that bulk MoS_2 has lost 50% of the 1C capacity by 20C (charge in 3 minutes). In contrast, the large disordered (LD) MoS_2 is able to provide 49 $mAh \cdot g^{-1}$ at 100C (charge in 40 seconds). The small disordered (sd) MoS_2 provides 70 $mAh \cdot g^{-1}$ at 100C, and the small crystalline (sc) MoS_2 provides 78 $mAh \cdot g^{-1}$ at 100C. For ease of comparison, we also show the rate-dependent discharge capacity normalized to 1C capacity (Figure 4.9b). From this plot, it is evident that both sc and sd MoS_2 retain 38% of the 1C capacity when discharged at 100C. Therefore, both increased lattice disorder and decreased particle size, can allow for faster Li^+ intercalation. The sample with both effects (sd), shows the

highest relative capacity retention at all rates, but the absolute capacity for the crystalline material is slightly higher.

4.4 Conclusions.

From our paired *operando* XRD and *operando* PDF investigation, we have been able to elucidate the dynamic evolution of both short-range and long-range structure in mesoporous MoS_2 samples. We observe that in all samples (bulk, sc, LD, and sd), the nearest neighbor Mo-S bond distances are not equivalent, even though they should be in both the 2H and 1T phases. There exist 2 distinct bond lengths corresponding to a shorter equatorial Mo-S bond and a longer axial Mo-S bond in a distorted octahedron, analogous to a Jahn-Teller distortion. This additional Mo-S bond is not observed in ambient powder PDF of as-synthesized MoS_2, and therefore is a form of disorder introduced during cycling. The most significant finding is that although *operando* XRD of sd, sc, and LD-MoS_2 do not show any evidence of crystalline triclinic $LiMoS_2$ phase, the *operando* PDF demonstrates that the local structure of all three nanostructured samples does resemble triclinic $LiMoS_2$ upon lithiation, similar to the bulk material. The coherence length of the triclinic domains differ by sample, however, with the sc-MoS_2 showing coherent order up to ~20 Å, while the LD-MoS_2 and sd-MoS_2 domain sizes are only ~10 Å.

These results thus show that the intercalation of Li^+ into mesoporous MoS_2 does result in transformation to a structure with local triclinic $LiMoS_2$ order, but the effect of reducing crystal size and/or introducing lattice disorder appears to be to prevented growth of triclinic domains beyond the 10 – 20 Å length scale, and to frustrate the formation of domains with long-range order. While this material was reported to show suppression of intercalation driven phases transitions, those phase transitions appear to still take place locally, but the discrete first-order transition is converted into a solid-solution type transition with very short coherence lengths. Taken together

with the electrochemical rate performance of each sample, we can conclude that long-range order is not necessary for inducing pseudocapacitive charge storage. On the contrary, the formation of long-range order appears to be the rate-limiting process in the overall (de)-intercalation mechanism.

4.5 References.

[1] Dedes, I.-C.; Tsampasis, E.; Elias, C.; Gkonis, P. "Energy Storage in Smart Electrical Grids." 10th Mediterranean Conference on Embedded Computing (MECO), 2021, p. 1 – 4. doi: 10.1109/MECO52532.2021.9460169.

[2] Blomgren, G. E. The Development and Future of Lithium Ion Batteries. *Journal of The Electrochemical Society*. **2017**, 164, A5019.

[3] Simon, P., et al. Where Do Batteries End and Supercapacitors Begin? *Science.* **2014**, 343, 1210 – 1211.

[4] Augustyn, V., et al. Pseudocapacitive oxide material for high-rate electrochemical energy storage. *Energy & Environmental Science.* **2014**, 7, 1597 – 1614.

[5] Whittingham, M. Stanley. "Lithium Batteries and Cathode Materials." *Chemical Reviews*, **2004**, 104, 4271 – 4301.

[6] Fleischmann, S., et al. Pseudocapacitance: From Fundamental Understanding to High Power Energy Storage Materials. *Chem. Rev*. **2020**, 120, 6738 - 6782.

[7] Conway, B.E., et al. Double-layer and pseudocapacitance types of electrochemical capacitors and their applications to the development of hybrid devices. *J. Solid State Electrochem*. **2003**, 7, 637 – 644.

[8] Zhang, X.-L.; Zhang, W.-B.; Han, X.-W.; Zhang, L.; Bao, X.; Guo, Y.-W.; Chai, S.-S.; Guo, S.-B.; Zhou, X.; Ma, X.-J. "Review – Pseudocapacitive Energy Storage Materials from Hägg-Phase Compounds to High-Entropy Ceramics." *Journal of The Electrochemical Society*, **2021**, 168, 120521.

[9] Ardizzone, S.; Fregonara, G.; Trasatti, S. " 'Inner' and 'outer' active surface of RuO_2 electrodes." *Electrochimica Acta*, **1990**, 35, 263 – 267.

[10] Kim, H.-S., et al. The Development of Pseudocapacitive Properties in Nanosized-MoO_2. *Journal of The Electrochemical Society.* **2015**, 162 (5), 5083 – 5090.

[11] Cook, J.B., et al. Suppression of Electrochemically Driven Phase Transitions in Nanostructure MoS_2 Pseudocapacitors Probed Using Operando X-ray Diffraction. *ACS Nano.* **2019**, 13, 1223 – 1231.

[12] Moshtev, R.V.; Zlatilova, P.; Manev, V.; Sato, A. "The $LiNiO_2$ solid solution as a cathode material for rechargeable lithium batteries". *Journal of Power Sources*, **1995**, 54, 329 – 333.

[13] Biasi, L.; Schiele, A.; Roca-Ayats, M.; Garcia, G.; Brezesinski, T.; Hartmann, P.; Janek, J. "Phase Transformation Behavior and Stability of $LiNiO_2$ Cathode Material for Li-Ion Batteries Obtained from In Situ Gas Analysis an Operando X-Ray Diffraction". *ChemSusChem*, **2019**, 12, 2240 – 2250.

[14] Castro-García, S.; Castro-Coucerio, A.; Señarís-Rodríguez, M.A.; Soulette, F.; Julien, C. "Influence of aluminum doping on the properties of $LiCoO_2$ and $LiNi_{0.5}Co_{0.5}O_2$ oxides". *Solid State Ionics*, **2003**, 156, 15 – 26.

[15] Orikasa, Y.; Maeda, T.; Koyama, Y.; Murayama, H.; Fukuda, K.; Tanida, H.; Arai, H.; Matsubara, E.; Uchimoto, Y.; Ogumi, Z. "Transient Phase Change in Two Phase Reaction between $LiFePO_4$ and $FePO_4$ under Battery Operation." *Chemistry of Materials*, **2013**, 25, 7, 1032 – 1039.

[16] Hou, P.; Chu, G.; Gao, J.; Zhang, Y.; Zhang, L. "Li-ion batteries: Phase transition." *Chinese Physics B*, **2016,** 25(1):016104.

[17] Van der ven, A.; Bhattacharya, J.; Belak, A.A. "Understanding Li Diffusion in Li-Intercalation Compounds." *Accounts of Chemical Research*, **2013**, 46, 1216 – 1225.

[18] Zhang, X.; van Hulzen, M.; Singh, D.P.; Brownrigg, A.; Wright, J.P.; van Dijk, N.H.; Wagemaker, M. "Direct view on the phase evolution in individual $LiFePO_4$ nanoparticles during Li-ion battery cycling." *Nature Communications*, **2015**, 6, 8333.

[19] Zhao, Y.; Zhang, Y.; Yang, Z.; Yan, Y.; Sun, K. "Synthesis of MoS_2 and MoO_2 for their applications in H_2 generation and lithium ion batteries: a review." *Science and Technology of Advanced Materials*, **2013**, 14, 1 – 12.

[20] Wang, H.; Yuan, H.; Hong, S.S.; Li, Y.; Cui, Y. "Physical and chemical tuning of two-dimensional transition metal dichalcogenides." *Chemical Society Reviews*, **2015**, 44, 2664.

[21] Tedstone, A.A.; Lewis, D.J.; O'Brien, P. "Synthesis, Properties, and Applications of Transition Metal-Doped Layered Transition Metal Dichalcogenides." *Chemistry of Materials*, **2016**, 28, 1965 – 1974.

[22] Li, Y.; Zhang, Y.; Tong, X.; Wang, X.; Zhang, L.; Xia, X.; Tu, J. "Recent progress on the phase modulation of molybdenum disulphide/diselenide and their applications in electrocatalysis." *Journal of Materials Chemistry A*, **2021**, 9, 1418 – 1428.

[23] Stephenson, T.; Li, Z.; Olsen, B.; Mitlin, D. "Lithium ion battery applications of molybdenum disulfide (MoS_2) nanocomposites". *Energy & Environmental Science*, **2014**, 7, 209-231.

[24] Huang, X.; Zeng, Z.; Zhang, H. "Metal dichalcogenide nanosheets: preparation, properties and applications." *Chemical Society Reviews*, **2013**, 42, 1934-1946.

[25] Hu, X.; Zhang, W.; Liu, X.; Mei, Y.; Huang, Y. "Nanostructured Mo-based electrode materials for electrochemical energy storage". *Chemical Society Reviews*, **2015**, 44, 2376-2404.

[26] Voiry, D.; Mohite, A.; Chhowalla, M. "Phase engineering of transition metal dichalcogenides." *Chemical Society Reviews*, **2015**, 44, 2702 – 2712.

[27] Egami, T. and Billinge, S.J.L. *Underneath the Bragg Peaks: Structural Analysis of Complex Materials*; Pergamon, 2003.

[28] Jeong, I.-K.; Proffen, T.; Mahiuddin-Jacobs, F.; Billinge, S.J.L. "Measuring Correlated Atomic Motion Using X-ray Diffraction." *Journal of Physical Chemistry A*, **1999**, 103, 921 – 924.

[29] Hwang, S.-J.; Petkov, V.; Rangan, K.K.; Shastri, S.; Kanatzidis, M.G. "Structure of Nanocrystalline Materials with Intrinsic Disorder from Atomic Pair Distribution Function Analysis: The Intercalation Compound Ag_xMoS_2." *Journal of Physical Chemistry B*, **2002**, 106, 12453 – 12458.

[30] Key, B.; Morcrette, M.; Tarascon, J.-M.; Grey, C.P. "Pair Distribution Function Analysis and Solid State NMR Studies of Silicon Electrodes for Lithium Ion Batteries: Understanding the (De)lithiation Mechanisms." *JACS*, **2010**, 133, 503 – 512.

[31] Wang, X.; Tan, S.; Yang, X.-Q.; Hu, E. "Pair distribution function analysis: Fundamentals and application to battery materials." *Chinese Physics B*, **2020**, 29, 028802.

[32] Chapman, K.W. "Emerging *operando* and x-ray pair distribution function methods for energy materials development." *MRS Bulletin*, **2016**, 41, 231 – 238.

[33] Billinge, Simon J.L. "The rise of the X-ray atomic pair distribution function method: a series of fortunate events." *Phil. Trans. R. Soc. A.*, **2019**, 377:20180413.

[34] Diaz-Lopez, M.; Cutts, G.L.; Allan, P.K.; Keeble, D.S.; Ross, A.; Pralong, V.; Spiekermann, G.; Chater, P.A. "Fast operando X-ray pair distribution function using the DRIX electrochemical cell." *Journal of Synchrotron Radiation*, **2020**, 27, 1190 – 1199.

[35] Wang, T.; Sel, O.; Djerdj, I.; Smarsly, B. "Preparation of a large Mesoporous CeO_2 with crystalline walls using PMMA colloidal crystal templates." *Colloid Polymer Science*, **2006**, 285, 1-9.

[36] Yan, Y.; Chin, M.A.; Robertson, D.D.; Lesel, B.K.; Tolbert, S.H. "Tuning the Porous Structure in PMMA-Templated Mesoporous MoO_2 for Pseudocapacitive Li-Ion Electrodes." *Journal of the Electrochemical Society*, **2022**, 169, 040545.

[37] Nagabhushana, G.P.; Samrat, D.; Chandrappa, G.T. "α-MoO_3 nanoparticles: solution combustion synthesis, photocatalytic and electrochemical properties." *RSC Advances*, **2014**, 4, 56784.

[38] Jiao, Y.; Hafez, A.M.; Cao, D.; Mukhopadyay, A.; Ma, Y.; Zhu, H. "Metallic MoS_2 for High Performance Energy Storage and Energy Conversion." *Small*, **2018**, 14, 1 – 20.

[39] Toby, B.H. and R.B. Von Dreele. "GSAS-II: the genesis of a modern open-source all purpose crystallography software package." *Journal of Applied Crystallography*, **2013**, 46, 544 – 549.

[40] Borkiewicz, O.J.; Shyam, B.; Wiaderek, K.M.; Kurtz, C.; Chupas, P.J.; Chapman, K.W. "The AMPIX electrochemical cell: a versatile apparatus for in situ X-ray scattering and spectroscopic measurements." *Journal of Applied Crystallography*, **2012**, 45, 1261 – 1269.

[41] Borkiewicz, O.J.; Wiaderek, K.M.; Chupas, P.J.; Chapman, K.W. "Best Practices for Operando Battery Experiments: Influences of X-ray Experiment Design on Observed Electrochemical Reactivity." *Journal of Physical Chemistry Letters*, **2015**, 6, 2081 – 2085.

[42] Farrow, C.L.; Juhas, P.; Liu, J.W.; Bryndin, D.; Bozin, E.S.; Block. J.; Proffen, Th.; and S.J.L. Billinge. "PDFfit2 and PDFgui: computer programs for studying nanostructure in crystals." *J. Phys.: Condens. Mat.*, **2007**, 19, 335219.

[43] Schonfeld, B.; Huang, J.J.; Moss, S. C. "Anisotropic mean-square displacements (MSD) in single crystals of 2H- and 3R-MoS_2." *Acta Crystallographica, Section B*, **1983**, 39, 404 – 407.

[44] Petkov, V.; Vogt, T.; Billinge, S.J.L.; Mahanti, S.D.; Larson, P.; Rangan, K.K.; Kanatzidis, M.G. "Structure of nanocrystalline materials using atomic pair distribution function analysis: study of $LiMoS_2$." Physical Review, Series 3. B – Condensed Matter, **2002**, 65, 921051 – 921054.

[45] Momma, K.; Izumi, F. "VESTA 3 for three-dimensional visualization of crystal, volumetric and morphology data." *Journal of Applied Crystallography*, **2011**, 44, 1272 – 1276.

[46] Julien, C.M. "Lithium intercalated compounds: Charge transfer and related properties." *Materials Science and Engineering R*, **2003**, 40, 47 – 102.

[47] Balendhran, S.; Walia, S.; Nili, H.; Ou, J.Z.; Zhuiykov, S.; Kaner, R.B.; Sriram, S.; Bhaskaran, M.; Kalantar-zadeh, K. "Two-Dimensional Molybdenum Trioxide and Dichalcogenides." *Advanced Functional Materials*, **2013**, 23, 3952 – 3970.

[48] Strachan, J.; Masters, A.F.; Maschmeyer, T. "3R-MoS_2 in Review: History, Status, and Outlook." *ACS Applied Energy Materials*, **2021**, 4, 7405 – 7418.

[49] Petkov, V.; Vogt, T.; Billinge, S.J.L.; Mahanti, S.D.; Larson, P.; Rangan, K.K.; Kanatzidis, M.G. "Structure of nanocrystalline materials using atomic pair distribution function analysis: study of $LiMoS_2$." Physical Review, Series 3. B – Condensed Matter, **2002**, 65, 921051 – 921054.

[50] Jin, Q.; Liu, N.; Chen, B.; Mei, D. "Mechanisms of Semiconducting 2H to Metallic 1T Phase Transition in Two-dimensional MoS_2 Nanosheets". *Journal of Physical Chemistry C*, **2018**, 122, 28215-28224.

[51] Wypych, F.; Schöllhorn, R. "1T-MoS_2, a New Metallic Modification of Molybdenum Disulfide". *Journal of the Chemical Society, Chemical Communications*, **1992**, 1386-1388.

[52] Gan, X.; Lee, L.Y.S.; Wong, K.-Y.; Lo, T.W.; Ho, K.H.; Lei, D.Y.; Zhao, H. "2H/1T Phase Transition of Multilayer MoS_2 by Electrochemical Incorporation of S Vacancies". *ACS Applied Energy Materials*, **2018**, 1, 4754-4765.

[53] Mattheiss, L.F. "Band Structures of Transition-Metal-Dichalcogenide Layer Compounds". *Physical Review B*, **1973**, 8, 3719-3740.

[54] Zhao, W.; Pan, J.; Fang, Y.; Che, X.; Wang, D.; Bu, K.; Huang, F. "Metastable MoS_2: Crystal Structure, Electronic Band Structure, Synthetic Approach and Intriguing Physical Properties." *Chem. Eur. J*. **2018**, 24, 15942 - 15954.

[55] Benavente, E.; Santa Ana, M.A.; Mendizabal, F.; Gonzalez, G. "Intercalation chemistry of molybdenum disulfide." *Coordination Chemistry Reviews*, **2002**, 224, 87 – 109.

CHAPTER 5: Improving Structural and Long-Term Stability in SbSn Alloy Anodes via Control of Nanoarchitectures and Intermediates

5.1 Introduction.

Lithium-ion batteries (LIB) have demonstrated enormous success in powering our everyday portable electronics such as smartphones and laptops.[1-3] However, as we look towards future applications such as electric vehicles and smart electrical grids, significant advancements in energy density are required.[4-6] Graphite is currently the most popular anode material of choice, providing a gravimetric capacity of 372 $mAh \cdot g^{-1}$ with a one electron intercalation reaction to form LiC_6, but charging beyond this capacity can lead to problems such as Li metal plating.[7-9] Therefore, to increase the cell energy density, it would be advantageous to utilize a material that can reversibly accommodate more than one Li-ion.

Alloy anode materials are an attractive candidate to replace graphite, as they are typically metalloid or metallic elements such as Si, Ge, Sn, Sb, Pb, or Bi that alloy with Li^+, which allows them to accommodate several more Li^+ per unit cell than an intercalation material.[10-12] This charge storage mechanism affords alloy anodes much higher gravimetric and volumetric capacities. For reference, Si, Sn, and Sb can provide 3579 mAh/g, 990 mAh/g, and 660 mAh/g, respectively.[13-14] However, since the Li^+ insertion forms an alloy with the material, huge structural rearrangements and volume expansion are induced. Again, Si, Sn, and Sb undergo 280%, 260%, and 147% volume expansion, respectively.[15] Repeated cycling causes mechanical stress, crack formation, which leads to disconnection of active material from the current collector and capacity fade. Therefore,

significant research efforts have been focused on strategies for alleviating the volume expansion issue.

Previous work in our group has demonstrated the synthesis of a nanoporous antimony-tin (SbSn) intermetallic through de-alloying reaction and used transmission x-ray microscopy (TXM) to show that the volume expansion is less severe and more reversible than in pure Sn.[16-18] The nanoporous structure allows the material to expand into the pore volume while maintaining a connected network during lithiation. Because Sb and Sn can both alloy with Li^+, but at different voltages, one component acts an inactive matrix to buffer the volume expansion during lithiation of the other.[19] Sn affords a large gravimetric capacity of 990 mAh/g, while Sb undergoes a relatively smaller volume expansion (147%) compared to other alloying materials. Therefore, the combined intermetallic crystal structure and nanoporous architecture enable more reversible lithiation behavior and mitigate long-term capacity fade due to volume expansion.

However, we still have a limited understanding of the dynamic structural changes that occur during lithiation and de-lithiation because much of the material becomes very disordered and nearly amorphous after the first cycle. The extent of lithiation of Sn is unclear because several higher lithiated Sn phases are reported to be stable in pure Sn (e.g. Li_7Sn_3, Li_5Sn_2, $Li_{13}Sn_5$, Li_7Sn_2, $Li_{17}Sn_4$, and $Li_{22}Sn_5$) but have not been demonstrated in the intermetallic.[20-22] Therefore, we have performed a combined *operando* x-ray diffraction (XRD) and pair distribution function analysis (PDF) study on our nanoporous SbSn electrode to determine crystalline phases formed *in situ*, as well as local structure of the remaining disordered material.

The x-ray total scattering (TS) / pair distribution function analysis (PDF) method collects both Bragg scattering and diffuse scattering from the material up to high Q ~ 25 $Å^{-1}$, where Q is the scattering vector and related to the lattice spacing, d, and scattering angle, θ, by the equation:

$Q = \frac{4\pi}{\lambda} sin(\theta) = \frac{2\pi}{d}$.[23] Bragg scattering is the diffraction signal due to the crystalline materials with long-range order, while diffuse scattering comes from elastic scattering of disordered or nanostructured materials. By taking the Fourier transform of the TS intensity, we obtain the pair distribution function (PDF), which effectively gives a histogram of all atom-atom correlations within the material, regardless of long-range order.[24-25] Therefore, PDF allows us to characterize the structure of amorphous material formed during lithiation and de-lithiation.[26-29]

In this work, we have synthesized both a bulk and nanoporous SbSn alloy anode to understand the effect of nanoscale architecture on improving the kinetics of phase separation and re-mixing of the alloy during cycling. We also characterize both crystalline and amorphous intermediates formed with paired *operando* XRD and PDF. We demonstrate that the phase-separation of nanoporous SbSn into crystalline Li_3Sb and β-Sn during first lithiation of Sb is much more facile than in the bulk, suggesting that the nanoporous structure by shortening the distance which Li^+ must travel to form domain of Li_3Sb. In the *operando* XRD, we do not observe any crystalline lithiated tin phases in the final product, but through *operando* PDF, we have determined that the amorphous lithiated tin phases resemble Li_7Sn_3 in the short-range. We postulate that the amorphous nature of the lithiated tin phase provides an additional ductile matrix to buffer volume expansion during cycling.

5.2 Experimental.

5.2.1. Synthesis of bulk SbSn alloy**:**

A parent alloy of $Sb_{20}Sn_{80}$ was synthesized by melting the stoichiometric amounts of Sb metal and Sn metal in a quartz ampule under Ar at 700°C, then cooled to room temperature. To make a

homogeneous alloy, the alloy was then heated and cooled several times at 400 °C. The extra Sn in the parent alloy was then etched away with a 4 M HBr.

5.2.2. Synthesis of nanoporous SbSn alloy**:**

Stoichiometric ratios of elemental Sn and Sb are mixed in a quartz ampule and placed in a 700˚C oven for five days to achieve a 55:45 Sb:Sn ratio alloy, which is the intermetallic phase. This intermetallic SbSn is then cryomilled. 10 mL of room temperature 5.93M HBr is introduced to the cryomilled SbSn powder. (30mgs yields ~12mgs of NP-SbSn and 20mgs ~ 8mgs) After 30 minutes of selective dealloying, the reaction is quenched with water and rinsed extensively with deionized water. The powder is dried in the Schlenk vacuum line to remove residual water.

5.2.3. Material characterization**:**

Scanning electron microscopy (SEM) images and energy dispersive spectroscopy (EDS) data were obtained using a JEOL model 6700F electron microscope. X-ray diffraction (XRD) patterns were collected with a PANalytical X'Pert Pro diffractometer operating with Cu Kα ($\lambda = 1.5418$ Å) using a 0.05° step size, an accelerating voltage of 45 kV, and a current of 40 mA.

5.2.4. Electrode fabrication and electrochemical characterization**:**

The nanoporous (NP) SbSn slurries were fabricated in a 70:15:15 ratio of active material: carbon nanofibers: carboxymethylcellulose (CMC), which is added as a 3% by weight solution in water. Each solid component (active and carbon fibers) is weighed and ground in a mortar and pestle. Once the powder is homogenous, 2 drops of deionized (DI) water are added to the mortar and pestle, then mixed. Then, the CMC solution is added and mixed in to create a more homogenous

slurry. Drops of DI water are added until the proper viscosity is achieved. The slurry is cast with a doctor blade at 25 μm thickness onto Cu foil, which is first cleaned with isopropanol (IPA). The slurry is then allowed to ambiently dry, and the corners of the Cu foil are weighed down to prevent wrinkling. After ambient drying overnight, another glass casting sheet is placed over the slurry to sandwich the slurry between two casting sheets. This sandwich is then crimped together with binder clips and placed into the 80˚C oven overnight. Electrode discs with area of 0.71 cm^2 were punched out and assembled inside an Ar-filled glovebox into 2032 coin cells with 2 stainless steel spacers, a stainless steel spring, and a glass fiber separator. Polished Li foil was used as the counter and reference electrode. Commercial grade 1 M $LiPF_6$ in 1:1 ethylene carbonate (EC): dimethylene carbonate (DMC) was purchased from Sigma-Aldrich and used as the electrolyte. Cyclic voltammetry (CV) experiments were performed at 0.1 mV/s sweep rate from 1.5 V to 0.05 V. Galvanostatic cycling (GV) was performed at a C/5 current density from 2.0 V to 0.05 V. Potentiostatic electrochemical impedance spectroscopy (PEIS) measurements were taken in the frequency range from 900 kHz to 100 mHz with a 10 mV input. EIS data was taken at open-circuit voltage (OCV), which was approximately 1.5 to 2.0 V in the pristine state, in the fully lithiated state at 0.05V, and in the delithiated state at 2.0 V. A 15 minute potentiostatic hold at each state of charge was applied before each EIS measurement to ensure decay of residual current and equilibrium conditions. EIS Nyquist plots were fit to the equivalent circuit $R_1 + \frac{Q_2}{R_2} + Q_3$ in the ZFit module of EC-Lab software from Biologic.

5.2.5. Operando XRD**:** *Operando* diffraction experiments were conducted at Stanford Synchrotron Radiation Lightsource (SSRL). Pouch cells were made of aluminized mylar, Ni and Al leads, and

glass fiber separator. 1M $LiPF_6$ in EC:DMC was used as electrolyte. Li metal was used as counter and reference electrode. Pouch cells were pressurized using beryllium windows during operation. X-ray energy at SSRL beamline 11-3 was 12.7 keV (λ = 0.9763 Å). Exposure time to x-rays at SSRL ranged from 30 – 60 seconds. LaB_6 placed at the same sample-to-detector distance as the electrodes was used as calibration standard. Data integration and reduction was performed using GSAS-II.[30] Peak fitting was performed in Igor. Nanoporous and bulk SbSn were cycled at C/4 during *operando* XRD.

5.2.6. Operando PDF: *Operando* total scattering / pair distribution function (PDF) analysis experiments were conducted at the Advanced Photon Source (APS) beamline 11-ID-C. Samples were pressed into pellet electrodes with a composition of 60% active material, 20% carboxymethylcellulose (CMC) as binder, and 20% vulcan black. Pellet electrodes were loaded in AMPIX cells with glassy carbon windows to allow for conductivity and x-ray transparency.[31-32] Cells were constructed using Li metal as counter and reference electrode, glass fiber separator, and 1M $LiPF_6$ in EC:DMC as electrolyte. X-ray energy of 105.7 keV (λ = 0.1173 Å) was used. CeO_2 was used as a calibration standard. Exposure time to collect each pattern was approximately 5 minutes. Cycling in AMPIX cells was done galvanostatically at C/10. Scattering due to Li metal was masked away during 2D integration. Scattering due to electrolyte, separator, and glassy carbon was subtracted away to minimize interference in the G(r).

5.2.7. PDF Simulations: PDFgui was used to simulate reference phase PDF patterns and refine structural parameters of experimental PDF data. Refinements were carried out in the G(r) range of 0 – 18 Å. Values of Q_{damp} = 0.038 and Q_{braod} = 0.02 were used to correct for instrument broadening.

Crystal structure of SbSn alloy with tetragonal unit cell in space group P4/mmm (a = b = 3.075 Å, c = 6.259 Å, α = β = γ = 90˚) was obtained from the Materials Project Database (mp ID: 1218920).[33] Crystal structure of β-Sn formed during cycling was obtained from Materials Project Database (mp ID: 84, ICSD: 236667). Crystal structure of Li_3Sb was obtained from Materials Project Database (space group Fm3m, mp ID: 2074). Crystal structures for Li_2Sn_5 (mp ID: 7924) and Li_7Sn_3 (mp ID: 30768) were obtained from the Materials Project Database. Single phase scale factor refinements were also performed on Li_2Sb, LiSn, Li_5Sn_2, Li_7Sn_2, $Li_{13}Sn_5$, $Li_{17}Sn_4$, and $Li_{22}Sn_5$ to determine whether any other lithiated antimony or lithiated tin phases were formed in *operando*, but no evidence was found for the presence of these phases. Unit cell and bond distance visualizations were performed using VESTA.[34]

5.3 Results and Discussion.

5.3.1. Material Characterization.

From SEM images (**Figure 5.1**), we can see that the dealloying reaction produces particles with well-dispersed porosity with pores on the order of 30 nm in diameter. The porosity allows flexibility for volume expansion during cycling while maintaining an electrically connected network and enable better electrolyte penetration. EDS measurements show a 55:45 ratio of Sb:Sn in the product, which is within the intermetallic range.

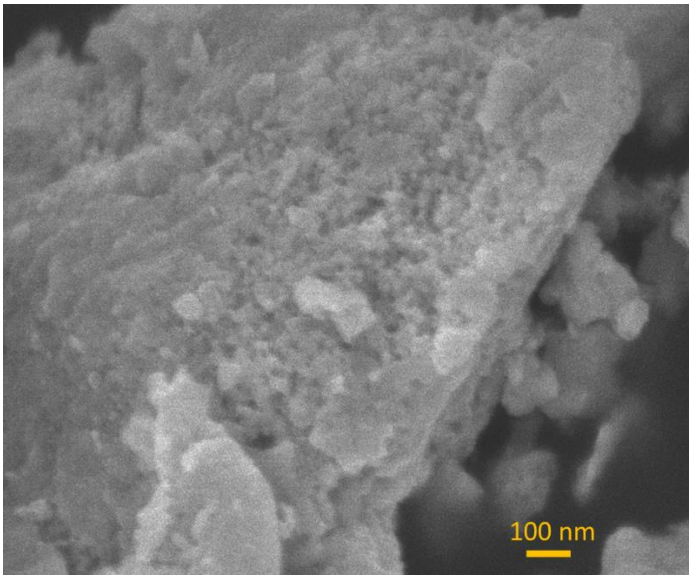

Figure 5.1. SEM image of nanoporous SbSn.

5.3.2. Electrochemical Characterization.

The bulk and nanoporous SbSn were fabricated into slurry electrodes for electrochemical testing. Cyclic voltammetry (CV) was performed at 0.1 mV/s sweep rate to identify the redox processes (**Figure 5.2a**). On the reduction scan, the peak at 0.78 V corresponds to the lithiation of Sb, and subsequent three peaks at 0.68, 0.52, and 0.40 V correspond to lithiation of the Sn. On the oxidation scan, delithiation of Sn occurs at 0.65, 0.74, and 0.80 V. Interestingly, the delithiation of Sb has split into two peaks at 1.04 and 1.08 V. However, by cycle 10, the first Sb delithiation peak has declined in intensity and all peaks appear broadened. This hysteresis observed in the CV suggests that lithiation and delithiation mechanisms are not the same. Galvanostatic cycling (GV) was also performed at C/5 (Figure 5.2b) to measure charge and discharge capacity. As expected, the lithiation GV shows four plateaus corresponding to the four reduction peaks in CV, and delithiation GV shows five plateaus corresponding to the five oxidation peaks in CV.

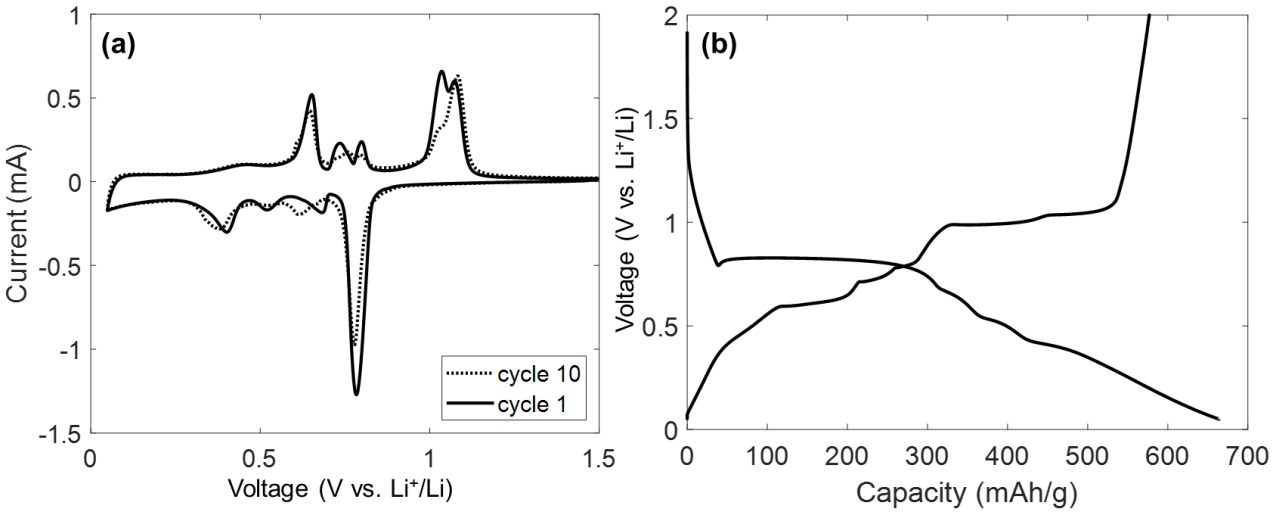

Figure 5.2 (a) CV of bulk SbSn during first and tenth cycle taken at 0.1 mV/s. (b) galvanostatic charge and discharge (GV) curves for bulk SbSn at C/5.

To measure the conductivity at different states of charge, electrochemical impedance spectroscopy (EIS) was performed (**Figure 5.3**) on bulk SbSn in the pristine state at open-circuit voltage (OCV), in the fully lithiated state at 0.05 V, and in the delithiated state 2.0 V. The EIS spectrum in the pristine state was fit to an equivalent circuit ($R_1 + \frac{Q_2}{R_2} + Q_3$) and the charge transfer resistance was determined to be 44 Ohm. In the fully lithiated state, we observe two semicircles, indicating that two distinct charge transfer processes are happening in the material. We attribute these two redox processes to charge transfer through the crystalline Li_3Sb and amorphous lithiated Sn product that are phase separated (see below discussion of *operando* XRD and PDF). Since the impedance shows two charge transfer events in fully lithiated state, the spectrum was fit to equivalent circuit ($R_1 + \frac{Q_2}{R_2} + \frac{Q_3}{R_3}$), and the two charge transfer resistances were calculated to be R_2 = 45 Ohm and R_3 = 82 Ohm. Interestingly, the delithiated state has the lowest charge transfer

resistance of 25 Ohm, although it contains significantly more amorphous material, suggesting that the delithiated material is well-mixed for uniform metallic conductivity.

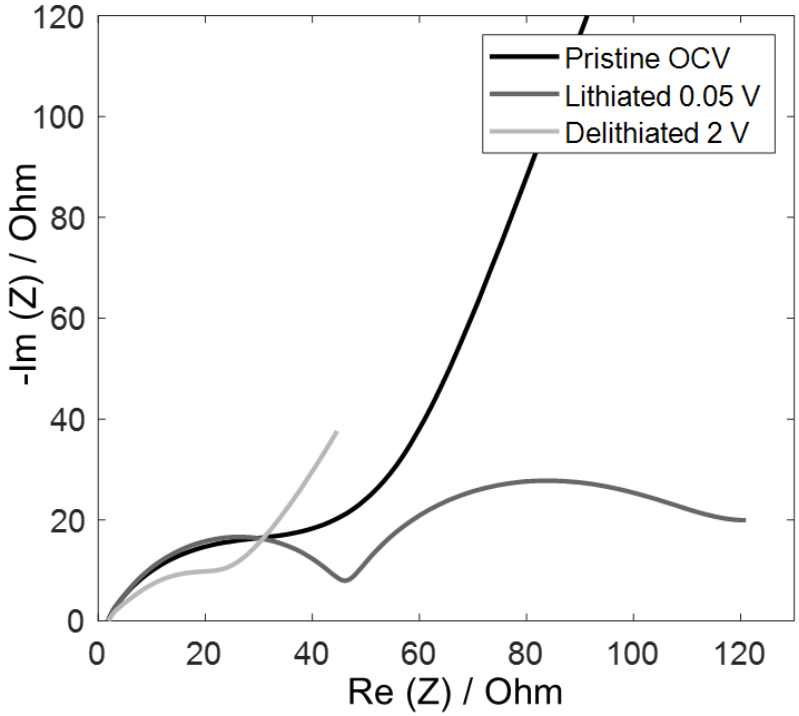

Figure 5.3. Nyquist plot of bulk SbSn EIS taken in the pristine, lithiated, and delithiated state.

5.3.3. *Operando* XRD.

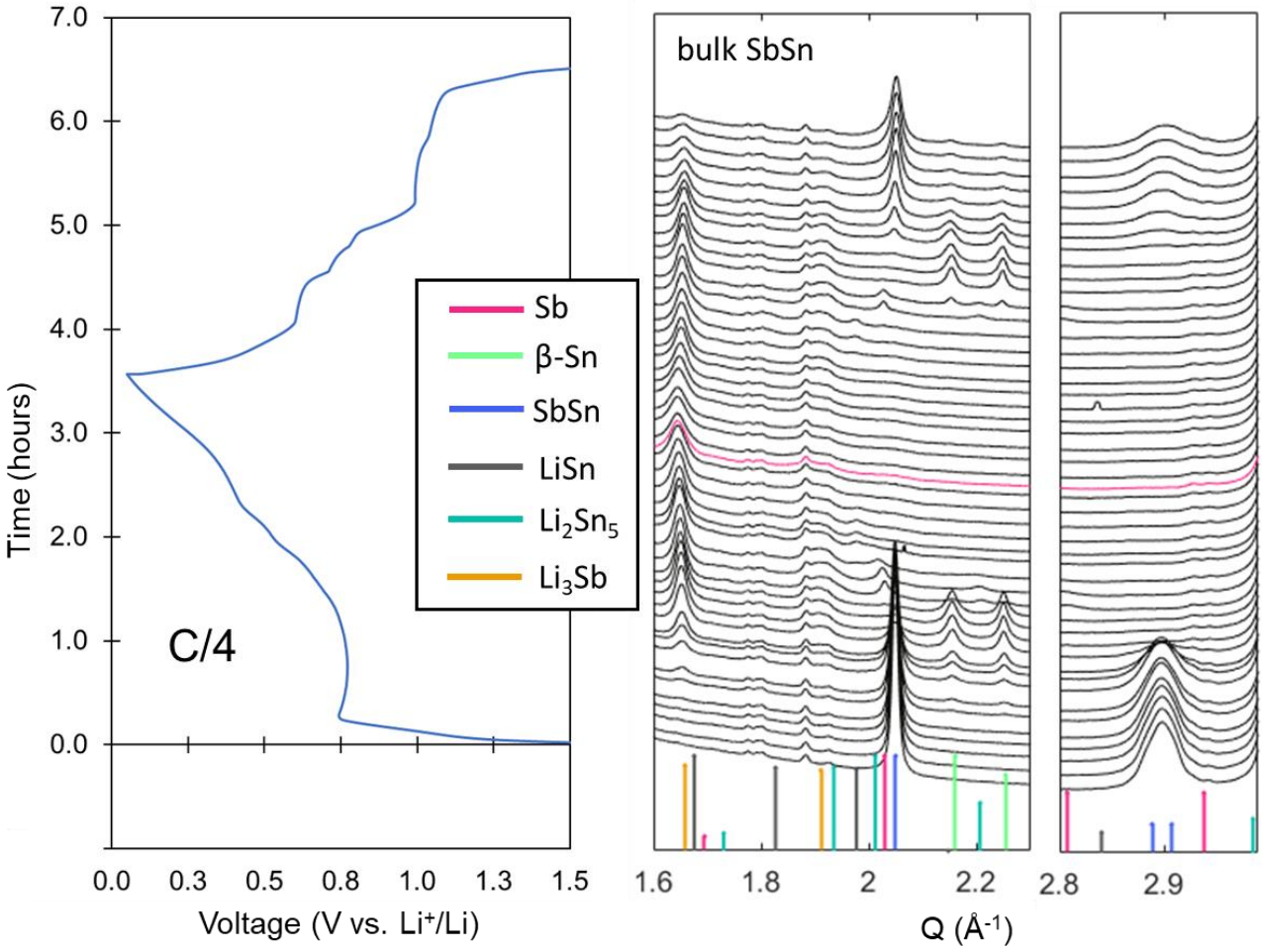

Figure 5.4. *Operando* XRD of bulk SbSn cycled with Li^+ at C/4. Reference pattern for Sb (pink) is shown to demonstrate that the material begins as a pure alloy with no phase separation of Sb and Sn. Reference pattern for LiSn (grey) is used to verify that no observable LiSn is formed in *operando*.

Bulk SbSn

The *operando* XRD (**Figure 5.4**) shows that the electrode material begins as a pure SbSn alloy with peaks at Q = 2.05, 2.89, and 2.91 $Å^{-1}$. No peaks for Sb are observed in the first scan,

indicating no phase separation of Sb or Sn. As the lithiation proceeds, the plateau at 0.8 V (vs. Li^+/Li) corresponds to the lithiation potential of Sb. This can be seen simultaneously with the appearance of Li_3Sb peaks at Q = 1.66 and 1.91 $Å^{-1}$, while the Sn phase separates out of the alloy, forming domains of β-Sn, showing peaks at Q = 2.16 and 2.25 $Å^{-1}$. After the initial appearance of the Li_3Sb peak at 1.66 $Å^{-1}$, the peak shifts to smaller Q (larger d-spacing) as lithiation continues. By fitting the peak positions to calculate d-spacing, we find that the Li_3Sb undergoes at 0.7% lattice expansion during insertion of Li^+. Once lithiation of Sb is complete, the lithiation of Sn begins at plateaus 0.6, 0.5, and 0.4 V. As Li^+ is inserted into Sn, the Sn metal peaks disappear. Some small peaks at Q = 1.94 and 2.01 $Å^{-1}$ appear that may correspond to a Li_2Sn_5 intermediate. As further lithiation proceeds, these peaks disappear, and no new peaks appear. Reference pattern for LiSn has been plotted (Figure 5.4, grey) to show this crystalline phase does not form. Other phases with higher stoichiometry of Li:Sn, such as Li_5Sn_2, $Li_{13}Sn_5$, Li_7Sn_2, and $Li_{22}Sn_5$, were also compared and no matching peaks were found. The lack of crystalline lithiated Sn phase peaks at the end of lithiation indicates that the highest lithiated Sn phase is amorphous. During de-lithiation, the reverse pathway is taken, as peaks for Li_2Sn_5 and β-Sn intermediates appear and disappear again. The SbSn alloy is reformed at the end of delithiation, but not to the same initial degree of crystallinity. Comparing peak areas of the SbSn peak at Q = 2.05 $Å^{-1}$ in first scan at OCV to the last scan at 1.5 V, 24% of the bulk SbSn alloy is recovered.

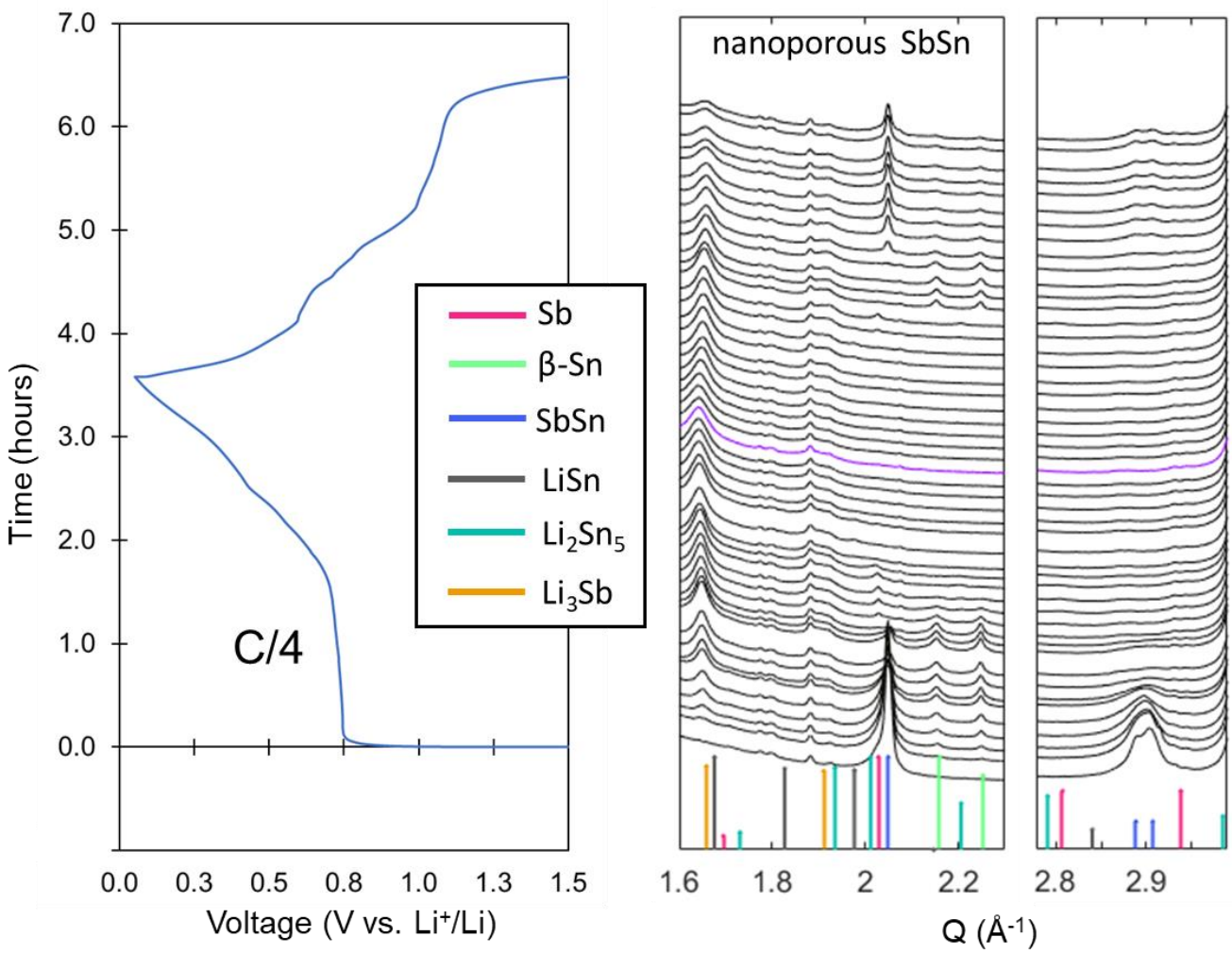

Figure 5.5. *Operando* XRD of nanoporous SbSn cycled with Li^+ at C/4. Reference pattern for Sb (pink) is shown to demonstrate that the material begins as a pure alloy with no phase separation of Sb and Sn. Reference pattern for LiSn (grey) is used to verify that no observable LiSn is formed in *operando*.

Nanoporous SbSn

The same phase evolution behavior is observed in the *operando* XRD of nanoporous SbSn (**Figure 5.5**). However, it can be noted that the Li_3Sb and β-Sn phases appear at an earlier time in

the nanoporous SbSn compared to the bulk SbSn. This suggests that lithiation of the Sb in the nanoporous alloy is more facile than in the bulk due to easier phase separation into nanoscale domains. The 1.66 $Å^{-1}$ peak of Li_3Sb also shifts to the left as lithiation proceeds, resulting in a 1% lattice spacing expansion. This value is larger than the 0.7% expansion that the Li_3Sb in bulk SbSn experiences, supporting the idea that the nanoporous architecture is able to accommodate more strain. The lithiation plateaus in the GV of nanoporous SbSn (Figure 5.5) are not as sharply defined as those observed in bulk , which is a commonly observed behavior for nanomaterials as the distribution of redox potentials is broadened and the material can accommodate more strain. Comparing peak areas of the SbSn peak at Q = 2.05 $Å^{-1}$ in first scan at OCV to the last scan at 1.5 V, 11% of the nanoporous SbSn alloy is recovered. Therefore, more of the bulk SbSn is able to re-alloy after de-lithiation than in the nanoporous material. The Li_3Sb peak at 1.66 $Å^{-1}$ has not completely disappeared in the last scan, indicating some Sb has not been fully delithiated.

Again, no peaks corresponding to lithiated Sn phases appear at the end of lithiation, demonstrating that the fully lithiated Sn is amorphous. This discovery is notable since several crystalline lithiated Sn phases have been reported, including Li_2Sn_5, LiSn, Li_7Sn_3, Li_5Sn_2, $Li_{13}Sn_5$, Li_7Sn_2, $Li_{17}Sn_4$, and $Li_{22}Sn_5$.[35] An *operando* XRD study by Frerichs *et al*. showed that lithiation of Sn nanoparticle-based electrodes results in the formation of crystalline Li_2Sn_5 and LiSn phases. [36] However, our operando XRD on the SbSn intermetallic only shows evidence for Li_2Sn_5 phase, suggesting that the crystallization of higher Li-content Sn phases is frustrated by the presence of the surrounding Li_3Sb matrix.

5.3.4. *Operando* PDF.

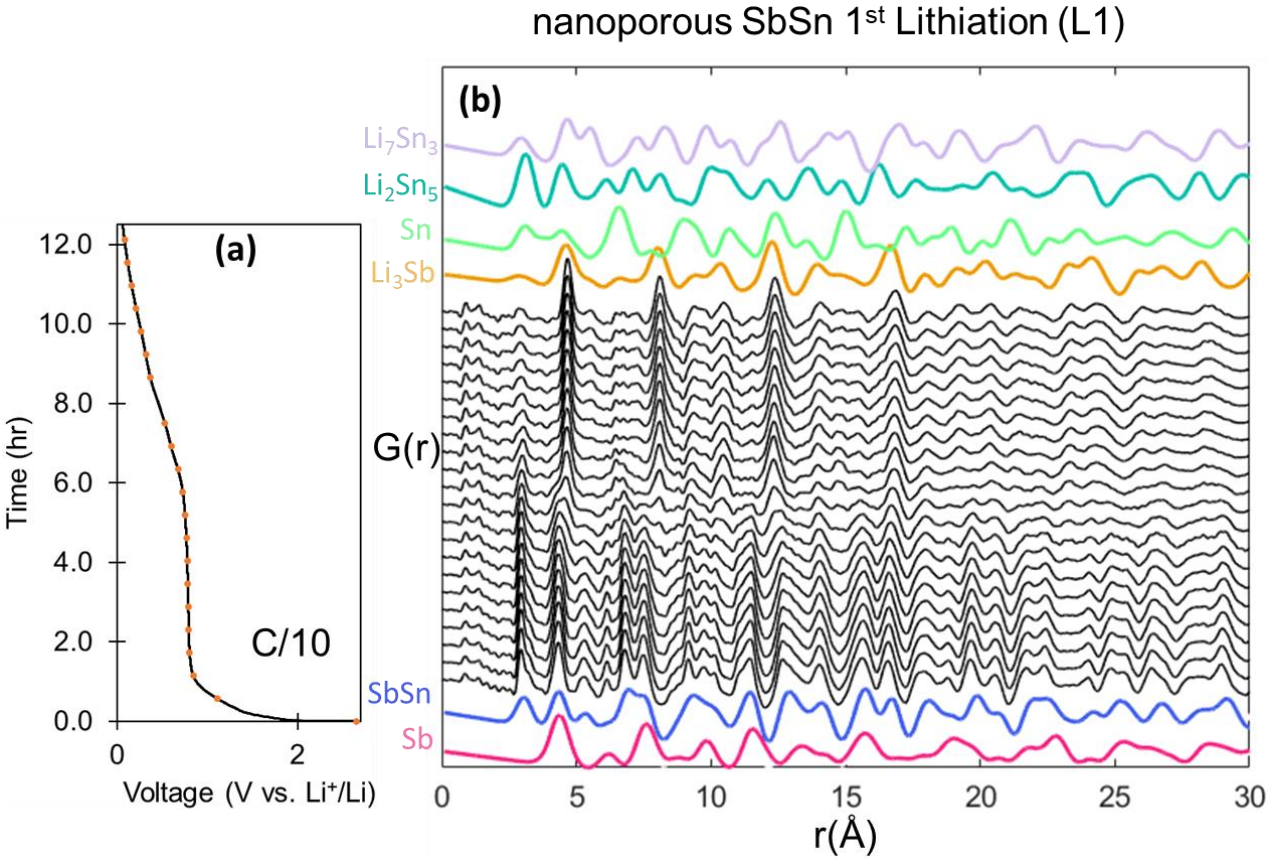

Figure 5.6. *Operando* PDF of nanoporous SbSn cycled with Li^+ at C/10. (a) First lithiation GV curve and (b) normalized operando PDF during first lithiation with simulated reference PDF patterns for Sb, SbSn, Li_3Sb, β-Sn, Li_2Sn_5, and Li_7Sn_3. Orange dots indicate voltages where PDF scans were taken.

The significant amount of amorphous material formed during cycling of SbSn makes unequivocal phase identification by XRD challenging. In particular, the nanoporous SbSn is only able to recover 11% of the original alloy. Therefore, we turn to *operando* PDF to give complementary structural information about the amorphous phases formed during cycling. The first scan matches well with the PDF pattern of SbSn alloy (**Figure 5.6b**), as expected. In the

reference pattern for SbSn, the first peak at r = 3.06 Å corresponds to a nearest neighbor Sb-Sn bond length assuming that the alloy is perfectly uniform and all Sb-Sn bonds are equal length. The relative contribution of Sn-Sb compared to Sb-Sb (or Sn-Sn) contributions to each PDF peak can be decomposed in the simulation (**Figure 5.7**). In the experimental data, the sharp peak at 2.95 Å and shoulder at 3.24 Å in the first scan suggests that the alloy is not atomically uniform and there are two distributions of nearest neighbor bonds, likely a result of annealing conditions during synthesis. In the middle of the PDF series, and at the end of 0.8 V plateau, we can see the loss of crystallinity and long-range order as the PDF peaks at r > 20 Å disappear. For the sake of discussion, we consider r = 0 – 18 Å as "short-range" and r > 20 Å as "long-range". At the end of the 0.8 V plateau (Figure 5.6a), the short-range peaks corresponding to SbSn disappear and peaks resembling Li_3Sb (orange) appear at r = 4.65, 8.09, 12.33, and 16.8 Å. As the lithiation of Sb is completed, the crystallinity is restored, as peaks appear again at r > 20 Å corresponding to Li_3Sb. These observations are consistent with the *operando* XRD (Figure 5.5), as Li_3Sb peaks appear towards the end of the 0.8 V plateau. Furthermore, as lithiation of the Sn proceeds (after 0.8 V plateau and after 6 hrs), the long-range PDF does not change at all, indicating that no new crystalline phases are being formed. Again, this data is consistent with the *operando* XRD which does not show any new peaks forming during lithiation of Sn, confirming that the lithiated Sn is amorphous. Because PDF gives all atom-atom correlations within the materials, the bonds in the amorphous lithiated Sn phase can still be identified to give some picture of structure. Specifically, a peak at 5.54 Å begins to grow during lithiation of Sn (Figure 5.6b).

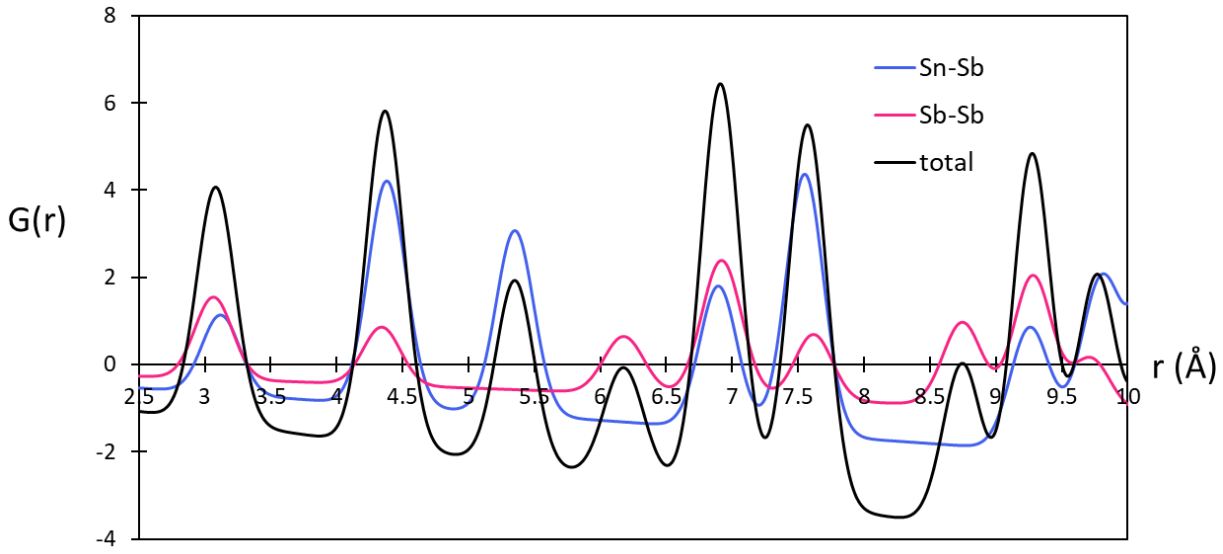

Figure 5.7. Simulated PDF for SbSn alloy (black) with partial PDF from Sn-Sb correlation contributions (blue) and Sb-Sb contributions (pink).

As the appearance and disappearance of several phases overlap in time, it becomes difficult to assign peaks in the PDF to distinct phases. Therefore, we have carried out multi-phase refinement on the scale factor of G(r) using PDFgui to quantify amounts of each phase during cycling (**Figure 5.8**). Based on the *operando* XRD, the presence of crystalline phases of SbSn, β-Sn metal, and Li_3Sb has been established. This is also confirmed in the multi-phase refinement of the PDF patterns. The active material begins as 80% SbSn alloy which decreases as lithiation proceeds. β-Sn is formed as an intermediate as the Li_3Sb phase separates out, but is consumed as Sn starts to lithiate. We also include additional phases of Li_2Sn_5 and Li_7Sn_3 to determine if the local structure of lithiated Sn formed in *operando* resembles any of these phases. The presence of Li_2Sn_5 as an intermediate, which was suggested by *operando* XRD but unclear due to low signal, is confirmed by multi-phase fitting of the PDF. Interestingly, as the Li_2Sn_5 intermediate breaks down and disappears, an amorphous phase resembling Li_7Sn_3 appears and persists to the end of

lithiation. Refinements were also performed on Li_2Sb, LiSn (Li:Sn ratio 1:1), Li_5Sn_2 (Li:Sn 2.5:1), Li_7Sn_2 (Li:Sn 3.5:1), $Li_{13}Sn_5$ (Li:Sn 2.6:1), $Li_{17}Sn_4$ (4.25:1), and $Li_{22}Sn_5$ (Li:Sn 4.4:1) to determine whether any other lithiated antimony or lithiated tin phases were formed in *operando*, but no evidence was found for the presence of these phases (see Appendix B). Therefore, we have confirmed that the highest extent of lithiation of Sn is Li_7Sn_3 or Li:Sn ratio of 2.33:1. The formation of an amorphous lithiated Sn phase resembling Li_7Sn_3 in short-range ordering has been suggested with in *operando* solid state NMR on Sn nanoparticles.

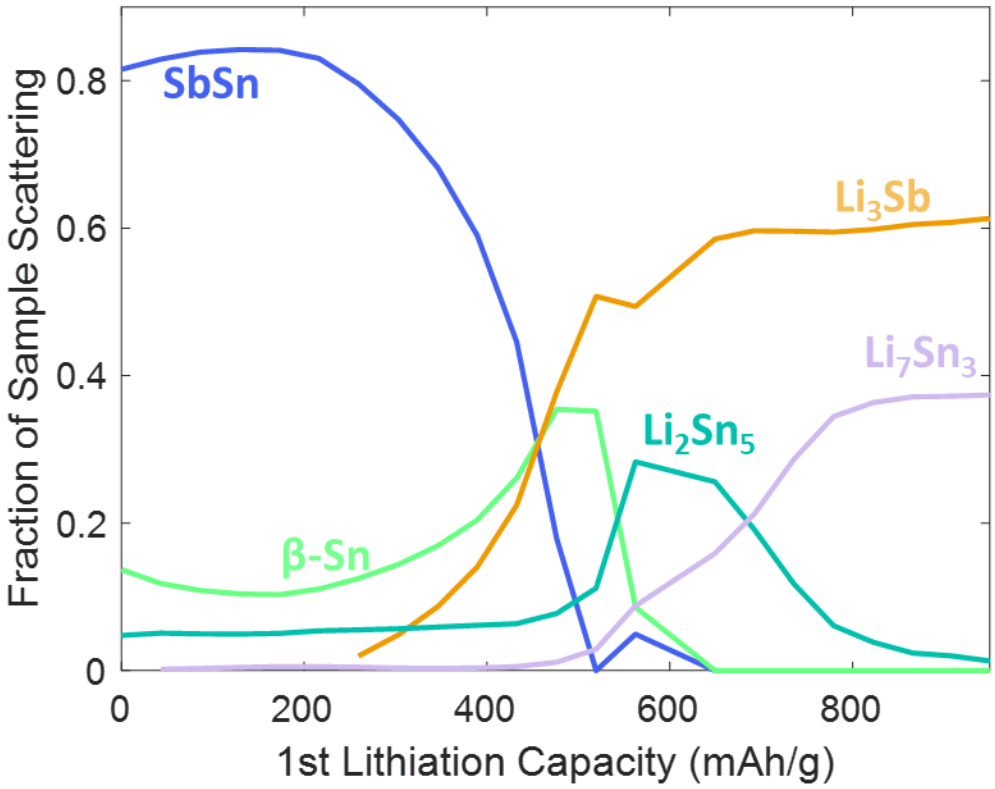

Figure 5.8. Multi-phase refinement of the 1st lithiation *operando* PDF of nanoporous SbSn. Fraction is calculated from the fraction of each phase of total refined scale factors.

Interestingly, in pure Sn electrodes, several more crystalline lithiated tin phases are formed as intermediates during cycling. In contrast, we never observe any crystalline lithiated tin phases formed during cycling in our SbSn intermetallic. This frustration of the crystallization of lithiated tin phases may be due to the fact that the β-Sn formed after lithiation of Sb is in dispersed nanocrystalline domains embedded in a Li_3Sb matrix. We postulate that the amorphous nature of the lithiated Sn phases provides further stabilization of volume expansion as the amorphous material is more ductile, resulting in more stable electrochemical performance.

Looking at the PDF during delithiation (**Figure 5.9**), it is evident that the evolution of local structure is not merely the reverse of the lithiation scan. As expected, the first delithiation PDF pattern most closely resembles Li_3Sb reference pattern, with some contribution from Li_7Sn_3 peak at 5.58 Å. At the end of delithiation (Figure 5.9b), the correlations in the region from 20 – 30 Å are very weak, confirming that much of the material is amorphous, without long-range order. In the short range from 2 – 15 Å, the delithiation product closely resembles the reference pattern for SbSn. However, it can be noted that there is a sharp peak at 2.98 Å, whose shape looks different from the initial SbSn alloy PDF (Figure 5.6b). Allan *et al.* have observed a very similar amorphous phase in *operando* PDF studies of Na^+ intercalation into pure Sb.[26] They attribute the new sharp peak at 2.9 Å to a Sb-Sb dumbbell-like dimer bonding motif.[26] The peak at 4.44 Å also appears to be two closely overlapping peaks, likely corresponding to SbSn and Sb, suggesting some degree of phase separation of the amorphous material formed at the end of delithiation.

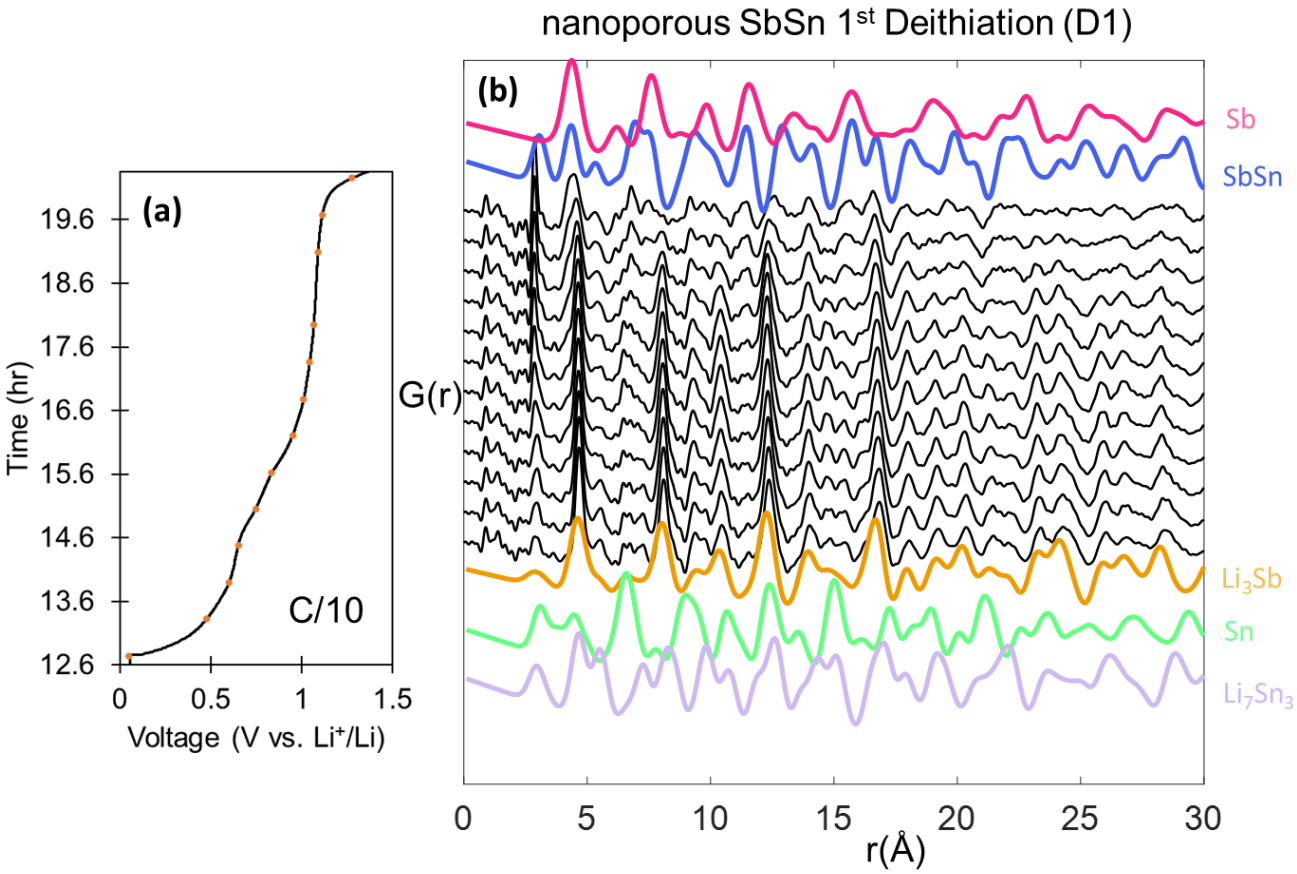

Figure 5.9. *Operando* PDF of nanoporous SbSn cycled with Li^+ at C/10. (a) First delithiation GV curve and (b) normalized operando PDF during first delithiation with simulated reference PDF patterns for Sb, SbSn, Li_3Sb, β-Sn, and Li_7Sn_3. Orange dots indicate voltages where PDF scans were taken.

Again, by performing a multi-phase refinement with Li_3Sb, Li_7Sn_3, Sb, SbSn, and β-Sn (**Figure 5.10**), we can estimate the percentage of each phase throughout the delithiation process. Although Li_2Sn_5 was observed in the operando XRD and lithiation operando PDF, it was not included in the delithiation PDF multi-phase refinment due to the restriction in PDFgui of allowing a maximum of 5 phases. These 5 phases were chosen because they gave the lowest error through

the multi-phase refinment. As expected, the material begins primarily as Li_3Sb and Li_7Sn_3, which decline in intensity as delithiation proceeds. Some β-Sn appears as an intermediate as Li_xSn gets delithiated first. We see the reappearance and growth of SbSn alloy phase to about 45% at the end of delithiation, and the reappearance of Sb. From the *operando* XRD peak area (Figure 5.5), we recall that about 11% of the crystalline nanoporous SbSn is recovered. While the 45% SbSn calcualted from *operando* PDF is a mixture of both crystalline and amoprhous SbSn, the PDF signal due to Sb and β-Sn at the end of delithiation must be amorphous material.

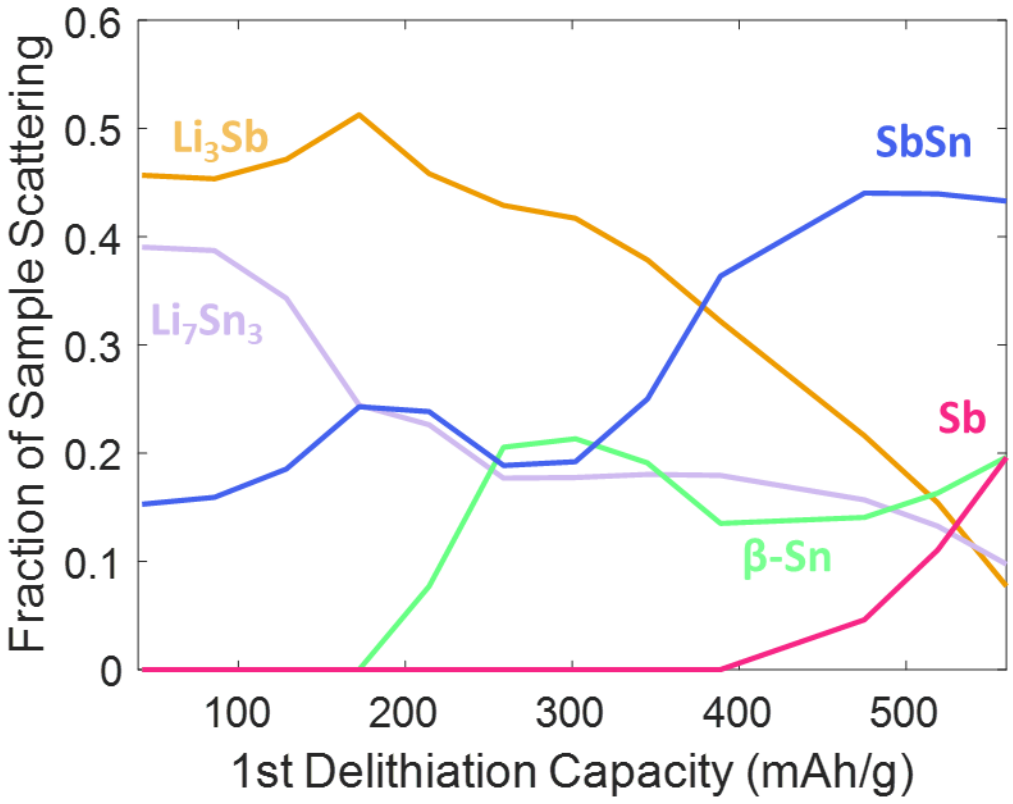

Figure 5.10. Multi-phase refinement of the 1st delithiation during *operando* PDF of nanoporous SbSn. Fraction is calculated from the fraction of each phase of total refined scale factors.

5.4 Conclusions.

We have demonstrated the synthesis and characterization of a nanoporous SbSn alloying anode material. The nanoporous architecture promotes volume expansion into the pores, mitigating crack formation and long-term capacity fade. *Operando* XRD on both nanoporous and bulk SbSn systems clearly shows phase separation, and the formation of Li_3Sb, β-Sn, and Li_2Sn_5 intermediates, and an amorphous lithiated Sn final product. The nanoporous architecture is shown to promote faster lithiation of the Sb and easier phase separation of the alloy. Upon delithiation, bulk SbSn is able to recover 24% of the original crystalline alloy, while nanoporous SbSn recovers only 11% of the original crystalline alloy. Therefore, we employ *operando* PDF as a complementary structural probe to characterize the local structure of the amorphous phase. We discover that lithiation of the Sn goes through Li_2Sn_5 intermediate to reach a final amorphous product that resembles the Li_7Sn_3 phase. The nanoporous intermetallic structure prevents formation of crystalline lithiated Sn phases, buffering the volume expansion and enabling better cycling stability.

5.5 References.

[1] Blomgren, G. E. The Development and Future of Lithium Ion Batteries. *Journal of The Electrochemical Society*. **2017**, 164, A5019.

[2] Whittingham, M. Stanley. "Lithium Batteries and Cathode Materials." *Chemical Reviews*, **2004**, 104, 4271 – 4301.

[3] Winter, M.; Brodd, R. "What Are Batteries, Fuel Cells, and Supercapacitors?" *Chemical Reviews*, **2004**, 104, 4245 – 4269.

[4] https://energystorageforum.com/energy-storage-technologies/smart-grid-energy-storage-systems

[5] Dedes, I.-C.; Tsampasis, E.; Elias, C.; Gkonis, P. "Energy Storage in Smart Electrical Grids." 10th Mediterranean Conference on Embedded Computing (MECO), 2021, p. 1 – 4. doi: 10.1109/MECO52532.2021.9460169.

[6] Goodenough, J.B.; Kim, Y. "Challenges for Rechargeable Li Batteries." *Chemistry of Materials*, **2010**, 22, 587 – 603.

[7] Moyassari, E.; Roth, T.; Kucher, S.; Chang, C.-C.; Hou, S.-C.; Spingler, F.B.; Jossen, A. "The Role of Silicon in Silicon-Graphite Composite Electrodes Regarding Specific Capacity, Cycle Stability, and Expansion." *Journal of The Electrochemical Society*, **2022**, 169, 010504.

[8] An, S.J.; Li, J.; Daniel, C.; Mohanty, D.; Nagpure, S.; Wood, D.L.W. "The state of understanding of the lithium-ion-battery graphite solid electrolyte interphase (SEI) and its relationship to formation cycling." *Carbon*, **2016**, 105, 52 – 76.

[9] Waldmann, T.; Kasper, M.; Wohlfahrt-Mehrens, M. "Optimization of Charging Strategy by Prevention of Lithium Deposition on Anodes in high-energy Lithium-ion Batteries – Electrochemical Experiments." *Electrochimica Acta*, **2015**, 178, 525 – 532.

[10] Obrovac, M.N., et al. Alloy Negative Electrodes for Li-Ion Batteries. *Chem. Rev.* **2014**, 114, 11444 – 11502.

[11] Park, C.-M., et al. Li-alloy based anode materials for Li secondary batteries. *Chem. Soc. Rev.* **2010**, 39, 3115 – 3141.

[12] Xie, H.; Kalisvaart, W.P.; Olsen, B.C.; Luber, E.J.; Mitlin, D.; Buriak, J.M. "Sn-Bi-Sb alloys as anode materials for sodium ion batteries." *Journal of Materials Chemistry A*, **2017**, 5, 9661 – 9670.

[13] Zhao, Y.; Manthiram, A. "High-Capacity, High-Rate Bi-Sb Alloy Anodes for Lithium-Ion and Sodium-Ion Batteries." *Chemistry of Materials*, **2015**, 27, 3096 – 3101.

[14] Augustyn, V., et al. High-rate electrochemical energy storage through Li^+ intercalation pseudocapacitance. *Nature Materials.* **2013**, 12, 518 – 522.

[15] Cook, J.B.; Lin, T.C.; Detsi, E.; Weker, J.N.; Tolbert, S.H. "Using X-ray Microscopy to Understand How Nanoporous Materials Can Be Used to Reduce the Large Volume Change in Alloy Anodes." *Nano Letters*, **2017**, 17, 870 – 877.

[16] Cook, J.B.; Detsi, E.; Liu, Y.; Liang, Y.-L.; Kim, H.-S.; Petrissans, X.; Dunn, B.; Tolbert, S.H. "Nanoporous Tin with a Granular Hierarchical Ligament Morphology as a Highly Stable Li-Ion Battery Anode." *ACS Applied Materials & Interfaces*, **2017**, 9, 293 – 303.

[17] Detsi, E.; Petrissans, X.; Yan, Y.; Cook, J.B.; Deng, Z.; Liang, Y.-L.; Dunn, B.; Tolbert, S.H. "Tuning ligament shape in dealloyed nanoporous tin and the impact of nanoscale morphology on its applications in Na-ion alloy battery anodes." *Physical Review Materials*, **2018**, 2, 055404.

[18] Cook, J.B., et al. Suppression of Electrochemically Driven Phase Transitions in Nanostructure MoS_2 Pseudocapacitors Probed Using Operando X-ray Diffraction. *ACS Nano.* **2019**, 13, 1223 – 1231.

[19] Ruiz, O.; Cochrane, M.; Li, M.; Yan, Y.; Ma, K.; Fu, J.; Wang, Z.; Tolbert, S.H.; Shenoy, V.B.; Detsi, E. "Enhanced Cycling Stability of Macroporous Bulk Antimony-Based Sodium-Ion Battery Anodes Enabled through Active/Inactive Composites." *Advanced Energy Materials*, **2018**, 8, 1801781.

[20] Courtney, I.A.; Dahn, J.R. "Electrochemical and In Situ X-Ray Diffraction Studies of the Reaction of Lithium with Tin Oxide Composites." *Journal of The Electrochemical Society*, **1997**, 144, 2045.

[21] Hwang, S.; Yao, Z.; Zhang, L.; Fu, M.; He, K.; Mai, L.; Wolverton, C.; Su, D. "Multistep Lithiation of Tin Sulfide: An Investigation Using in Situ Electron Microscopy." *ACS Nano*, **2018**, 12, 3638 – 3645.

[22] Xu, H.; Li, S.; Zhang, C.; Chen, X.; Liu, W.; Zheng, Y.; Xie, Y.; Huang, Y.; Li, J. "Roll-to-roll prelithiation of Sn foil anode suppresses gassing and enables stable full-cell cycling of lithium-ion batteries." *Energy & Environmental Science*, **2019**, 12, 2991 – 3000.

[23] Farrow, C.L.; Juhas, P.; Liu, J.W.; Bryndin, D.; Bozin, E.S.; Block. J.; Proffen, Th.; and S.J.L. Billinge. "PDFfit2 and PDFgui: computer programs for studying nanostructure in crystals." *J. Phys.: Condens. Mat.*, **2007**, 19, 335219.

[24] Egami, T. and Billinge, S.J.L. *Underneath the Bragg Peaks: Structural Analysis of Complex Materials*; Pergamon, 2003.

[25] Jeong, I.-K.; Proffen, T.; Mahiuddin-Jacobs, F.; Billinge, S.J.L. "Measuring Correlated Atomic Motion Using X-ray Diffraction." *Journal of Physical Chemistry A*, **1999**, 103, 921 – 924.

[26] Allan, P.K.; Griffin, J.M.; Darwiche, A.; Borkiewicz, O.J.; Wiaderek, K.M.; Chapman, K.W.; Morris, A.J.; Chupas, P.J.; Monconduit, L.; Grey, C.P. "Tracking Sodium-Antimonide Phase Transformations in Sodium-Ion Anodes: Insights from Operando Pair Distribution Function Analysis and Solid-State NMR Spectroscopy." *JACS*, **2016**, 138, 2352 – 2365.

[27] Wang, X.; Tan, S.; Yang, X.-Q.; Hu, E. "Pair distribution function analysis: Fundamentals and application to battery materials." *Chinese Physics B*, **2020**, 29, 028802.

[28] Chapman, K.W. "Emerging *operando* and x-ray pair distribution function methods for energy materials development." *MRS Bulletin*, **2016**, 41, 231 – 238.

[29] Billinge, Simon J.L. "The rise of the X-ray atomic pair distribution function method: a series of fortunate events." *Phil. Trans. R. Soc. A.*, **2019**, 377:20180413.

[30] Toby, B.H. and R.B. Von Dreele. "GSAS-II: the genesis of a modern open-source all purpose crystallography software package." *Journal of Applied Crystallography*, **2013**, 46, 544 – 549.

[31] Borkiewicz, O.J.; Shyam, B.; Wiaderek, K.M.; Kurtz, C.; Chupas, P.J.; Chapman, K.W. "The AMPIX electrochemical cell: a versatile apparatus for in situ X-ray scattering and spectroscopic measurements." *Journal of Applied Crystallography*, **2012**, 45, 1261 – 1269.

[32] Borkiewicz, O.J.; Wiaderek, K.M.; Chupas, P.J.; Chapman, K.W. "Best Practices for Operando Battery Experiments: Influences of X-ray Experiment Design on Observed Electrochemical Reactivity." *Journal of Physical Chemistry Letters*, **2015**, 6, 2081 – 2085.

[33] Jain, A.; Ong, S.P.; Hautier, G.; Chen, W.; Richards, W.D.; Dacek, S.; Cholia, S.; Gunter, D.; Skinner, D.; Ceder, G.; Persson, K.A. "Commentary: The Materials Project: A materials genome approach to accelerating materials innovation." *APL Materials*, **2013**, 1, 011002.

[34] Momma, K.; Izumi, F. "VESTA 3 for three-dimensional visualization of crystal, volumetric and morphology data." *Journal of Applied Crystallography*, **2011**, 44, 1272 – 1276.

[35] Berger, P.; Flandorfer, H. "Sb-Sn alloy anodes for Li-ion batteries: The ternary system Li-Sb-Sn." *Journal of Alloys and Compounds*, **2021**, 855, 157381.

[36] Frerichs, J.; Ruttert, M.; Bockmann, S.; Winter, M.; Placke, T.; and M. R. Hansen. "Identification of Li_xSn Phase Transitions During Lithiation of Tin Nanoparticle-Based Negative Electrodes from Ex Situ ^{119}Sn MAS and Operando ^{7}Li NMR and XRD." *ACS Applied Energy Materials*, **2021**, 4, 7278 – 7287.

CHAPTER 6: Conclusions.

We investigated a variety of nanostructured energy storage materials, ranging from pseudocapacitive cathode and anode materials, to alloying anode materials. We have synthesized spinel $LiMn_2O_4$ (LMO) cathode as a nanoporous architecture through a PMMA colloid-templated sol-gel method, enables high-rate capability up to 20C. By Al-doping the surface of nanoporous LMO, we are able to significantly mitigate the self-discharge problem related to Mn(III) surface dissolution, while still maintaining high rate capability. Our method offers a simple and scalable way to produce a pseudocapacitive cathode material, which can be paired with many anode materials to obtain a pseudocapacitive full cell.

In mesoporous MoS_2, we have achieved synthetic control over both crystal size and crystallinity to produce a matrix of samples in order to de-convolute the interplay of size and disorder as design principles to induce pseudocapacitance. Mesoporous MoS_2 was synthesized through a gas-phase sulfurization reaction on precursor mesoporous MoO_2, produced through PMMA colloid-templating. Size control is obtained by varying the PMMA template size, and subsequent crystal size, of the mesoporous MoO_2 precursor. Disorder is controlled by annealing at different temperatures, with 700˚C producing the most disordered and 900˚C producing the most crystalline material. From ambient powder total scattering (TS) / pair distribution function (PDF) measurements paired with simulation, we demonstrate that disorder in MoS_2 takes the form of both stacking faults and vdW layer expansion and quantitate their relative contributions. *Operando* XRD shows that the first-order Li^+ intercalation-induced phase transition from 1T-MoS_2 to triclinic Li_xMoS_2 is suppressed by both reducing crystal size and introducing lattice disorder.

APPENDIX A: Detailed Procedure for PDF Multi-Phase Refinement and Discussion of Other Phases Investigated for *Operando* PDF of MoS_2

Before performing multi-phase refinement, a single-phase refinement was performed on the first pattern of pre-cycled bulk MoS_2 at the beginning of lithiation (2.7 V) to obtain a refined structure for both 2H and 1T-MoS_2 since the material should largely be in the 1T structure, but a mixture of 2H and 1T may exist due to some back-conversion. Similarly, a single-phase refinement was performed on the last pattern of bulk MoS_2 at the end of lithiation to obtain a refined structure triclinic Li_xMoS_2 since the material should predominantly be in this structure at the end of lithiation (1.0 V). Details about these refined crystal structures are given in tables below.

Table A1: Parameters to define crystal structure of refined 1T phase.

a	**b**	**c**	**α**	**β**	**γ**	**Scale factor**	**Delta1**			
3.17604	3.17604	6.25301	90.0	90.0	120.0	0.126279	2.30688			
elem	**x**	**y**	**z**	**u11**	**u22**	**u33**	**u12**	**u13**	**u23**	**occ**
Mo	0.0	0.0	0.0	0.04208	0.04208	0.031	0.02104	0.0	0.0	1.0
S	0.3333	0.6667	0.2559	0.02	0.02	0.065	0.0099	0.0	0.0	1.0
S	0.3333	0.6666	0.2559	0.02	0.02	0.065	0.0101	0.0	0.0	1.0
S	0.3334	0.6667	0.2559	0.02	0.02	0.065	0.0101	0.0	0.0	1.0
S	0.6667	0.3333	0.7441	0.0202	0.02	0.065	0.0099	0.0	0.0	1.0
S	0.6666	0.3333	0.7441	0.0202	0.02	0.065	0.0101	0.0	0.0	1.0
S	0.6667	0.3334	0.7441	0.0202	0.02	0.065	0.0101	0.0	0.0	1.0

Table A2: Parameters to define crystal structure of refined 2H phase.

a	b	c	α	β	γ	Scale factor	Delta1			
3.18365	3.18365	12.8779	90.0	90.0	120.0	0.198753	2.05526			
elem	**x**	**y**	**z**	**u11**	**u22**	**u33**	**u12**	**u13**	**u23**	**occ**
Mo	0.33333	0.66666	0.25	0.0079395	0.0079395	0.033641	0.0	0.0	0.0	0.995
Mo	0.66666	0.33333	0.75	0.0079395	0.0079395	0.033641	0.0	0.0	0.0	0.995
S	0.33333	0.66666	0.627	0.01	0.01	0.01	0.0	0.0	0.0	1.0
S	0.66666	0.33333	0.127	0.01	0.01	0.01	0.0	0.0	0.0	1.0
S	0.33333	0.66666	0.872	0.01	0.01	0.01	0.0	0.0	0.0	1.0
S	0.66666	0.33333	0.3725	0.01	0.01	0.01	0.0	0.0	0.0	1.0
Mo	0.33333	0.66666	0.25	0.0079395	0.0079395	0.033641	0.0	0.0	0.0	0.995
Mo	0.66666	0.33333	0.75	0.0079395	0.0079395	0.033641	0.0	0.0	0.0	0.995

Table A3: Parameters to define crystal structure of refined triclinic $LiMoS_2$ phase.

a	b	c	α	β	γ	Scale factor	Delta1			
6.22053	6.65533	6.69788	61.9115	91.8628	91.0543	0.188591	0.0			
elem	**x**	**y**	**z**	**u11**	**u22**	**u33**	**u12**	**u13**	**u23**	**occ**
Li	0.00994	0.481909	0.290165	0.001	0.001	0.001	0.001	0.001	0.001	1.0
Li	0.99006	0.518091	0.709835	0.001	0.001	0.001	0.001	0.001	0.001	1.0
Li	0.979104	0.009214	0.739919	0.001	0.001	0.001	0.001	0.001	0.001	1.0

Li	0.020896	0.990786	0.260081	0.001	0.001	0.001	0.001	0.001	0.001	1.0
Mo	0.500255	0.491742	0.210233	0.001	0.001	0.001	0.001	0.001	0.001	1.0
Mo	0.499745	0.508258	0.789767	0.001	0.001	0.001	0.001	0.001	0.001	1.0
Mo	0.49609	0.943019	0.807797	0.001	0.001	0.001	0.001	0.001	0.001	1.0
Mo	0.50391	0.056981	0.192203	0.001	0.001	0.001	0.001	0.001	0.001	1.0
S	0.773248	0.344861	0.068566	0.001	0.001	0.001	0.001	0.001	0.001	1.0
S	0.226752	0.655139	0.931434	0.001	0.001	0.001	0.001	0.001	0.001	1.0
S	0.746448	0.817849	0.104764	0.001	0.001	0.001	0.001	0.001	0.001	1.0
S	0.253552	0.182151	0.895236	0.001	0.001	0.001	0.001	0.001	0.001	1.0
S	0.698337	0.322222	0.59074	0.001	0.001	0.001	0.001	0.001	0.001	1.0
S	0.301663	0.677778	0.40926	0.001	0.001	0.001	0.001	0.001	0.001	1.0
S	0.718371	0.847862	0.568865	0.001	0.001	0.001	0.001	0.001	0.001	1.0
S	0.281629	0.152138	0.431135	0.001	0.001	0.001	0.001	0.001	0.001	1.0

Often crystal structures do not come with thermal displacement parameters (u11, u22, u33, u12, u13, u23), so the isotropic thermal parameters (u11, u22, u33) were given an initial value of 0.001 to begin refinement. Parameters for each phase were relaxed and refined in sequential steps starting with a) lattice constants, b) scale factor, c) delta1, d) isotropic thermal displacement parameters (u11, u22, u33), and e) occupancy numbers. After reaching a minimum goodness of fit, R_w, delta1 was fixed at optimized value. Delta1 and delta2 are highly correlated and should not be simultaneously relaxed. Relaxing atomic positions (x,y,z) or anisotropic thermal displacement parameters (u12, u13, u23) usually resulted in irreversibly poor fits, so they were left at initial values.

Once the three optimized structures for 2H, 1T, and triclinic phases were obtained, they input as possible phases for each refinement of experimental PDF scan. During multi-phase refinement, only the scale factor of each phase was relaxed. Several refinement procedures relaxing scale factors and lattice parameters during multi-phase refinement were tested but relaxing too many correlated parameters resulted in refinement instability. Multi-phase refinement results, including goodness of fit (R_w), are shown for each sample in tables below.

Table A4: Precycled Bulk MoS_2 Multi-Phase Scale Factor Refinement Results.

Voltage (V)	**2H**	**1T**	**triclinic**	**R_w**
2.475	0.2402	0.052444	0.022709	0.409297
2.133	0.239562	0.049033	0.030266	0.419201
1.862	0.233702	0.044353	0.044537	0.425659
1.759	0.226139	0.038452	0.06402	0.431425
1.436	0.194625	0.02682	0.105591	0.468584
1.322	0.163336	0.020617	0.126145	0.493152
1.23	0.128389	0.016121	0.144104	0.515655
1.147	0.093085	0.014056	0.156536	0.530245
1.079	0.069912	0.014257	0.162705	0.538284
1.015	0.046182	0.014522	0.168355	0.541716
1.26	0.013458	0.013989	0.177336	0.546851
1.749	0.020507	0.016471	0.174416	0.533911
1.871	0.023333	0.025266	0.157836	0.530887
1.927	0.027236	0.034582	0.134338	0.556667
1.991	0.02997	0.044727	0.108384	0.60058
2.065	0.035846	0.05447	0.086063	0.63104

2.274	0.053859	0.060654	0.069647	0.626475
2.448	0.080389	0.064422	0.056297	0.591335
2.56	0.112039	0.067244	0.042623	0.545594

To normalize the scale factors into phase percentages, the absolute scale factors were summed and the scale factor for each respective phase (2H, 1T, triclinic) was divided by the sum.

Table A5: Large disordered (LD) MoS_2 Multi-Phase Scale Factor Refinement Results.

Voltage (V)	**2H**	**1T**	**triclinic**	**R_w**
2.122	0.15028	0.049944	0	0.540004
1.782	0.150015	0.049489	0.001901	0.533308
1.555	0.148173	0.048284	0.007179	0.522883
1.395	0.144854	0.047409	0.01169	0.509317
1.314	0.139588	0.045225	0.018116	0.498245
1.269	0.131374	0.043179	0.024416	0.48808
1.244	0.12059	0.04098	0.03211	0.477125
1.23	0.109151	0.037981	0.041612	0.467907
1.221	0.097664	0.03463	0.052336	0.461497
1.211	0.084581	0.031276	0.063276	0.461398
1.2	0.070372	0.027853	0.074472	0.468168
1.183	0.055492	0.023807	0.086582	0.484916
1.154	0.041162	0.019517	0.099064	0.509456
1.096	0.030165	0.015877	0.108798	0.532139

1.011	0.026287	0.013935	0.11332	0.543313
1.241	0.025947	0.014185	0.113899	0.543088
1.466	0.026092	0.016429	0.110461	0.542443
1.645	0.026099	0.019668	0.104608	0.54295
1.754	0.026892	0.023301	0.096671	0.542172
1.828	0.028809	0.027439	0.087355	0.545143
1.889	0.031267	0.031724	0.077374	0.551886
1.95	0.036329	0.035402	0.068076	0.55241
2.008	0.04323	0.038825	0.058418	0.544489
2.073	0.050734	0.042215	0.049235	0.532931
2.163	0.059609	0.045099	0.04045	0.513623
2.268	0.070797	0.046945	0.033697	0.497053
2.377	0.083013	0.047922	0.027066	0.481373
2.488	0.095688	0.049071	0.018792	0.475907

Table A6: Small crystalline (sc) MoS_2 Multi-Phase Scale Factor Refinement Results.

Voltage (V)	**2H**	**1T**	**triclinic**	**R_w**
2.241	0.40744	0.132475	0.032767	0.495611
1.879	0.400744	0.131129	0.052599	0.498741
1.487	0.376982	0.114156	0.116561	0.485906
1.373	0.348274	0.106921	0.144899	0.477977
1.311	0.313749	0.091766	0.187228	0.464572

1.271	0.269734	0.078023	0.233651	0.459227
1.241	0.222133	0.059629	0.286501	0.446801
1.21	0.168495	0.045634	0.333088	0.450678
1.161	0.122554	0.027578	0.382276	0.467067
1.069	0.096747	0.017148	0.408877	0.485771
1.102	0.087255	0.013471	0.416243	0.498571
1.442	0.090826	0.01485	0.41751	0.478542
1.716	0.08812	0.032287	0.387557	0.492367
1.833	0.084735	0.055306	0.343325	0.51308
1.903	0.085752	0.076911	0.293995	0.541286
1.982	0.094395	0.097439	0.245939	0.564395
2.065	0.111568	0.115685	0.202061	0.563519
2.219	0.14342	0.128574	0.168159	0.543416
2.382	0.186573	0.134557	0.141463	0.518599
2.673	0.295034	0.141724	0.068965	0.464099

Table A7: Small disordered (sd) MoS_2 Multi-Phase Scale Factor Refinement Results.

Voltage (V)	**2H**	**1T**	**triclinic**	**R_w**
2.314	0.102115	0.036639	0.007006	0.521383
1.804	0.103256	0.03644	0.010497	0.516864
1.549	0.10126	0.03488	0.016472	0.508899
1.36	0.096657	0.033404	0.021747	0.499568

1.264	0.088418	0.030535	0.030415	0.488969
1.213	0.07638	0.026542	0.041997	0.482632
1.177	0.061573	0.022055	0.055007	0.488915
1.137	0.045431	0.017717	0.067769	0.51586
1.077	0.030383	0.012921	0.081172	0.552634
1.227	0.022642	0.010121	0.089303	0.578169
1.581	0.021639	0.013239	0.08394	0.583123
1.778	0.021598	0.016946	0.076145	0.582129
1.897	0.022949	0.02203	0.065311	0.588592
2.004	0.028304	0.026715	0.053451	0.590933
2.115	0.037412	0.0307	0.042532	0.574103
2.275	0.048884	0.033737	0.03321	0.541457
2.457	0.062519	0.035495	0.024386	0.513151
2.656	0.079336	0.036715	0.015098	0.501471

For all samples, on the delithiation scan, the R_w briefly gets larger. This can also be seen in the asymmetry and hysteresis of the multi-phase refinements. We investigated several other possible phases to determine whether other structures were being formed during delithiation. These phases were not included in the final multi-phase fit because they did not make a significant contribution to PDF intensity or because their similarity to 2H, 1T, or triclinic caused too many parameters to be correlated during refinement. These phases are shown below.

Petkov $LiMoS_2$.

(Petkov, V.; Vogt, T.; Billinge, S.J.L.; Mahanti, S.D.; Larson, P.; Rangan, K.K.; Kanatzidis, M.G. "Structure of nanocrystalline materials using atomic pair distribution function analysis: study of $LiMoS_2$." Physical Review, Series 3. B – Condensed Matter, **2002**, 65, 921051 – 921054.)

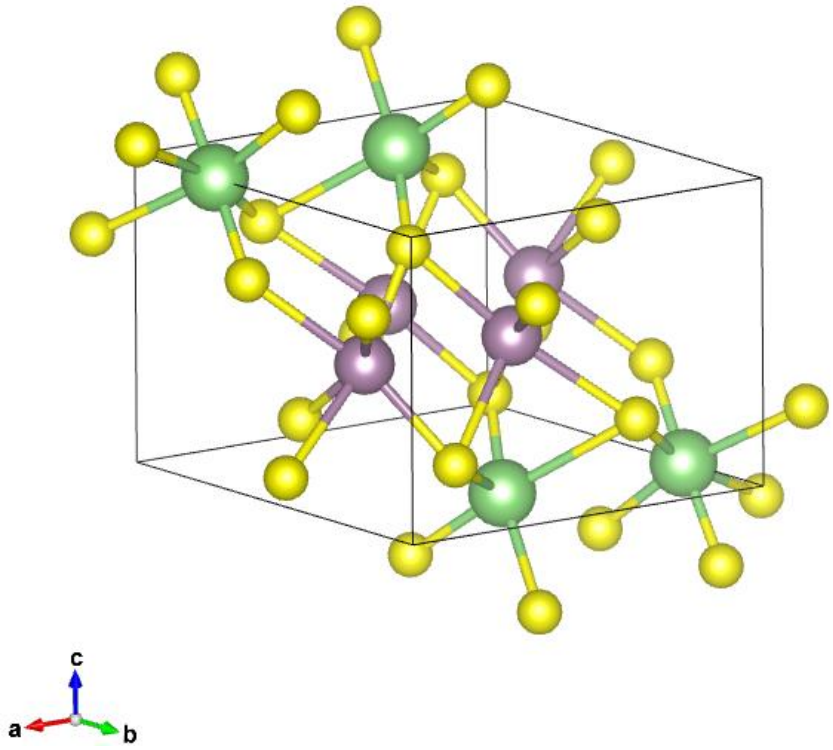

Figure A1. Unit cell of Petkov $LiMoS_2$, another lithiated MoS_2 phase with different Li ordering than triclinic Li_xMoS_2.

Table A8: Parameters to define crystal structure of refined Petkov $LiMoS_2$ phase.

a	b	c	α	β	γ	Scale factor	Delta1			
6.94635	6.38223	6.24468	88.6	89.07	120.06	0.058428	0.0			
elem	**x**	**y**	**z**	**u11**	**u22**	**u33**	**u12**	**u13**	**u23**	**occ**

Mo	0.506	0.7342	0.5138	0.001	0.001	0.001	0.001	0.001	0.001	1.0
Mo	0.494	0.2658	0.4862	0.001	0.001	0.001	0.001	0.001	0.001	1.0
Li	0.03	0.7481	0.013	0.001	0.001	0.001	0.001	0.001	0.001	1.0
Li	0.97	0.2519	0.987	0.001	0.001	0.001	0.001	0.001	0.001	1.0
Mo	0.9187	0.7251	0.4977	0.001	0.001	0.001	0.001	0.001	0.001	1.0
Mo	0.0813	0.2749	0.5023	0.001	0.001	0.001	0.001	0.001	0.001	1.0
S	0.1033	0.5369	0.7569	0.001	0.001	0.001	0.001	0.001	0.001	1.0
S	0.8967	0.4631	0.2431	0.001	0.001	0.001	0.001	0.001	0.001	1.0
S	0.6638	0.5628	0.7863	0.001	0.001	0.001	0.001	0.001	0.001	1.0
S	0.3362	0.4372	0.2137	0.001	0.001	0.001	0.001	0.001	0.001	1.0
S	0.1349	0.0158	0.771	0.001	0.001	0.001	0.001	0.001	0.001	1.0
S	0.8651	0.9842	0.229	0.001	0.001	0.001	0.001	0.001	0.001	1.0
S	0.6979	0.0736	0.7441	0.001	0.001	0.001	0.001	0.001	0.001	1.0
S	0.3021	0.9264	0.2559	0.001	0.001	0.001	0.001	0.001	0.001	1.0
Li	0.537	0.7356	0.009	0.001	0.001	0.001	0.001	0.001	0.001	1.0
Li	0.463	0.2644	0.991	0.001	0.001	0.001	0.001	0.001	0.001	1.0

3R-MoS_2.

3R-MoS_2 is a naturally occurring polymorph of MoS_2 that looks similar to 2H-MoS_2 but contains three S-Mo-S layers within one unit cell that are stacked in an A-B-C pattern.

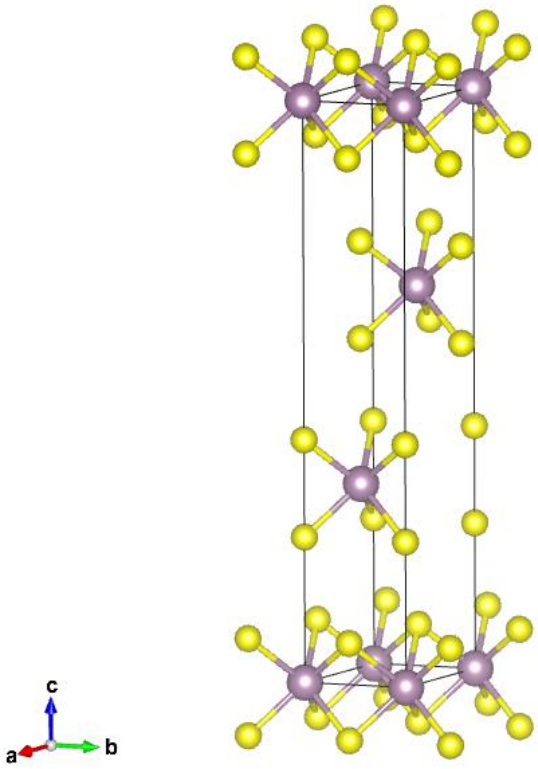

Figure A2. Unit cell of 3R-MoS_2.

Table A9: Parameters to define crystal structure of 3R-MoS_2 phase (not refined).

a	b	c	α	β	γ	Scale factor	Delta1			
3.16	3.16	18.33	90.0	90.0	120.0	1.0	0.0			
elem	**x**	**y**	**z**	**u11**	**u22**	**u33**	**u12**	**u13**	**u23**	**occ**
Mo	0.0	0.0	0.0	0.0	0.0	0.0	0.0	0.0	0.0	1.0
Mo	0.666667	0.333333	0.333333	0.0	0.0	0.0	0.0	0.0	0.0	1.0
Mo	0.333333	0.666667	0.666667	0.0	0.0	0.0	0.0	0.0	0.0	1.0
S	0.0	0.0	0.25	0.0	0.0	0.0	0.0	0.0	0.0	1.0

S	0.666667	0.333333	0.583333	0.0	0.0	0.0	0.0	0.0	0.0	1.0
S	0.333333	0.666667	0.916667	0.0	0.0	0.0	0.0	0.0	0.0	1.0
S	0.0	0.0	0.417	0.0	0.0	0.0	0.0	0.0	0.0	1.0
S	0.666667	0.333333	0.750333	0.0	0.0	0.0	0.0	0.0	0.0	1.0
S	0.333333	0.666667	0.0836667	0.0	0.0	0.0	0.0	0.0	0.0	1.0

APPENDIX B: Detailed Procedure for PDF Multi-Phase Refinement and Discussion of Other Phases Investigated for *Operando* XRD and PDF of SbSn

Parameters for crystal structures of SbSn, Sb, β-Sn, Li_3Sb, Li_2Sn_5, and Li_7Sn_3 (main phases included in multi-phase refinement) are given below.

Table B1: Parameters to define crystal structure of tetragonal SbSn.

a	**b**	**c**	**α**	**β**	**γ**	**Scale factor**	**Delta1**			
3.07497	3.07497	6.25924	90.0	90.0	90.0	1.0	0.0			
elem	**x**	**y**	**z**	**u11**	**u22**	**u33**	**u12**	**u13**	**u23**	**occ**
Sn	0.0	0.0	0.0	0.01	0.01	0.01	0.0	0.0	0.0	1.0
Sb	0.0	0.0	0.5	0.01	0.01	0.01	0.0	0.0	0.0	1.0

Table B2: Parameters to define crystal structure of hexagonal Sb.

a	**b**	**c**	**α**	**β**	**γ**	**Scale factor**	**Delta1**			
4.3084	4.3084	11.274	90.0	90.0	120.0	1.0	0.0			
elem	**x**	**y**	**z**	**u11**	**u22**	**u33**	**u12**	**u13**	**u23**	**occ**
Sb	0.0	0.0	0.23349	0.01	0.01	0.01	0.0	0.0	0.0	1.0
Sb	0.666667	0.333333	0.566823	0.01	0.01	0.01	0.0	0.0	0.0	1.0
Sb	0.333333	0.666667	0.900157	0.01	0.01	0.01	0.0	0.0	0.0	1.0

Table B3: Parameters to define crystal structure of tetragonal β-Sn.

a	b	c	α	β	γ	Scale factor	Delta1			
5.90801	5.90801	3.24562	90.0	90.0	90.0	1.0	0.0			
elem	**x**	**y**	**z**	**u11**	**u22**	**u33**	**u12**	**u13**	**u23**	**occ**
Sn	0.0	0.0	0.0	0.01	0.01	0.01	0.0	0.0	0.0	1.0
Sn	0.5	0.0	0.25	0.01	0.01	0.01	0.0	0.0	0.0	1.0
Sn	0.5	0.5	0.5	0.01	0.01	0.01	0.0	0.0	0.0	1.0
Sn	0.0	0.5	0.75	0.01	0.01	0.01	0.0	0.0	0.0	1.0

Table B4: Parameters to define crystal structure of cubic Li_3Sb.

a	b	c	α	β	γ	Scale factor	Delta1			
6.61003	6.61003	6.61003	90.0	90.0	90.0	0.024004	0.0			
elem	**x**	**y**	**z**	**u11**	**u22**	**u33**	**u12**	**u13**	**u23**	**occ**
Li	0.5	0.0	0.0	0.01	0.01	0.01	0.0	0.0	0.0	1.0
Li	0.25	0.25	0.75	0.01	0.01	0.01	0.0	0.0	0.0	1.0
Li	0.25	0.75	0.75	0.01	0.01	0.01	0.0	0.0	0.0	1.0
Li	0.5	0.5	0.5	0.01	0.01	0.01	0.0	0.0	0.0	1.0
Li	0.25	0.75	0.25	0.01	0.01	0.01	0.0	0.0	0.0	1.0
Li	0.25	0.25	0.25	0.01	0.01	0.01	0.0	0.0	0.0	1.0
Li	0.0	0.0	0.5	0.01	0.01	0.01	0.0	0.0	0.0	1.0

Li	0.75	0.25	0.25	0.01	0.01	0.01	0.0	0.0	0.0	1.0
Li	0.75	0.75	0.25	0.01	0.01	0.01	0.0	0.0	0.0	1.0
Li	0.0	0.5	0.0	0.01	0.01	0.01	0.0	0.0	0.0	1.0
Li	0.75	0.75	0.75	0.01	0.01	0.01	0.0	0.0	0.0	1.0
Li	0.75	0.25	0.75	0.01	0.01	0.01	0.0	0.0	0.0	1.0
Sb	0.0	0.0	0.0	0.0377436	0.0412945	0.0391791	0.0	0.0	0.0	3.9981
Sb	0.0	0.5	0.5	0.0667291	0.0651218	0.0432717	0.0	0.0	0.0	2.8798
Sb	0.5	0.0	0.5	0.0476113	0.03598	0.0354826	0.0	0.0	0.0	3.7716
Sb	0.5	0.5	0.0	0.0146728	0.0119128	0.0133909	0.0	0.0	0.0	4.3187

Table B5: Parameters to define crystal structure of Li_7Sn_3.

a	**b**	**c**	**α**	**β**	**γ**	**Scale factor**	**Delta1**			
8.53178	4.7432	9.46157	90.0	106.104	90.0	1.0	0.0			
elem	**x**	**y**	**z**	**u11**	**u22**	**u33**	**u12**	**u13**	**u23**	**occ**
Li	0.603698	0.25	0.275102	0.01	0.01	0.01	0.0	0.0	0.0	1.0
Li	0.396302	0.75	0.724898	0.01	0.01	0.01	0.0	0.0	0.0	1.0
Li	0.993033	0.25	0.872697	0.01	0.01	0.01	0.0	0.0	0.0	1.0
Li	0.006967	0.75	0.127303	0.01	0.01	0.01	0.0	0.0	0.0	1.0
Li	0.005569	0.25	0.37925	0.01	0.01	0.01	0.0	0.0	0.0	1.0
Li	0.994431	0.75	0.62075	0.01	0.01	0.01	0.0	0.0	0.0	1.0
Li	0.199625	0.25	0.681727	0.01	0.01	0.01	0.0	0.0	0.0	1.0

Li	0.800375	0.75	0.318273	0.01	0.01	0.01	0.0	0.0	0.0	1.0
Li	0.187827	0.25	0.169822	0.01	0.01	0.01	0.0	0.0	0.0	1.0
Li	0.812173	0.75	0.830178	0.01	0.01	0.01	0.0	0.0	0.0	1.0
Li	0.400178	0.25	0.46625	0.01	0.01	0.01	0.0	0.0	0.0	1.0
Li	0.599822	0.75	0.53375	0.01	0.01	0.01	0.0	0.0	0.0	1.0
Li	0.398285	0.25	0.985556	0.01	0.01	0.01	0.0	0.0	0.0	1.0
Li	0.601715	0.75	0.014444	0.01	0.01	0.01	0.0	0.0	0.0	1.0
Sn	0.595798	0.25	0.776008	0.01	0.01	0.01	0.0	0.0	0.0	1.0
Sn	0.404202	0.75	0.223992	0.01	0.01	0.01	0.0	0.0	0.0	1.0
Sn	0.806016	0.25	0.085608	0.01	0.01	0.01	0.0	0.0	0.0	1.0
Sn	0.193984	0.75	0.914392	0.01	0.01	0.01	0.0	0.0	0.0	1.0
Sn	0.802869	0.25	0.567666	0.01	0.01	0.01	0.0	0.0	0.0	1.0
Sn	0.197131	0.75	0.432334	0.01	0.01	0.01	0.0	0.0	0.0	1.0

Table B6: Parameters to define crystal structure of Li_2Sn_5.

a	**b**	**c**	**α**	**β**	**γ**	**Scale factor**	**Delta1**			
10.3461	10.3461	3.15855	90.0	90.0	90.0	0.015319	0.0			
elem	**x**	**y**	**z**	**u11**	**u22**	**u33**	**u12**	**u13**	**u23**	**occ**
Li	0.825075	0.325075	0.5	0.01	0.01	0.01	0.0	0.0	0.0	1.0
Li	0.674925	0.825075	0.5	0.01	0.01	0.01	0.0	0.0	0.0	1.0
Li	0.325075	0.174925	0.5	0.01	0.01	0.01	0.0	0.0	0.0	1.0

Li	0.174925	0.674925	0.5	0.01	0.01	0.01	0.0	0.0	0.0	1.0
Sn	0.795179	0.068179	0.0	0.01	0.01	0.01	0.0	0.0	0.0	1.0
Sn	0.204821	0.931821	0.0	0.01	0.01	0.01	0.0	0.0	0.0	1.0
Sn	0.931821	0.795179	0.0	0.01	0.01	0.01	0.0	0.0	0.0	1.0
Sn	0.068179	0.204821	0.0	0.01	0.01	0.01	0.0	0.0	0.0	1.0
Sn	0.0	0.5	0.0	0.01	0.01	0.01	0.0	0.0	0.0	1.0
Sn	0.5	0.0	0.0	0.01	0.01	0.01	0.0	0.0	0.0	1.0
Sn	0.704821	0.568179	0.0	0.01	0.01	0.01	0.0	0.0	0.0	1.0
Sn	0.431821	0.704821	0.0	0.01	0.01	0.01	0.0	0.0	0.0	1.0
Sn	0.568179	0.295179	0.0	0.01	0.01	0.01	0.0	0.0	0.0	1.0
Sn	0.295179	0.431821	0.0	0.01	0.01	0.01	0.0	0.0	0.0	1.0

During multi-phase refinement, only the scale factor of each phase was relaxed. Multi-phase refinement results, including goodness of fit (R_w), are shown for each sample in tables below.

Table B7: 1st Lithiation of nanoporous SbSn PDF multi-phase refinement.

Voltage (V)	**SbSn**	**Li_3Sb**	**Sn**	**Li_2Sn_5**	**Li_7Sn_3**	**R_w**
2.653	0.137332	0	0.023078	0.008029	0	0.563281
1.11	0.155574	0	0.022184	0.009532	0.000352	0.52693
0.843	0.161002	0	0.02087	0.009553	0.000537	0.507094
0.803	0.156725	0	0.019348	0.009198	0.000811	0.497003
0.794	0.155064	0	0.018984	0.009307	0.00099	0.489535
0.789	0.146321	0	0.019503	0.0095	0.000933	0.489685

0.784	0.132458	0.003263	0.020784	0.009188	0.000774	0.492887
0.777	0.115992	0.007534	0.022344	0.008807	0.000531	0.502505
0.767	0.09687	0.012333	0.02404	0.008389	0.000431	0.513908
0.753	0.074329	0.017712	0.025748	0.007741	0.000454	0.517566
0.728	0.047703	0.023996	0.027934	0.006804	0.000574	0.499848
0.673	0.015194	0.032079	0.030086	0.006578	0.000954	0.448785
0.598	0	0.037915	0.026291	0.008352	0.002162	0.405112
0.529	0.003761	0.037578	0.006528	0.021549	0.006685	0.378607
0.368	0	0.04017	0	0.017577	0.010904	0.351271
0.316	0	0.040824	0	0.013093	0.014531	0.344902
0.267	0	0.040972	0	0.008078	0.019712	0.342485
0.211	0	0.041067	0	0.004196	0.023798	0.341499
0.16	0	0.041248	0	0.002649	0.025052	0.343634
0.117	0	0.041333	0	0.001622	0.025365	0.342137
0.081	0	0.041242	0	0.001346	0.025236	0.34395
0.051	0	0.041116	0	0.000851	0.025054	0.345226

To normalize the scale factors into phase percentages, the absolute scale factors were summed and the scale factor for each respective phase (SbSn, Sb, β-Sn, Li_3Sb, Li_2Sn_5, Li_7Sn_3) was divided by the sum.

Table B8: 1st Delithiation of nanoporous SbSn PDF multi-phase refinement.

Voltage (V)	**SbSn**	**Li_3Sb**	**Sn**	**Li_7Sn_3**	**Sb**	**R_w**

0.478	0.01527	0.045645	0	0.039003	0	0.305315
0.602	0.016191	0.04613	0	0.039387	0	0.305229
0.651	0.018113	0.046068	0	0.03352	0	0.312611
0.748	0.02182	0.046066	0	0.021954	0	0.341249
0.836	0.023724	0.045607	0.007668	0.022514	0	0.362013
0.951	0.019833	0.045104	0.021606	0.0186	0	0.393338
1.012	0.019989	0.043397	0.022197	0.018474	0	0.414331
1.045	0.026421	0.040006	0.020186	0.019059	0	0.448289
1.068	0.039562	0.035	0.014694	0.019518	0	0.497984
1.091	0.051036	0.025045	0.016302	0.01818	0.00534	0.603725
1.115	0.054727	0.019201	0.020298	0.016509	0.013744	0.660801
1.277	0.06001	0.010212	0.027446	0.013289	0.027732	0.717111

Phase fitting on the *operando* PDF data for nanoporous SbSn was also performed on several other possible lithiated antimony and lithiated tin phases to confirm their absence. These are shown below.

Li_2Sb:

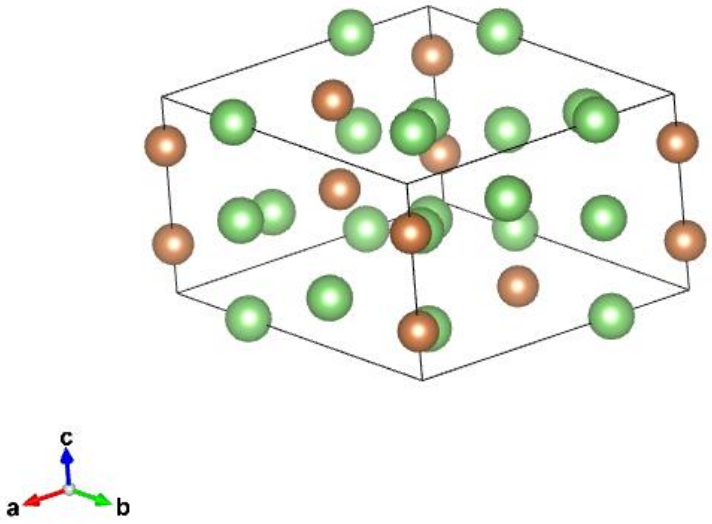

Figure B1. Unit cell of hexagonal Li_2Sb.

Table B9: Parameters to define crystal structure of Li_2Sb.

a	b	c	α	β	γ	Scale factor	Delta1			
7.9514	7.9514	6.56835	90.0	90.0	120.0	1.0	0.0			
elem	**x**	**y**	**z**	**u11**	**u22**	**u33**	**u12**	**u13**	**u23**	**occ**
Li	0.291006	0.0	0.0	0.01	0.01	0.01	0.0	0.0	0.0	1.0
Li	0.708994	0.708994	0.5	0.01	0.01	0.01	0.0	0.0	0.0	1.0
Li	0.0	0.291006	0.5	0.01	0.01	0.01	0.0	0.0	0.0	1.0
Li	0.0	0.291006	0.0	0.01	0.01	0.01	0.0	0.0	0.0	1.0
Li	0.708994	0.708994	0.0	0.01	0.01	0.01	0.0	0.0	0.0	1.0
Li	0.291006	0.0	0.5	0.01	0.01	0.01	0.0	0.0	0.0	1.0
Li	0.637321	0.009891	0.25	0.01	0.01	0.01	0.0	0.0	0.0	1.0
Li	0.37257	0.362679	0.25	0.01	0.01	0.01	0.0	0.0	0.0	1.0

Li	0.990109	0.62743	0.25	0.01	0.01	0.01	0.0	0.0	0.0	1.0
Li	0.62743	0.990109	0.75	0.01	0.01	0.01	0.0	0.0	0.0	1.0
Li	0.362679	0.37257	0.75	0.01	0.01	0.01	0.0	0.0	0.0	1.0
Li	0.009891	0.637321	0.75	0.01	0.01	0.01	0.0	0.0	0.0	1.0
Sb	0.0	0.0	0.25	0.01	0.01	0.01	0.0	0.0	0.0	1.0
Sb	0.0	0.0	0.75	0.01	0.01	0.01	0.0	0.0	0.0	1.0
Sb	0.333333	0.666667	0.023772	0.01	0.01	0.01	0.0	0.0	0.0	1.0
Sb	0.333333	0.666667	0.476228	0.01	0.01	0.01	0.0	0.0	0.0	1.0
Sb	0.666667	0.333333	0.976228	0.01	0.01	0.01	0.0	0.0	0.0	1.0
Sb	0.666667	0.333333	0.523772	0.01	0.01	0.01	0.0	0.0	0.0	1.0

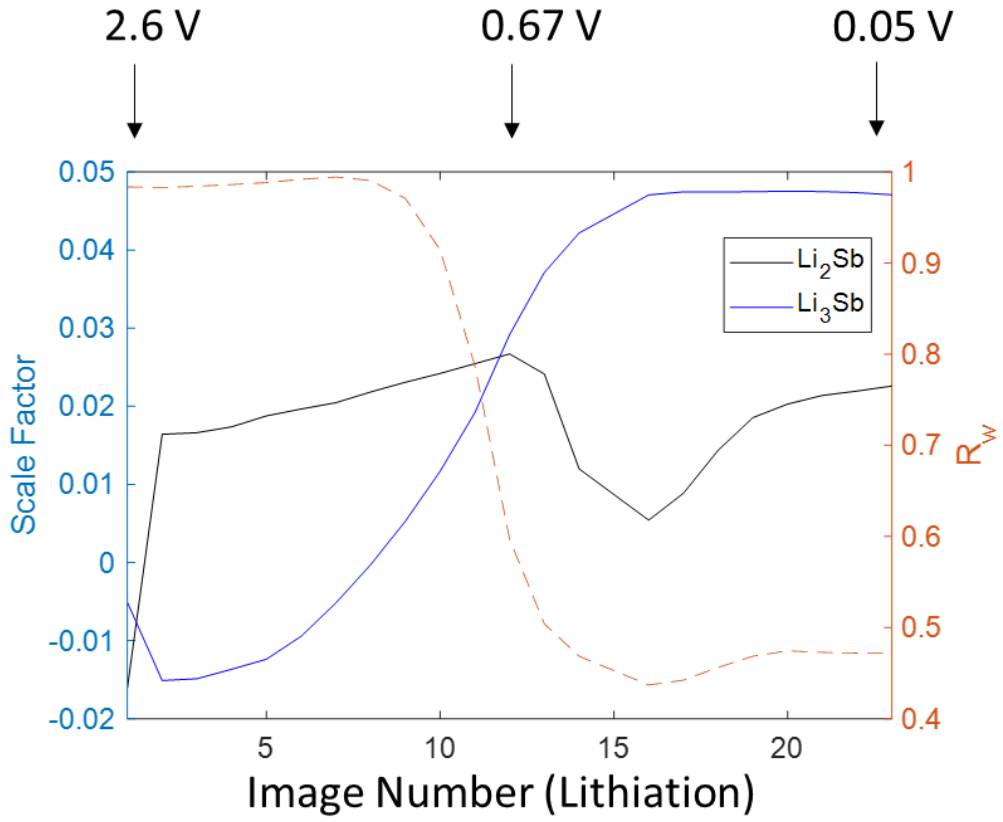

Figure B2. Multi-phase refinement of np-SbSn lithiation scan with Li_2Sb and Li_3Sb.

Although it may look like there is some increase in the scale factor of Li_2Sb, we consider the magnitude on the same order as the noise level and not significant. The R_w, goodness of fit parameter, does not improve until a significant fraction of Li_3Sb is factored in.

LiSn:

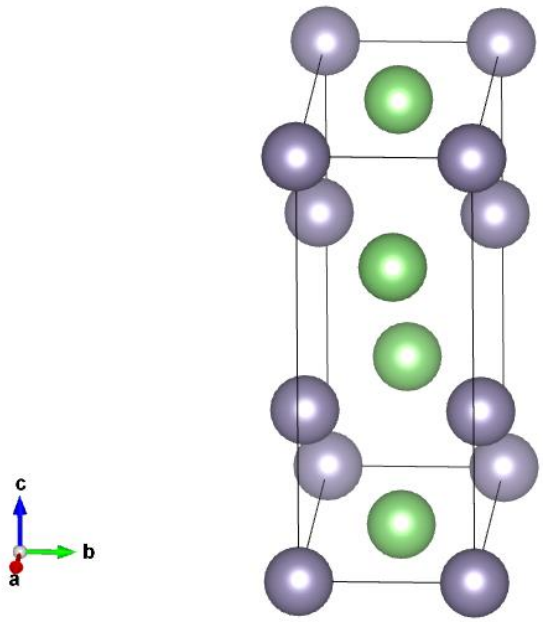

Figure B3. Unit cell of monoclinic LiSn.

Table B10: Parameters to define crystal structure of LiSn.

a	b	c	α	β	γ	Scale factor	Delta1	

5.1814	3.22409	7.80534	90.0	105.747	90.0	1.0	0.0			
elem	**x**	**y**	**z**	**u11**	**u22**	**u33**	**u12**	**u13**	**u23**	**occ**
Li	0.268026	0.5	0.331701	0.01	0.01	0.01	0.0	0.0	0.0	1.0
Li	0.5	0.5	0.0	0.01	0.01	0.01	0.0	0.0	0.0	1.0
Li	0.731974	0.5	0.668299	0.01	0.01	0.01	0.0	0.0	0.0	1.0
Sn	0.241273	0.0	0.661946	0.01	0.01	0.01	0.0	0.0	0.0	1.0
Sn	0.758727	0.0	0.338054	0.01	0.01	0.01	0.0	0.0	0.0	1.0
Sn	0.0	0.0	0.0	0.01	0.01	0.01	0.0	0.0	0.0	1.0

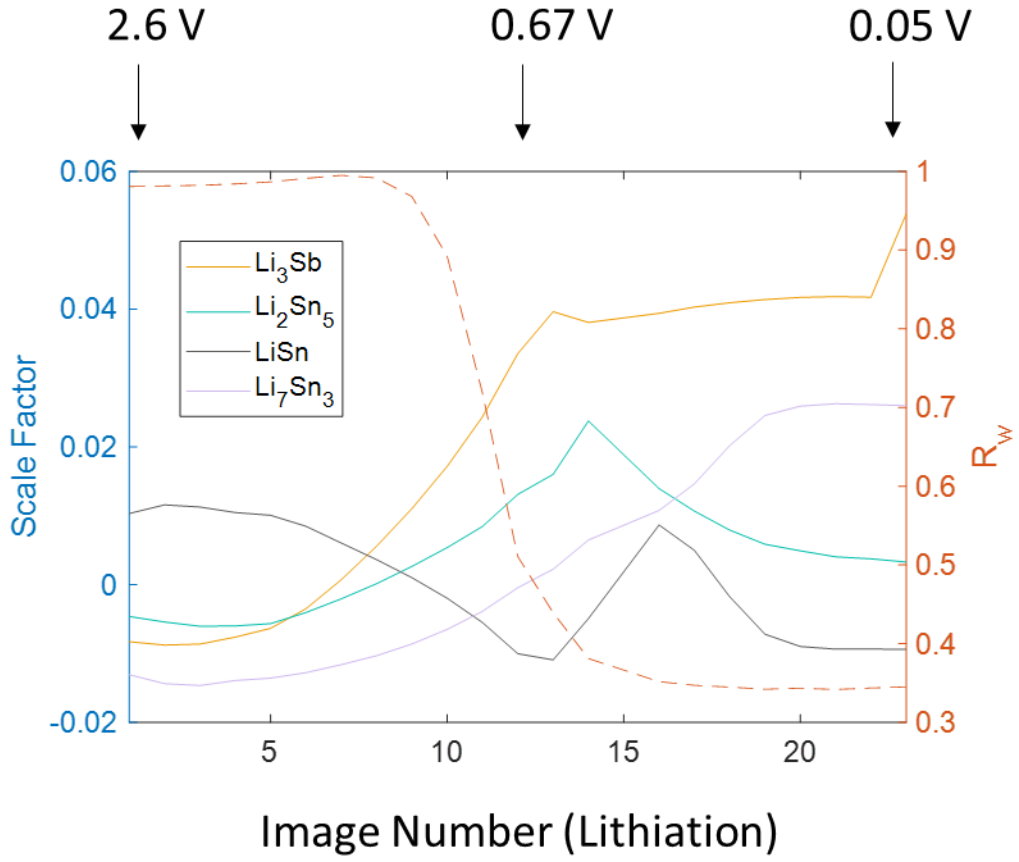

Figure B4. Multi-phase refinement of np-SbSn lithiation scan including LiSn, Li_3Sb, Li_2Sn_5, Li_7Sn_3.

The scale factor of LiSn begins at a non-zero value during lithiation scan, although we know that there cannot be any existing LiSn before Li^+ insertion has started. Therefore, we consider this magnitude of scale factor value as background-noise level, and because the scale factor of LiSn never exceeds this background level throughout lithiation, we conclude that no significant amount of LiSn is formed during lithiation.